UNIVERSITÁ DEGLI STUDI DI PADOVA

DIPARTIMENTO DI FISICA "'GALILEO GALILEI"'

Scuola di dottorato di ricerca in Fisica

XXI Ciclo

Wetting on Anisotropically Patterned and Rough Surfaces

Direttore della scuola: Ch.mo Prof. ATTILIO STELLA .....

Supervisore: Ch.mo Prof. GIAMPAOLO MISTURA .....

Co-Supervisore: Ch.mo Prof. ENZO ORLANDINI .....

Dottorando: Ciro Semprebon

January 2009

to my parents

Occupat obsessos sudor mihi frigidus artus,
Caeruleaeque cadunt toto de corpore guttae;
quaque pedem movi, manat locus, eque capillis
ros cadi, et citius, quam nunc tibi facta renarro,
in latices mutor. Sed enim cognoscit amatas
amnis aquas, positoque viri, quod sumpserat, ore,
vertitur in proprias, ut se mihi miscerat, undas.
OVIDIO: METAMORPHOSEON LIBRI

Abstract

(Italiano)

Da quando Young nel 1805 [1] descrisse a parole le relazioni trigonometriche tra l'angolo di contatto e le forze agenti su una goccia in equilibrio meccanico su una superficie solida sono stati ottenuti molti progressi nella descrizione di vari aspetti del wetting. Inoltre i progressi degli ultimi anni nel campo della microlavorazione hanno permesso di ottenere in modo semplice superfici con pattern chimici e geometrici assai regolari, su cui è stato possibile testare sperimentalmente le ipotesi dei vari modelli teorici. Oltre a tutti i pattern caratterizzati da una disposizione globalmente isotropa delle asperità, sono stati prodotti pattern costituiti da una serie di strisce e rilievi paralleli gli uni agli altri, introducendo così un elemento anisotropo nel substrato. Negli ultimi anni molti lavori sono stati rivolti alla caratterizzazione del comportamento anisotropo delle gocce su tali substrati. Tuttavia ad oggi non esiste una teoria completa che descriva l'anisotropia di gocce in queste condizioni. Inoltre la maggior parte dei lavori precedenti riguarda lo studio dell'anisotropia su pattern regolari costituiti da canali micrometrici.

Per fornire una descrizione generale di quegli aspetti del comportamento anisotropo che sono indipendenti dai dettagli del pattern regolare su scala micrometrica, e per evidenziare l'influenza di diverse bagnabilità della superficie, in questa tesi abbiamo studiato il wetting anisotropo di gocce depositate su singoli rilievi, caratterizzati da una supervicie piana e spigoli vivi, e costruiti con diversi materiali. L'anisotropia è stata quantificata misurando gli angoli di contatto e le dimensioni della base delle gocce nei due principali assi di simetria. Le misure sono state ottenute con u apparato fatto in casa, e il software di analisi è stato interamente sviluppato durante questa tesi. Il risultato principale consiste nel fatto che la differenza tra gli angoli di contatto nelle due direzioni $\Delta\theta$ e l'eccentricità di base ϵ mostrano la stessa relazione all'interno degli errori sperimentali, indipendentemente dalla bagnabilità del substrato. Queste misure sono state completate tramite simulazioni numeriche per mezzo del metodo Lattice Boltzmann, e che hanno mostrato un buon accordo con i risultati sperimentali. Inoltre abbiamo formulato un semplice modello geometrico, valido per piccoli ϵ, che riproduce qualitativamente sia i risultati sperimentali che quelli numerici.

Inoltre in questa tesi ho caratterizzato la bagnabilità di sottili film (isotropici) di titania nanostrutturata, mettendola in relazione con le proprietà morfologiche dei substrati stessi.

Abstract

(English)

Since Young in 1805 [1] described in words the trigonometric relations between the contact angle and the forces acting on a droplet in mechanical equilibrium on a sulid surface, many advances in the description of several aspects of wetting behavior have been done. Besides the recent years developements in the field of micropatterning allowed the production surfaces with chemical and geometrical regular patterns, which make possible a direct test of theoretical models. Beyond the patterns characterized by a global isotropic disposition if the surface asperities and heterogeneities, patterns constituted of series of parallel stripes or reliefs have been produced, introducing an anisotropic element in the substrate. Recently many works focused on the characterization of the anisotropic behavior of droplets on those surfaces. However there is not a complete theory describing the anisotropy of droplets in these conditions. Furthermore most part of previous works study the anisotropy on regular patterns made by micrometric channels.

To give a general description of those aspects of the anisotropic behavior which are independent by the nature of the micrometric regular pattern, and to focus on the influence of different wettabilities, in this thesis we studied the anisotropic wetting of droplets sitting on the top of single posts, characterized by flat surfaces and sharp corners, and made with different materials. The anisotropy was quantified by measuring the contact angles and base elongations in the two principal symmetry axis. Measurements were obtained by a homemade apparatus, and the analysis software has been entirely developed in this thesis. The main finding is that the contact angle difference $\Delta\theta$ and the base eccentricity ϵ show the same relation within the experimental errors regardless of surface wettability. These measurements were complemented by numerical simulations with the Lattice Boltzmann method, which showed a good agreement with experimental results. We also developed a simple geometrical model, valid for small ϵ, which reproduces qualitatively experimental and numerical data.

In addition, during this thesis I characterized the wetting properties of thin (isotropic) films of nanostructured titania, and related them to the morphological parameters of the substrates.

Contents

Chapter 1

Introduction

Surface wettability is an important property of materials, which is generally characterized by measuring the contact angle of a liquid droplet sitting on the surface. When water is used, a contact angle less than 90° is indicative of a hydrophilic surface while a contact angle greater than 90° is indicative of a hydrophobic surface. If a surface shows identical contact angles when measured from different directions, the surface is said to be isotropic in wettability, otherwise it is anisotropic. Modification of surface wettability is achieved through either chemical or physical means or through both. Chemical means such as silanization [2] fluorination [3] plasma treatment [4] and photolytic treatment [5] have been widely used; some of these, however, suffer the drawback of a short-lived effect. Physical means of modifying surface wettability are typically achieved through surface roughening, which results in either ordered or disordered surface structures. Very often, surface roughening or patterning works together with chemical treatments to alter surface wettability [6]. Meanwhile, the natural world has provided some inspirations for surface wettability modifications. For example, the hierarchical surface texture is responsible for the superhydrophobic and selfcleaning properties of the lotus leaf [23], the hierarchical structure in a gecko's foot gives rise to its ability to adhere to the wall and ceiling [7]; and the heterogeneous surface on a Stenocara beetle's back consisting of hydrophilic spots on a hydrophobic background endows the beetle with a unique water harvesting capability in the desert [8]. These inspirations have led to a lot of efforts to mimic these biological structures, in particular the hierarchical structure of the lotus leaf and thus the remarkable superhydrophobic property. Most of these examples reported isotropic hierarchical structures with the aim to achieve superhydrophobicity on different materials such as on silicon and polymer substrates.

Anisotropic wettability has attracted much interest more recently. Similar to the approaches taken on tuning the surface wettability, anisotropic wettability is also achieved either through chemical patterning [9; 10; 11] or surface roughening [12; 13]. Surfaces with controlled anisotropic wettability have the advantage of restricting liquid flow to a desired direction, which

has potential applications in microfluidic devices [14]. For example, Sommers et al. reported drainage enhancement with the aid of wetting anisotropy on an aluminum surface [15]. In nature, anisotropic wettability has been observed on the surface of the rice leaf, and it has been mimicked by growing aligned carbon nanotubes on a substrate [16].

In this thesis two different topic related to wetting phenomena are studied. In the first we reproduce the essential character of anisotropic rough substrates by taking an homogeneuos surface confined by two potential walls assumed to be infinite. Most of the works cited focus on the dynamic of the drop spreading, while our system focus on the details of the final state of minimum energy, which does not depend from the deposition proces, becouse all intermediate potential barriers are suppressed. The second topic regards the specific study of a titania substrate obtained with a Supersonic Cluster Beam deposition technique, very meaningfull in biochemical applications, which show a controlled and homogeneous roughness. Chapters 3, 5, 6 are directely referred to the first topic while the second one is exposed in chapter 7.

More in detail, in **chapter 2** we briefly introduce the most common laws on wetting, like the Young Equation, the problem of istheresys and the Wenzen and Cassie-Baxter models.

In **chapter 3** we give a general description of the standard experimental thechniques inherent to the fabrication of samples involved in the experimental study of the first topic. They regards cleaning methods by UV treatments, silanization techniques in order to obtain anti stick surfaces and tune its surface energy, the UV litography, etching techniques, litogrphy with thiolenic resins, and replica molding. Another thechniques is the Micro electrical discharge machining, but being developed out of laboratory is briefly mentioned in the chapter of results.

In **chapter 4** are reported all experimental techniques and procedures involved in the measurement of contact angles: after a description of the experimental setup, are summarized manual operations of repeated measurements in standard conditions, anisotropy measurements and advancing contact angles measurements. We also give an extimation of the contact angle variation due to the loss of liquid by evaporation if, as in the case of anisotropy measurements, every droplet has to be photographed three times.

In **chapter 5** is described the Lattice Boltzmann algorythm used for the numerical simulations. For this study the dynamic is used only to reach a configuration of minimum energy, and all resuts represent states or metastates of equilibrum.

In **chapter 6** we report a full characterization of anisotropy involving all thechniques previously described. First we give an introduction which draw the state of the art on this topic, until very recent experimental and theoretical works. The following work is subdivided in three principal sections: in the first all samples produced are full characterized, acquired data are exposed, focusing on the profile analysis, which denote clear deviations od curvature. Finally is given a first global picture of the topic, which suggest what significant parameters describe better anisotropy

with generality. In the second section we full decribe most significant simulation results, focusing on methods to extract physical parameters from the density maps of the simulation. In this section we indagate the path the drop follows during the minimization, a characterization of the triple phase contact line and of the two main axial profiles at varyin of surface parameters, and give a comparison between numerical and experimental results. I the third section we propose a simple geometrical medel, which give some useful informations in the case of low anisotropy, and that i some cases well fit experimental data. Finally we give a general discussion, which resumes and compares all previous results, emphatizing similarities and differences, and gives a physical interpretation.

In chapter **7** we report a full characterization of wetting on Supersonic Beam Cluster Assembles titania surfaces. First is introduced with generality the titalium element, focusing on its biochemical properties. Then is reported a sinthetic description of the deposition SCBD apparatus for the sample production, followed by a full morphological characterization, and finally by the correlation between morphological parameters, thermal treatments and wetting behavior.

In the **appendice A** are reported details of calculations. It includes a description of the fitting procedure, and of part of the software developed.

Chapter 2

Wetting phenomena

In this chapter we introduce the basic concept of wettability, and the most common models which describe the behavior of liquids on solid surfaces. This is one of the most important properties of solid surfaces, governed by both the surface chemical composition and its morphology [17; 18].

2.1 Young Equation

When a liquid is brought into contact with a flat homogeneous solid surface, the degree of the spreading depends on only the surface chemistry. Young [1] and Laplace [19] in 1805 first associated the equilibrium drop shape to the competition between the interfacial energies of the solid, liquid, and gas. Young and Laplace realized that when there is an interface between two materials, there is a specific energy, termed the interfacial energy, which is proportional to the number of molecules present at that interface. In other words, this energy is proportional to the surface area of the interface and the constant of proportionality is called the surface tension. Since in wetting phenomena we typically have a liquid, a solid and a surrounding gas, there are three types of surface tensions: the liquid-gas σ_{lg} , the gas-solid σ_{gs} and the liquid-solid σ_{ls} surface tensions.

When liquid drops are in air, they are spherical in order to minimize the surface energy. When they are in contact with a solid, the liquid-gas interface maintains a spherical cap profile and the angle at which the liquid drop joins the solid is called the contact angle θ, where

$$\cos\theta = \frac{\sigma_{gs} - \sigma_{ls}}{\sigma_{lg}} \tag{2.1}$$

This equilibrium contact angle is often called the Youngś angle. In the literature, a solid surface

is called hydrophilic when a water droplet appears with $\theta < 90°$, and hydrophobic when $\theta > 90°$. This is illustrated in the schematic diagram shown in Fig. 2.1

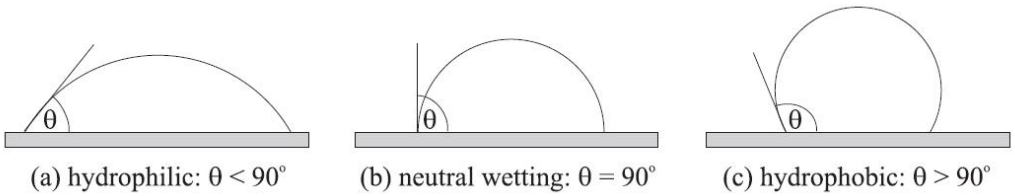

Figure 2.1: Schematic diagrams of a liquid drop on (a) a hydrophilic, (b) a neutrally wetting and (c) a hydrophobic surface.

Another important concept associated with the surface tension is the Laplace pressure. When crossing a curved interface, the pressure of the system on the two sides of the interface differs by

$$\Delta P = \sigma_{lg} k \tag{2.2}$$

where k is the total curvature of the interface. In static or quasi-static situations, the Laplace pressure, and hence the curvature of the drop is constant. With two dimensions the only possible solution is the cylindrical droplet, where the interface is given by an exact circular shape and $k = 1/R$. In three dimensions, if we define two directions mutually orthogonal on the liquid surface we have

$$k = \frac{1}{R_1} + \frac{1}{R_2} \tag{2.3}$$

where R_1 and R_2 are the lcal curvature radii, in the two orthogonal directions. If the droplet is isotropic the curvature is the same in all directions, but when the droplet is forced to have high distorted base shapes this assumption is no longer true and different directions are characterized by different local curvatures ($R_1 \neq R_2$) So far we have only considered surface tension effects and the majority of works we present here deals with systems where surface tension is the dominant force in the problem. It is therefore important to know when this approximation holds, in particular the typical length scale below which we can neglect gravity. The energy associated with surface tension scales as $\sigma_{lg} R^2$ where R is the size of the drop. On the other hand, the gravitational energy of a drop scales as $\Delta n g R^4$ where Δn is the density difference between the liquid and gas phase and g is the gravitational acceleration. Therefore we can safely neglect gravity if $\sigma_{lg} R^2 \ll \Delta n g R^4$, or alternatively when the size of the drop is much smaller than the so-called capillary length, λ_C, where

$$\lambda_C = \sqrt{\frac{\sigma_{lg}}{\Delta n g}} \tag{2.4}$$

Putting the typical values of water, e.g. $\sigma_{lg} = 10^{-2} N \times m^{-1}$, $\Delta n = 103 kg \times m^{-3}$ and $g = 10 m \times s^{-2}$, we find $\lambda_C \sim 1mm$. Typical droplet size of our experiments goes from $0.1\mu l$ to $1\mu l$ which, assuming an hemispherical cup shape, correspod to a radius from $0.36mm$ to $0.78mm$: just below λ_C. Lower volumes are not accessible to our apparatus, due to evaporation effects. At a first approximation, gravity effects can be neglected. gravity effects may be even then neglected.

2.2 Surface heterogeneities

Real solids are chemically heterogeneous and rough, and are thus far from being the ideally smooth and homogeneous surface we have assumed when deriving Eq. 2.1. These heterogeneities are often at micron-scale, although some recent works [22; 21; 20] suggest that nanometric scale heterogeneities may play an important role too, especially on superhydrophobic surfaces.

The effect of surface heterogeneities are summarized in two quantities: the effective (or apparent) contact angle and the contact angle hysteresis. The effective contact angle measures the average properties of the surface, while the contact angle hysteresis quantifies the variability of the contact angle measurements. The largest static angle is called the advancing contact angle, θ_A, while the smallest angle is called the receding contact angle, θ_R. Several methods have been developed to measure advancing and receding contact angles. That developed in our laboratory is described in section 4. The contact angle hysteresis is defined as $\Delta\theta = \theta_A - \theta_R$. Usually both these quantities should be given.

2.3 Superhydrophobic surfaces

Superhydrophobic surfaces are the best example of how surface heterogeneities can alter the wettability of a surface. When a liquid drop spreads on a smooth hydrophobic surface, the highest contact angle one can achieve is of order $120 - 130^\circ$ [18]. When the hydrophobic surface is made rougher, however, higher contact angles are possible. Several natural materials exhibit this so-called superhydrophobicity, with contact angles between $150 - 165^\circ$. The most famous example is the leaf of lotus plant [23; 24]. Here, there are two scales of roughness of $10\mu m$ and $1\mu m$, and these bumps promote superhydrophobicity by trapping the gas phase in between the corrugations.

Recently, many research groups have been able to reproduce superhydrophobic surfaces. The earliest superhydrophobic surfaces were made by patterning hydrophobic surfaces by regular posts of the same material [25]. Similar regular structures were produced in our laboratory by Pozzato

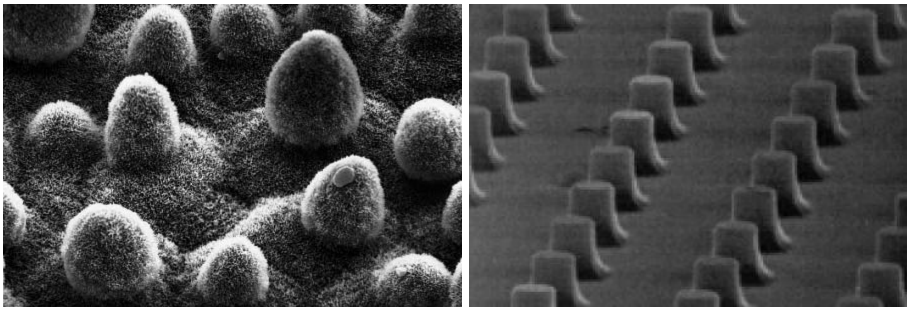

Figure 2.2: Scanning electron micrographs of (left) a lotus leaf [23] and (right) a hydrophobic surface patterned regularly with posts [25].

et al. [26]. An example is reported in figure 2.2 (right). However, it has been recently shown than neither the regular patterning, nor the intrinsic hydrophobicity [27; 28] of the material are an absolute requirement to promote superhydrophobicity. Several authors have even shown the possibility of fabricating multiscale roughness [20; 21; 22] to mimic those found in nature.

2.4 Cassie and Wenzel models

There are two ways in which superhydrophobic behavior can occur. When the drop is suspended on top of the surface roughness, as shown in Fig. 2.3 (a), the substrate is effectively a composite of liquid-solid and liquid-gas sections. If the length scale of the posts is much smaller than the drop size, the effective liquid-substrate surface tension is given by $\Phi\sigma_{ls} + (1 - \Phi)\sigma_{lg}$, while the effective gas-substrate surface tension is given by $\Phi\sigma_{gs}$,

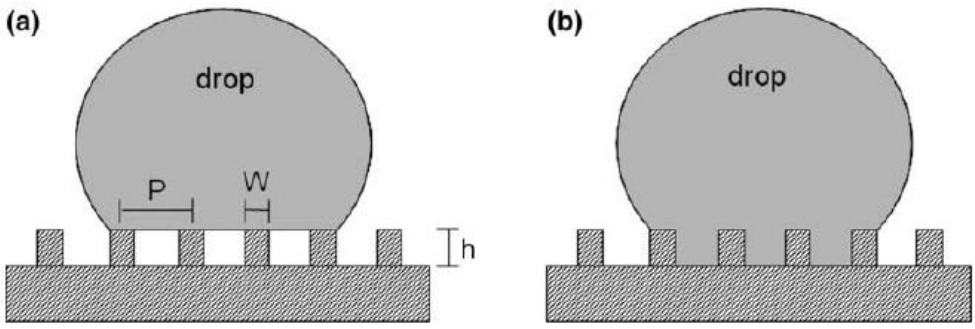

Figure 2.3: Schematic illustration of water drops on hydrophobic microstructured surfaces. (a) Cassie state, (b) Wenzel state .

Here Φ is the solid (area) fraction of the substrate on top of the posts. Substituting these to the Youngś equation (Eq. 2.1), we obtain the so-called Cassie-Baxter equation [29]

$$\cos\theta_{CB} = \Phi\cos\theta_e - (1-\Phi) \tag{2.5}$$

This state is called the suspended or Cassie-Baxter state.

In the case of a more general rough surface characterized by disordered asperities of the same matherial (fig. 2.4) the Cassie - Baxter equation should be modifiad into eq. 2.6

$$\cos\theta_a = A_{\mathrm{spec}}(1-f)\cos\theta_e - f \tag{2.6}$$

where A_{spec} is the specific area, determined as the ratio between the real surface and its projection on the plane, and f is the ratio of the surface occupied by air bubbles (pores). This picture is valid only if the matherial which asperities are made is slight hydrophobic ore more ($\theta_e > 90^\circ$). In this case capillary pressure prevents from the infiltration of liquid into the pores.

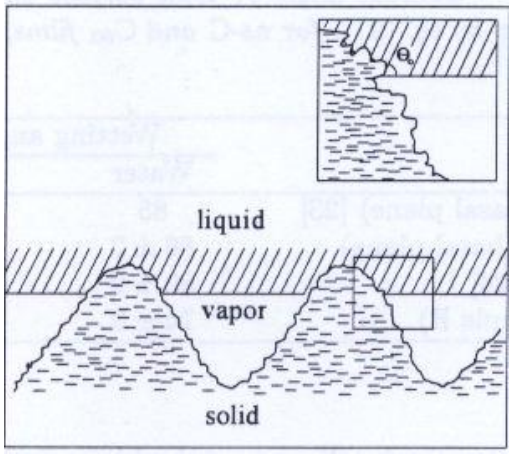

Figure 2.4: Schematic illustration of the solid - liquid interface with formation of bubbles of trapped air in the case of a generical rough surface [31].

In the case of a flat heterogeneous surface the Cassie - Baxer equation can be extended the Young-Dupré equation (2.7). Here the liquid is assumed to be in contact at the same time with portions of surface characterized by different wettabilities.

$$\cos\theta_a = \sum_i f_i \cos\theta_i \tag{2.7}$$

where the f_i are the surface ratios of intrinsic contact angles θ_i ($\sum_i f_i = 1$).

On the other hand, if the liquid drop fills the space between asperitiess, both the liquid-solid and gas-solid contact area are increased by a roughness factor r. In the case of homegeneaous disordered roughness r is given by the specific area A_{spec} In this case, the macroscopic contact angle is given by the Wenzel equation [30]

$$\cos\theta_W = r\cos\theta_e \tag{2.8}$$

This state is called the collapsed or Wenzel state. Both the Cassie - Baxter and Wenzel state are (local) minimum of the free energy, but there is often a transition between them, opposed by a finite energy. The magnitude of the energy barrier has been shown to depend on both the size of the drop and the roughness of the surface [32; 33] and Kusumaatmaja et al. [34] explored a mechanisms by which the drop spontaneously collapses. The question of how and when collapse occurs is important because, even though both states show high values of the contact angle, many of their other physical properties like contact angle hysteresis are very different: while in the Cassie state the pinning is not relevant and the hysteresis is minimal, in the Wenzel state the droplet is stogly pined to the substrate and the hysteresis is very high: In the collapsed state the advancing contact angle is similar to the one in the suspended state, while on the other hand the receding angle may be very low.

2.5 Line tension effects

The three phase contact line corrugation, as a consequence of he presence of defects on the substrate, may in principle influence the contact angle by adding an excess of energy to the total amount of the system. A schematic representation of this situation is reported in fig. 2.5.

A better understanding of this situation comes from a generalized Young equation, proposed by Boruvka and Neumann [35]:

$$\sigma_{sv} - \sigma_{sl} = \sigma_{lv}\cos\theta_a + \sigma_{slv}\chi_{vs} \tag{2.9}$$

where σ_{slv} is the three phase line tension and $\chi_{vs} = 1/R$ is the curvature of the three phase contact line. The three phase line tension may be thermodinamically defined as

$$\sigma_{slv} = \left(\frac{\partial G}{\partial L}\right)_{T,N,A} \tag{2.10}$$

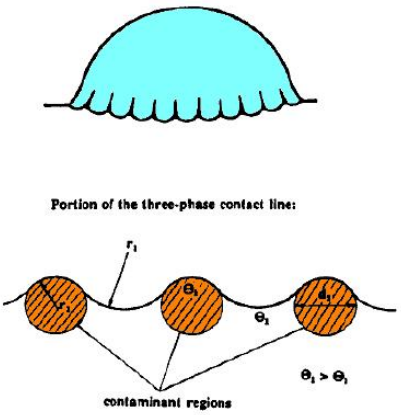

Figure 2.5: Schematic representation of three phase contact line corrugation.

where G is the free energy of the system, and T, V, A are Temperature, volume, interfacial area and three phase contact line length respectively. Taking account of the contact line tension the Cassie equation is modified into eq. 2.11 (see fig. 2.6).

$$\cos\theta_a = \sum_i f_i \cos\theta_i - \left(\frac{1}{\sigma_{lv}}\right) \sum_i f_i \sigma^i_{slv} \chi^i_{vs} \tag{2.11}$$

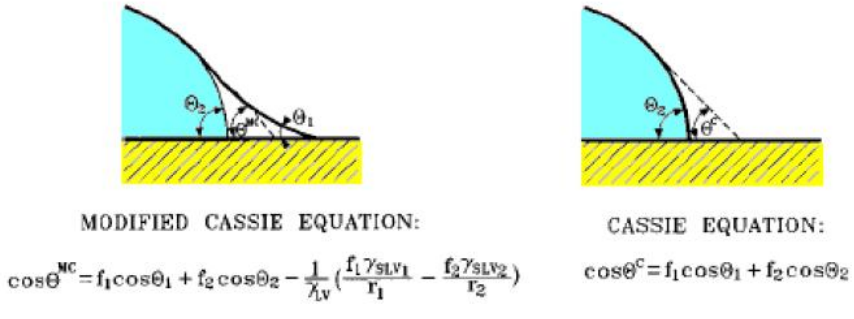

Figure 2.6: Effect of the contact line tension correction on the measured contact angle [36].

Theoretical values of σ_{slv} predicted on the base of the energy excess on the triple junction, are of the order of $10^{-11}N$ and $10^{-10}N$, while experimentally are found values of $\sigma_{slv} \sim 10^{-9}N$. As a consequence contact line tensions should be taken into account if the curvature deformation is

lower than the nanometric scale, while with macroscopic corrugations ($\sim 1 - 10\mu m$ or greater), it can be neglected. Anyway we point out that all surface details influencing the droplet shape are that in proximity of the triple phase contact line. In this way if we assume a statical droplet configuration and we neglect the way this configuration is reached, all surface portions far from the contact line, both under the liquid and the air, are not relevant for determination of the equilibrium shape.

2.6 Anisotropic wetting

In previous sections we have seen how geometrica(roughness) and chemical heterogeneity intluence the wetting behavior, and in particular the estimation of the contact angle. The common character of all these models is to be homogeneous and isotropic, which means that the surface details influence the droplet behavior in the same way independently from the direction from what the droplet is observed along the plane. In this case if gravity is neglected the droplet assumes an almost spherical shape. If the roughness is not isotropic, e.g. parallel grooves, the drop is elongated in the direction parallel to the grooves and the apparent contact angles measured along the principal directions of the patterned surface are different. An impressive demonstration of such dissimilar behaviors is provided by the leaves of lotus and rice plants: in the former case, a water drop assumes an almost spherical shape, while in the latter the drop is markedly stretched out along the raphes parallel to the stem on the leaf [24].

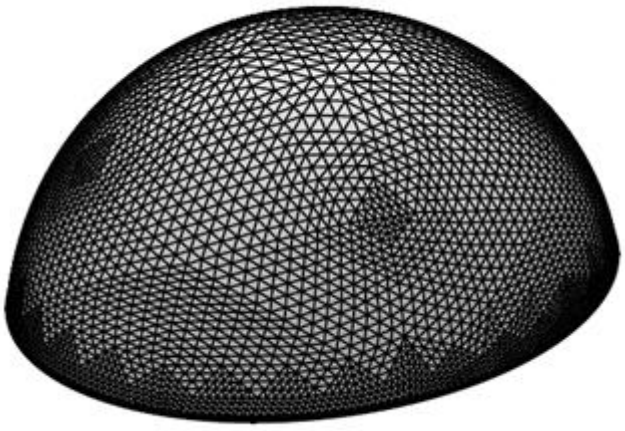

Figure 2.7: Global view of an anisotropic droplet obtained with a Surface Evolver simulation.

Advances in fabrication techniques allow the realization of very controlled patterns at the micron/nano-scale which produce isotropic, super-hydrophobic surfaces, with a water contact angle greater than 150° [38; 16; 39; 26; 40]. Such surfaces have attracted a lot of attention as an ideal playground to study fundamental issues at the solid-liquid interface [25; 42; 43; 44] and for practical applications [45; 46; 47]. More recent studies have focused onto the wetting properties of anisotropic patterned surfaces. It was observed that even relatively simple surface topographies such as grooves with rectangular cross section exhibit a large variety of different wetting morphologies [48]. Analogously, chemically heterogeneous flat surfaces formed by alternating hydrophilic/hydrophobic stripes show pronounced anisotropic contact-angle hysteresis [96; 97; 11; 12; 98].

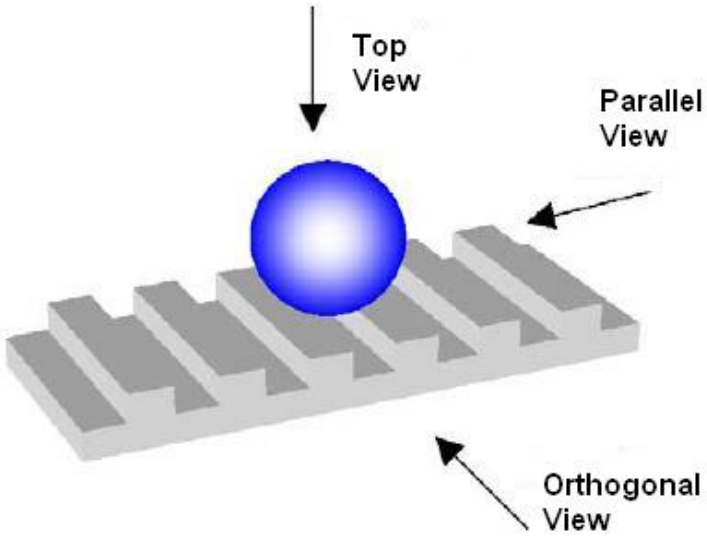

Figure 2.8: Schematic of a sessile drop on a substrate with horizontal grooves.

Recently the shape of water drops deposited on patterned PDMS substrates was simulated with the Surface Evolver and complemented by contact angle measurements[99]. For such composite hydrophobic drops, i.e. drops that do not wet the grooves of the structured surface, the apparent contact angle in the direction perpendicular to the pillars $\theta_\perp$ and that in the direction parallel to the pillars $\theta_\parallel$ are different and both are larger than the intrinsic value of the substrate material. If a drop is deposited on a grooved substrate, the liquid tends to expand in every direction, but it finds periodically energy barriers in its motion across the channels, while it is ideally free to move along the parallel direction. Accordingly, the drop is typically trapped in a state where it resides on fewer pillars compared to a spherical composite drop on the rough surface. As a result, $\theta_\perp > \theta_\parallel$. This is

a consequence of the squeezing and pinning of the drop in the perpendicular direction and of the stretching of the drop along the grooves.

More recently, the anisotropy of water drops deposited on tunable micro-wrinkled surfaces was studied as a function of the surface roughness[100]. Again, it was found that $\theta_{\perp} > \theta_{\parallel}$. Furthermore, $\theta_{\perp}$ increased with the surface roughness because of the pinning of the contact line. Vice versa, $\theta_{\parallel}$ decreased with the surface roughness as a result of preferential spreading due to roughness-enhanced wetting (Wenzel behavior). An important conclusion of this work was that the change of contact angle on a real rough surface is significantly affected by the nature of the three-phase contact line structure, rather than by simply increasing surface roughness. Similar findings were observed in experiments and numerical simulations based on the lattice Boltzmann method on the spreading of liquid drops on hydrophilic surfaces patterned with sub-micron and micron-scale parallel grooves [85]. It was found that the final drop shape is highly dependent on the path by which it is achieved. Drops that advance across the surface are elongated parallel to the grooves whereas drops that dewet the surface are elongated perpendicular to the grooves. Again, this behavior was explained in terms of pinning of the contact line on the groove edges. However, as the authors pointed out, the contact angle data was very noisy, underlining the prevalence of hysteresis on patterned surfaces.

2.7 Discussion

In this chapter we have briefly introduced the standard moldels describing wetting behavior in simple hydrophilic / hydrophobic systems. In that situations where gravity can be neglected, on a flat homogeneous surface the Young equation represents a good model, while the introduction of chemical heterogeneities requires a model of composte wetting, which is the Cassie - Baxter one. If the surface is rough and the liquid always touch the surface, a good model is that proposed by Wenzel, while if some air remains trapped into the asperities, may raise the phonomenon of superhydrophobicity, which may also be explained in terms of the Cassie - Baxter model. Another phenomenon related with surface heterogeneities, is the contatc angle hysteresys, which makes not univoque the determination of the correct contact angle in presence of defects. Defects are also related with the presence of a line tension along the three phase contact line.

All these models suppose an isotropic surface. The introduction in the last years of micrometric patterning of chemical stripes and geometical grooves, makes the situation much more complicated and anisotropy has caused a great interest recently. In the last section of this capter we have briefly collected the mai results of literature on this topic.

Chapter 3

Microfabrication

In this chapter we introduce some of the most common techniques used in the production of the samples for the experimental studies of this work. In order to study quantitatively the anisotropic wetting we produced a set of samples with the as wide as possible variety of intrinsic wetting properties. What is primarily needed in this work is a well defined aspect ratio for structures of the size of hundred of microns and a stable control of the wetting behavior on the flat surface.

For this purpose we produced samples which involved different materials and fabrication techniques. Materials are (in decreasing order of surface energy) stainless steel, thiolene resins (NOA) , polimetimetacrylate (PMMA) and polydimethylsiloxane (PDMS). Stainless steel structures are obtained with microelectroerosion process, PMMA structures are obtained via mechanical micromachining, NOA structures are obtained via standard photolithography techniques, while that in PDMS via double replica molding starting from the stainless steel samples used as masters.

In the following sections these processes, and techniques are briefly introduced in separate topics Finally the detailed results of the fabricated samples are reported.

3.1 Sample Cleaning and Preparation

An accurate cleaning of materials and components is the first step in sample fabrication. Many developments were made to avoid this problems, and currently it is common to work in a clean-room environment while processing microfabrication. In a clean room the presence of particulate is reduced and controlled, as indicated by the class (in a class 1000 clean-room there can be at most 1000 particles of diameter 0.5 μm per cube feet, which corresponds to $\approx$ 35000 particles per m^3), and clearly a class 100 is 10 times better the a class 1000 clean-room. To clean the sample, routinely procedures are applied, using acids and/or other oxidant agents (ozone) to remove contaminants from the surface.

To produce samples and masters for replica molding the first step is to clean a glass slide. A

microscope slide (Menzel glass) is washed with water and soap, then with ultrapure water, and finally with ethanol and acetone, to remove dust particles and contaminants.

Figure 3.1: UVO-Cleaner apparatus, Jelight Inc, model 42-220.

After that, the glass is dried with N_2, and then it is cleaned in a UVO-Cleaner apparatus (Jelight Inc., model 42-220), in which a mercury lamp produces UV radiation (with $\lambda_1 = 184,9nm$and $\lambda_2 = 253,7nm$). Molecular oxygen strongly absorbs radiation at $184,9nm$ and dissociates to produce atomic oxygen, which interacts with O_2 to produce ozone. The $253,7nm$ radiation is absorbed by the largest part of contaminants on the glass surface (hydrocarbons), that interact with ozone to produce volatile molecules (CO_2 and H_2O) [49]. Schematically:

$$\frac{3}{2}O_2 + h\nu(184,9nm) \longrightarrow O_3 \tag{3.1}$$

$$\mathrm{H}ydrocarbons + O_3 + h\nu(253,7nm) \longrightarrow CO_2 + H_2O \tag{3.2}$$

These steps produce a clean surface, with exposed superficial $-OH$ groups, due to the strongly oxidant environment. After this process, the samples can be stored for a long time.

3.2 Silanization

The silanization technique absolves to the double function of tuning the original hydrofobicity of a given surface and of realizing antistick surfaces (i.e. common glass slides) useful in photolithographic processes. The process is also essential in double replica molding. It consists in the formation of a Self Assembled Monolayer (SAM) of a silane on the surface. Two molecules were utilized: octadecyltrichlorosilane ($H_3C-(CH_2)_{17}-SiCl_3$, commonly known as OTS) and $1H,1H,2H,2H$ - perfluoro octyltrichloro silane ($F_3C-(CF_2)_6-(CH_2)_2-SiCl_3$, TPOS). As shown in figure 3.2 both of them are molecules with a long chain (alkylic with eventually fluorine atoms) and a reactive head (with three chlorine atoms).

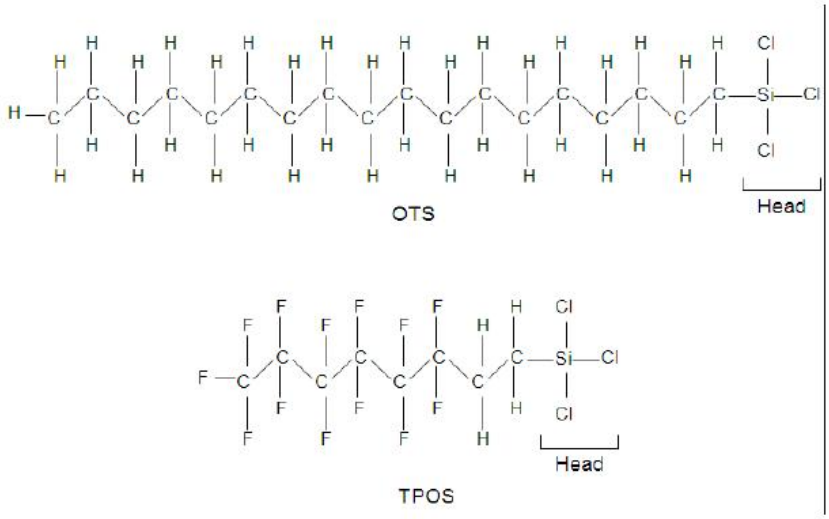

Figure 3.2: Chemical formula of OTS and TPOS, the two silanes used to produce anti-stick glass slides. For both these molecules The reactive head is indicated.

The master is first treated for 30 minutes in UVO-Cleaner, wetted with ultrapure water, lightly dried with nitrogen and then put in contact with the silane vapors. At this point the surface is covered by -OH groups and by a thin water layer (some molecules thick). When the silane approaches the surface, its chlorine atoms are hydrolyzed by water:

$$R-SiCl_3+H_2O \longrightarrow R-Si(OH)_3+3HCl$$

The molecules are then adsorbed on the surface, by hydrogen interaction with the superficial -OH groups, and the same between adjacent molecules. This unstable situation evolves with water elimination, that produces a stable network as shown in 3.3. In this situation the surface is com-

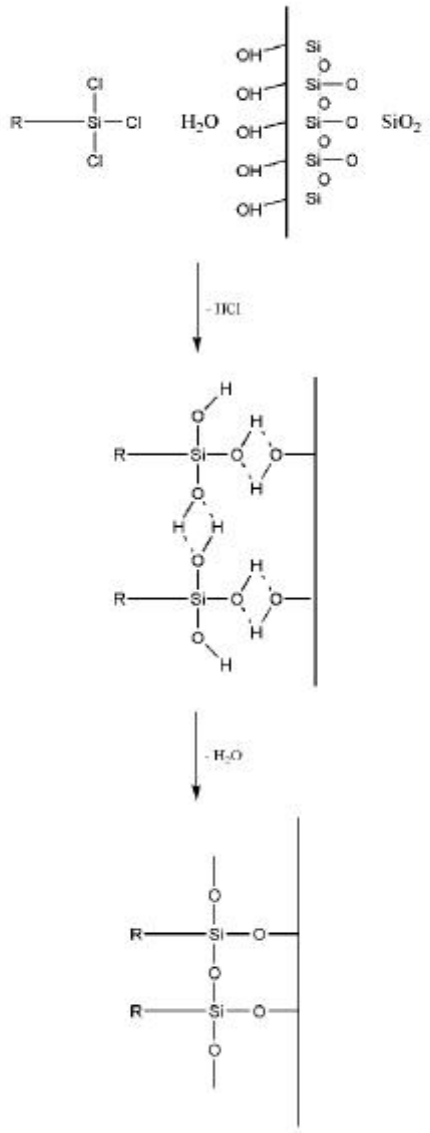

Figure 3.3: Schematic representation of the reactions involved in silane Self Assembled Monolayer formation.

pletely covered by a Self-Assembled Monolayer of silane molecules (for an accurate description of SAMs see for example ref. [51]), and the wetting properties change from hydrophilic glass to hydrophobic due to the alkyl or fluorinated chains.

Practically, a small quantity $(80 - 160\mu l)$ of silane is put inside a vessel, in a low-vacuum chamber. The glass slide is put on top of the vessel. A rotative pump provides a low vacuum $(\sim 10mbar)$, and the system is equipped with a liquid nitrogen trap to prevent HCl vapors to interact with the pump. After 1 hour, external pressure is introduced inside the chamber by nitrogen or air reflux. After this treatment the surface becomes hydrophobic, acquiring antistick properties, due to its low surface energy.

3.3 UV Lithography

Lithography is one of the most important micromachining techniques [52]. The traditional field of application involves the production of silicon microchips and integrated circuits [53].

Lithography is a process used to transfer a pattern from a photo mask (which can be a polymeric sheet or a metal deposited on a piece of quartz) to a light sensitive material, which is commonly known as a *photoresist*. When we expose this material to an appropriate radiation, we have two possibilities:

- if we are working whit a *Negative photoresist* , it will reticulate only in the areas exposed to light (becoming hard), while the unexposed material can be easily removed using an appropriate solvent
- if we are working with a *Positive photoresist* the exposed areas will be removable, while the unexposed ones will remain unwashable.

When we want to produce small and isolated structures, it is better to use a negative photoresist, while for channels or great areas a positive photoresist will be more suitable. A schematic representation of the two kinds of photoresist is shown in figure 3.3. It also suggests that in the common situation we have a bulk material (e.g. silicon), a thin film (native or induced silicon dioxide) and the photoresist.

What is to be underlined is that the maximum resolution that can be obtained is given by eq. 3.3:

$$R = b_{\mathrm{m}in} = \frac{3}{2}\sqrt{\lambda\left(s + \frac{z}{2}\right)} \tag{3.3}$$

in which λ is the radiation wavelength, s is the distance between the mask and the photoresist surface, and z is the resistś thickness. If masks with pattern dimensions lower than $b_{\mathrm{m}in}$ are used,

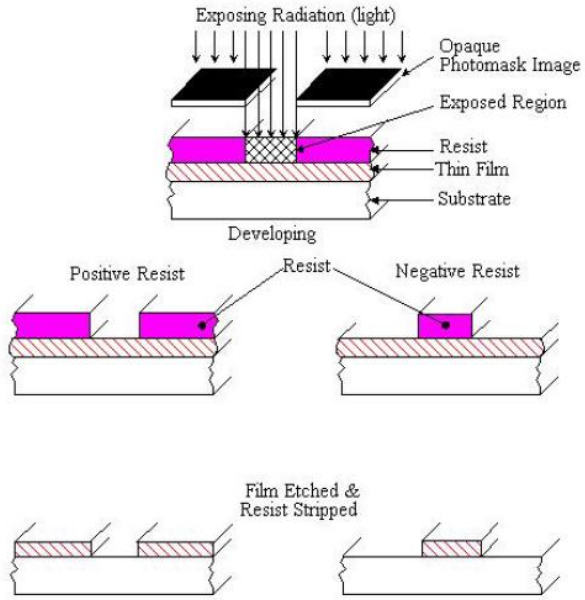

Figure 3.4: Representation of a negative and positive resist behaviour

a bad result is obtained due to the presence of diffraction. Using contact printing technique (in which $s \approx 0$), a typical wavelength of about $400nm$ and a resist thickness of $1\mu m$ we obtain a resolution of about $1\mu m$. With more sophisticated techniques (using deep UV radiation and improved resists) a resolution of about $100 - 200nm$ can be obtained, which is very high (even too high) compared with the typical dimensions of microfluidic devices.

3.4 Etching and anodic bonding

The area not covered by the pattern is usually removed by wet or dry etching. The chemical technique consist in a selective reaction that occurs only with the wafer material (for example silicon or SiO_2) and not with the resist material (which acts as a mask). A great number of combinations (bulk material/resist/etchant) have been studied and improved. Depending on the bulk material we can have isotropic etching (for glass and polysilicon) and anisotropic etching (for monocrystalline silicon). In the former case the result is a pattern with rounded edges, in the latter case edges are sharp.

To etch glass hydrofluoric acid (HF) solutions are commonly used. HF has a specific interaction with SiO_2, which is the main component of glass, with the following reaction

40% NH_4F: 49% HF Volume Ratio	HF Conc., %	Specific Gravity @25°C	Etch Rate @21°C, Å/Min.	Freezing Point, °F
4:1	9.9-10.2	1.115	1740-1840	76
5:1	8.2-8.5	1.113	1020-1120	64
21:4	7.9-8.2	1.113	970-1070	63
6:1	7.0-7.3	1.112	860-930	56
25:4	6.8-7.1	1.112	830-900	53
13:2	6.5-6.8	1.111	790-860	52
34:5	6.3-6.6	1.111	765-835	50
7:1	6.1-6.4	1.111	735-805	49
8:1	5.4-5.7	1.110	640-710	44
9:1	4.9-5.2	1.110	575-645	40
10: 1	4.4-4.7	1.109	510-580	37
12: 1	3.8-4.1	1.109	435-505	32
15:1	3.0-3.3	1.108	345-395	30
20:1	2.3-2.6	1.107	265-315	26
25:1	1.8-2.1	1.107	205-255	25
30:1	1.5-1.8	1.106	185-215	22
40:1	1.1-1.4	1.106	140-170	21
50:1	1.0-1.1	1.105	125-145	20
100:1	.45-.55	1.105	65-85	20

Figure 3.5: Standard BOE Etchant characteristics for different compositions [50]

$$SiO_2 + 6HF \Leftrightarrow H_2SiF_6 + 2H_2O \tag{3.4}$$

The reaction rate (and so the etching rate in terms of depth/time) depends principally on HF concentration and on solution temperature. To avoid a decrease in etching rate due to HF consumption during the reaction, glass etching is usually done with a buffered solution, obtained by mixing HF (which can be found in aqueous solution) with an aqueous solution of ammonium fluoride (NH_4F), obtaining the so-called *Buffered Oxide Etchant* (BOE). In aqueous solution NH_4F dissociates following the relation

$$NH_4F \Leftrightarrow NH_2 + HF \tag{3.5}$$

providing a constant concentration of HF, and consequently a constant etch rate with time. Depending on BOE composition, etch rate varies as described in figure 3.4

The temperature dependence of etching rate is described in figure 3.4. It should be noted that the etching reaction is thermally activated, so increasing the temperature it increases the etching rate. One thing that has to be considered is the expansion coefficient of glass and masks, which are usually different, so great care should be used with high temperature, to avoid the resist detachment.

Another solution to produce microstructures is to use dry etching. When performing dry etching, the material is exposed to an ion bombardment (e.g. in a nitrogen or oxygen plasma), that selectively removes only the unexposed parts. This technique provides good resolution and reproducibility, even if costs are extremely increased by the necessity to produce and control a plasma. After the formation of channels by etching, these first microfluidic chips were usually sealed using methods such as anodic bonding, in which a silicon wafer and a glass wafer are bonded together at elevate temperatures ($\approx 400°C$) and high voltages ($\approx 1kV$).

In figure 3.4 is reported a scheme of the main photolitographic steps using both positive and negative resists.

3.5 Photolitography with thiolenic resins

Usually the resist is used as a mask in the following etching process, but it may also constitute the final structure. This second method of photolithography has been implemented directly in our laboratory. It is useful in the production of samples with patterns in relief of large dimensions, of hundreds of micrometers. The structure has been produced with a negative resist which consist s of a thiolene resin used as an optical adhesive, commercially available by Norland Products as a prepolymer and that, under UV exposure, polymerizes becoming hard and transparent, with a reaction that involves a *thiol* group $(R - SH)$ and an *ene* group (the double bond $H_2C = C - R'$

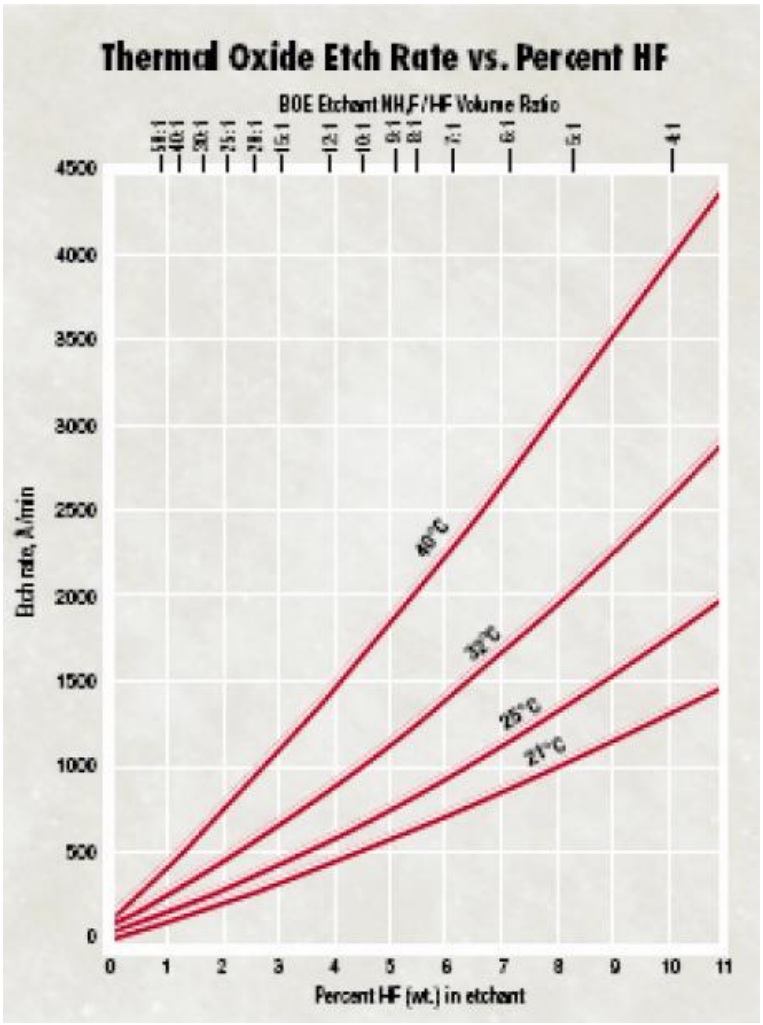

Figure 3.6: Etch rate of different BOE solutions with increasing temperature [50]

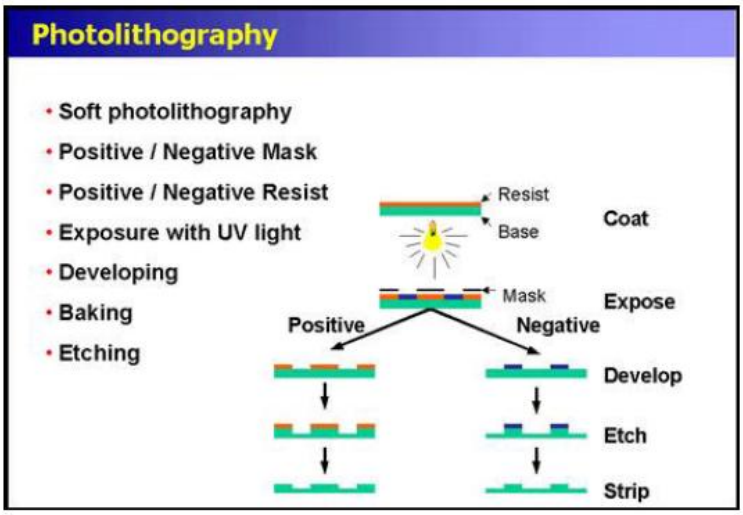

Figure 3.7: Schematic description of the photolitographic process with positive and negative resists

). In figure 3.8 the $h\nu$ indicates that the reaction takes place if the prepolymer is exposed to UV radiation.

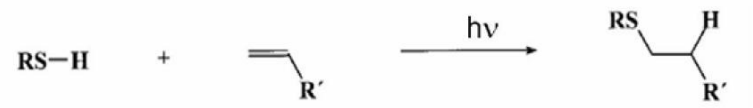

Figure 3.8: Polymerization process under UV exposure.

The commercial name is Norland Optical Adhesive (NOA) followed by a number which indicates different adhesive characteristics (i.e. viscosity). The adhesive has a transmission spectrum that shows no adsorption in visible light, while has an adsorption peak around 365nm. As example in figure 3.9 is reported the transmission spectrum of NOA61. The photopolymerization reaction can be described as a four-steps process, as shown in 3.10, which consists in the typical initiation, propagation (2 steps) and termination processes. It is a frontal phopolymerizzation, because UV light is absorbed principally by the first layer of uncured prepolymer and only a little part of radiation arrives to deep uncured prepolymer.

Time needed to have complete polymerization depends principally on the adhesive thickness, but many other parameters (lamp power, lamp distance, external temperature, etc ...) have great influence. The kinetic of frontal photopolymerization has been investigated by Douglas et al. [55; 56] and they showed that there is an empirical relation between the patterned height h (position

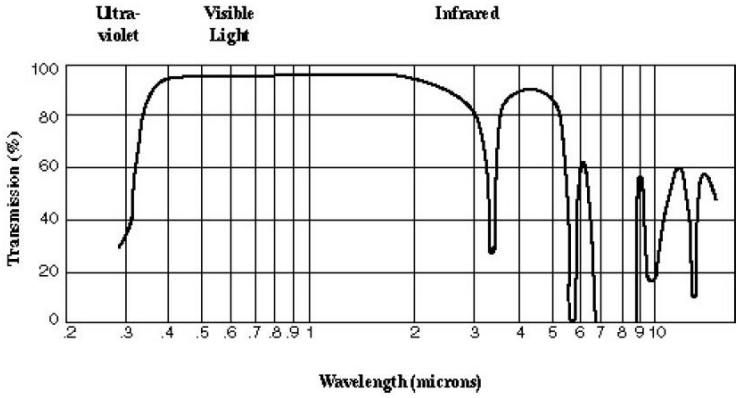

Figure 3.9: Trasmission spectrum of NOA 61. Note that in the visible region the transmission coefficient is close to 100%, while in the UV region an absorption peak is centered around 365 nm.

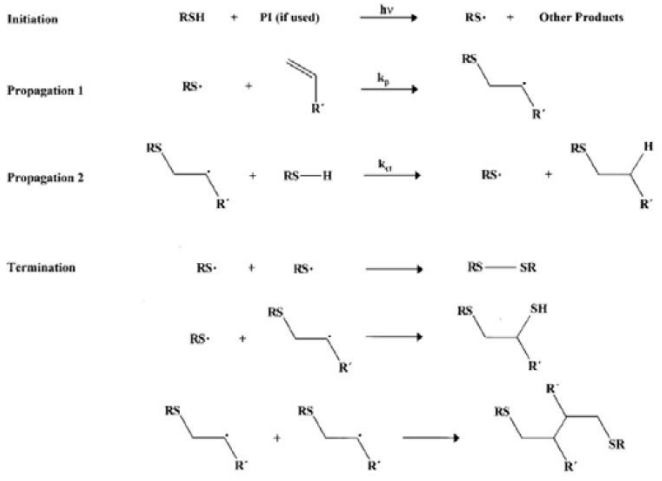

Figure 3.10: Process of radical photopolymerization of thiolene resins. The four steps are here represented, showing the three possibilities for termination [54].

at which the solid liquid interface is placed) and time. This relation is exposed in equations 3.6 and 3.7.

$$h(t, \bar{\mu}, KI_0, \phi_C) = \frac{\ln(t/\tau)}{\bar{\mu}} \tag{3.6}$$

where

$$\tau(KI_0, \phi_C) \equiv= \frac{\ln[1/(1-\phi_C)]}{KI_0} \tag{3.7}$$

in which: ϕ_C is the critical conversion fraction ($<< 1$) of monomers at which the partially converted material becomes a solid; K is the reaction conversion rate (assumed constant and expressed in $cm^2(Js)^{-1}$); I_0 is the lamp intensity; $\bar{\mu}$) is the effective optical attenuation coefficient, obtained from the arithmetic mean of the attenuation coefficient of the unexposed monomer (μ_0 and fully polymerized material (μ_∞).

Another feature of thiolene resins is the possibility to adhere to a variety of surfaces, including metals and glass, this explains its use as an adhesive. The uncured prepolymer has to be removed after the UV exposure. Two solvents are commonly used: ethanol and acetone [57]. The former has only a mechanical effect, while the latter has also a chemical effect, because the prepolymer is soluble in acetone.

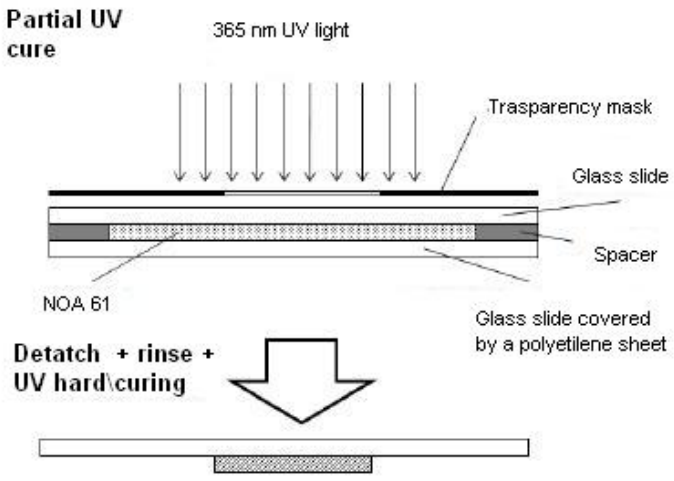

Figure 3.11: Schematic representation of the fabrication of a master using thiolene resins.

The UV treatment in photolithography is schematically represented in figure 3.11: the support glass slide is put on top of a UV-absorbing film (UV-Sun Blocker, Unisol, PD, IT), covered by a

polyetilene antistick sheet. On it two spacers (of desired thickness, ranging from $250\mu m$ to few millimeters) are placed, and some thiolene prepolymer (NOA 61) is poured. The cleaned glass slide is gently put on top of the prepolymer, to avoid air bubbles formation. Then the adhesive is partially polymerized across a photomask (designed with Canvas Software and printed by Cleup PD, Italy [59]), exposing it to a UV lamp (Spectronics Corp., model SB-100P) light for a few minutes, at a distance of 60cm from the lamp. The time needed for this first treatment (referred as *Pre-curing*) depends on the adhesive thickness. As an example for $100\mu m$ it is about 5 min.

After the pre-curing, the stack is disassembled, accurately stretching the polyetilene sheet, and unpolymerized adhesive is washed away using ethanol and / or acetone. Using only acetone allows better removal, but can cause problems (for example detachment of NOA structures from the glass slide) in the hard curing or silanization passage. After this, the layer is cured for a longer time: this second treatment (referred as *Hard-curing*) needs a time ranging from 30 minutes (for a 100ìm thick adhesive), up to a few hours for thicker layers. It should be noted that these passages can be done even in a normal laboratory, with no necessity of special equipment (clean/yellow/dark room).

3.6 Polymeric structures made by Soft-Lithography (PDMS)

A great development in microfluidic devices production came in the 1990s, with the appearance of soft-lithographic techniques. Soft lithography represents a non photolithographic strategy to miniaturization, using for example self assembly, microcontact printing and replica molding for creating micro and nano structures [60]. The key concept is that if we have a micromachined master and we pour on it a prepolymer, after curing we can obtain microstructured polymeric blocks without photolithographic processes. This master (stamp or mold) for replication can be produced with traditional silicon-based micromachining technologies. After this first step a UV (or X-ray) lithography equipment is not needed, and a large number of devices can be produced simply by replication of the original master. This approach, with the relatively low costs of prepolymers, make soft-lithography a cheap technology and allows a great productivity.

Polymers are materials constituted by relatively large molecules (in some cases called *macromolecules*), which are made by the repetition of small units (called *monomers*). These monomers create (in general) long linear molecules, with eventually the possibility to produce ramifications and reticulations. In a polymeric material these molecules are tangled together, and interact by intermolecular forces (Van der Waals or dipolar forces) that are weak for a single monomer, but can become great for a macromolecule by addition of single interactions.

The molecular nature of polymers affect their properties, especially for what concerns mechanical behavior with temperature change. At low temperature a polymer tends to be rigid, since

thermal energy is much lower than interaction forces between molecules. In this situation the state is a mix of crystalline domains and amorphous regions, because it is very difficult to arrange an ordered structure using monomers in long chains. The relative size of crystalline regions depend on the nature of monomers (dimensions, rigidity, side groups etc.) and on the regularity of the polymer (ramifications and reticulations). In general if the chains have high mobility, they can arrange in a ordered network. Even with small monomers and linear chain polymers, the crystalline fraction is not more than 40%.

Increasing the temperature we find a critical value, the Glass Transition Temperature (Tg) over which the chains start to become more mobile, even if the material is still rigid. It is a second order transition, which involves only the amorphous part of the polymer. At $^\circ > T_g$ if the material is subjected to an external deformation, it tends to change its shape and to maintain it if temperature is decreased under the Tg. This behavior can be explained by the possibility for chains to slide one on the other but keeping their interactions that provide rigidity. There are three main classes of polymers:

- If the polymer is made by linear inert chains, and has a significant crystalline fraction, when it reaches the Melting Temperature (Tm) it becomes liquid. In this situation the crystalline regions dissolve, similarly to the fusion of crystalline materials. This configuration is typical of *Thermoplastic Polymers*, which can be modeled more than one time, and a device can be modeled even after its formation. Some examples are Polyethylene (PE) and Polystyrene (PS).

- If monomers have reactive groups (for example double bonds), increasing the temperature tends to increase the reticulation, thus making the material more rigid. This is the behavior of *Thermosetting Polymers*. These polymers can be formed only one time, and it is impossible to change the device shape after reticulation. An example of this kind of polymers are the Epoxy resins.

- If the polymer is made starting from a liquid prepolymer (made by relatively large molecules, called *oligomers*) which is then reticulated by a chemical reaction between the chains (or eventually using a reticulant agent), it tends to behave as an *elastomer*, which is deformable but returns to its original shape after the external load is removed. Some examples are Polybutadiene (BR) and Polyisoprene (IR).

What is very important to underline is that varying the monomer structure (with different side groups or chain constituent groups) or the monomers ratio (in copolymers) it is possible to change both the material Tm and Tg. This provides a great versatility for polymeric materials and, with monomers costs that are usually very low, explains why polymers are commonly used in modern

technology. The principal polymeric material utilized for microfabrication is polydimethylsiloxane (PDMS), a polymer with inorganic chains (siloxanes) but organic side groups (methyl groups). A representation of the typical PDMS chain chemical structure is shown in figure 3.12. platinum catalyst) and thermally curing. After curing it becomes a transparent, flexible elastomer, which has a Tg around $\sim -120°C$ and a Tm more than $200°C$ PDMS devices are commonly produced using Replica Molding, which is a technique that consists in the replication of a master, obtained pouring a liquid prepolymer on it and then promoting reticulation. A simple scheme of this approach is shown in figure 3.13.

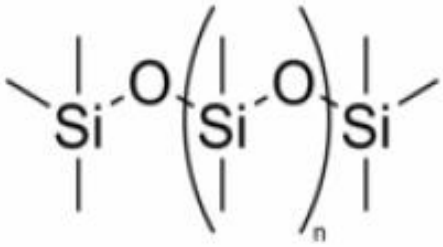

Figure 3.12: Representation of the chemical structure of PDMS, with an inorganic chain ($Si - O - Si$) and organic side groups ($-CH3$).

Masters are produced with common photolithographic technique using silicon, glass or photocurable polymers, and micro electrical discharge machining of stailess steel. To promote the detachment of the polymeric replica, an antistick Self Assembled Monolayer is placed on the master before its use (silanization technique), avoiding the formation of chemical bonds between the prepolymer and the material constituting the master. After that the prepolymer is poured on the master, cured and then released.

3.7 Micro electrical discharge machining

Micro electrical discharge machining, is a thermal process for contactless material removal of electrically conductive materials. In micro EDM the machining of conductive materials is performed by a sequence of electrical discharges occurring in an electrically insulated gap between a tool electrode and a workpiece. During the discharge pluses, a high temperature plasma channel is formed in the gap, causing local melting and evaporation of workpiece and electrode material. The machining forces are negligible compared to those in mechanical material removal processes. The removal of material from the tool electrode and workpiece occurs in discrete units corresponding

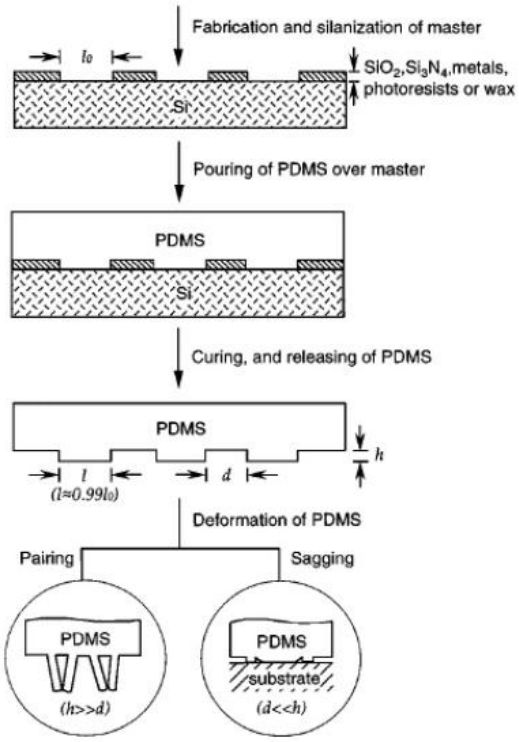

Figure 3.13: Schematic representation of Replica Molding Technique and of possible problems for the polymeric replica if structures are too close (Pairing) or too far-between (Saggling)[60].

to each discharge and, for a given couple of tool and workpiece materials and dielectric fluid, is proportional to the discharge energy. Differently from wire micro electrical discharge machining or sinking micro electrical discharge machining, in micro EDM milling micro electrodes, essentially consisting of cylindrical rods with diameters down to 10 microns, are driven along defined paths while rotating, in a way similar to conventional 3 axis milling. The electrodes can be shaped to the desired diameter by means of a wire electro discharge grinding (WEDG) unit and workpiece material is removed layer by layer, with layer thickness ranging from few microns to 0.1 microns. Rapid tool profile stabilization allows wear correction to be performed by a one dimensional motion parallel to the electrode axis. Electrode wear compensation is therefore achieved by continuously advancing the tool electrode towards the workpiece, while moving along its path, with a constant wear ratio. The minimum machinable feature size and maximum accuracy are in the order of 10 m and 1 m respectively.

For the study of anisotropy the machined features consisted of a series of rectangular protrusions with length of $15mm$, height of $200\mu m$ and widths of $200\mu m$, $400\mu m$, $600\mu m$ and $800\mu m$ obtained from a stainless steel substrate, using electrodes in tungsten carbides with a diamenter of $300\mu m$. The surfaces of the steel substrate were initially in the ground condition. In order to improve the surface finish of the generated protrusions and avoid the influence of the surface texture anisotropy due to grinding, the substrate's surface was polished in several steps, following a procedure similar to the one used for preparation of samples for metallographic analysis. This operation also allowed the removal of irregularities possibly occurring at the features edges due to small amounts of recast material.

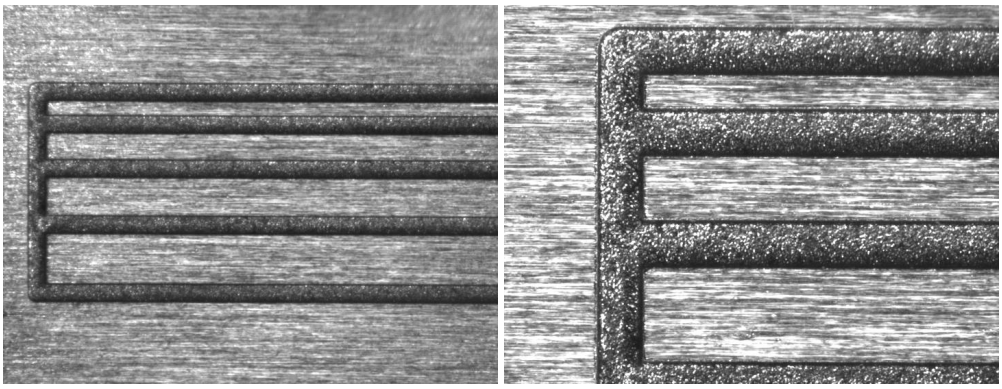

Figure 3.14: Top view of the rough micro EDM sample.

Chapter 4

Contact Angle Measurements

In this chapter we summarize some generalities on contact angle measurements and describe in detail our experimental apparatus and the procedures adopted to take the measures in the different experimental conditions find in static and dynamic measurements, and measurements on anisotropic droplets.

4.1 Introduction

Most of the experimental part of the work in this thesis regards an accurate measurement of-contact angles. A variety of methods has been developed in time ranging from force measurements like the Wilhelm-balance tensiometry (WBT) [61] to the traditional contact angle goniometry. Wilhelmy-balance tensiometry measures wetting forces along the perimeter of a regularly shaped object (typically a plate or cylinder) as it is immersed into or emerged from the wetting liquid (see ref. [62] for a brief tutorial). In goniometry, a back-lit drop (silhouette) is optically imaged and the angle subtended by the drop at the point of solid - liquid contact (on left and right sides) estimated with an optical goniometer (manual) or by image analysis (computerized).

Modern computerized instrumentation has greatly reduced labor and subjectivity of goniometric and balance techniques, but there are a number of analytical subtleties that can be easily overlooked in instrument setup and operation. For example, in goniometry, it is essential to establish an accurate baseline between the drop and surface and choose the correct point of contact. These two aspects are intertwined and both require that the observer must be looking down on the drop at a slight angle above (not below) the horizon. Otherwise, the base of the drop can be cropped by the horizon and finding the maximum profile width becomes highly ambiguous. In Wilhelmy-balance tensiometry, buoyancy correction requires accurate knowledge of the wetted perimeter and point of liquid - plate contact; both of which insist that the test plate or cylinder enter and exit the fluid perpendicularly.

Measurement of advancing and receding contact angles, θ_a and θ_r, respectively, is an essential aspect of tensiometry because these are the two reproducible angles that characterize wetting. No doubt WBT is the most accurate and least subjective approach to measuring hysteresis ($\Delta = \theta_a - \theta_r$) because the three - phase (solid - liquid - vapor) line is in wholesale motion, assuring achievement of maximal θ_a and minimum θ_r. As a consequence, WBT is a reasonable choice as a benchmark of comparison for goniometric methods [63].

Two goniometric methods widely applied in commercial instruments to measure θ_a and θ_r are the captive-drop goniometric (CDG) and tilting-plate (TPG) goniometric techniques. In CDG, a drop is held in place on a surface under study with a fine needle connected to a syringe. Advancing angles θ_a are read by slightly filling the drop, advancing liquid over the surface. Receding angles θ_r are read by removing liquid from the drop, receding liquid from the surface. Maximum θ_a and minimum θ_r is assured by incrementally increasing volume added or removed, respectively, until no change in angles is observed. Care must be taken with CDG to use a needle diameter that is a very small portion of the drop diameter. If the needle diameter exceeds a few tens of microns, drop shape can be significantly affected and introduce serious errors into the estimation of θ_a and θ_r.

TPG measures left and right sides of a drop as the surface under study is tilted with respect to the optical axis so fluid accumulates in the leading (advancing) edge of the drop and drains from the trailing (receding) edge. Maximum θ_a and minimum θ_r are attained when the drop is at a point of ' incipient motion ' ; that is, just at the point when the drop rolls out of the observation window. Needless to say, finding the point of incipient motion is experimentally inconvenient. A typical remedy for a particular surface under investigation is to plot observed contact angle against tilt angle to find a tilt smaller than required to induce drop rolling yet large enough that an incremental increase or decrease in tilt does not observably change left-and-right angles.

4.2 Experimental Setup

Our homemade apparatus is able to take measurements of static droplets residing on a surfaces, and advancing and receding contact angles both with the captive-drop (CDG) and tilting-plate (TPG) goniometry.

Figure 4.1 shows the scheme of the apparatus for deposition and measurements of small droplets. Droplets are deposited with a microsyringe pump (Ultra Micro Pump ||, World Precision Instruments), controlled by a pc. They are back lighted (Phlox) and images are acquired with a CMOS camera (Photon Focus MV-D1024). Several translator stages are positioned on the deposition plane and both on the syringe and camera supports. A rotator is placed on the measurement plane to easily orientate anisotropic droplets and a second one on its vertical support to

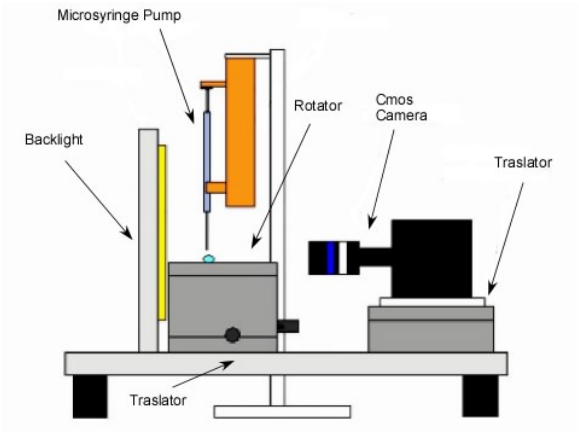

Figure 4.1: Schematic diagram of the Contact Angle goniometer.

tilt the surface. Image acquisition is managed by pc software (Silicon Software Microenable |||). Images are saved in .bmp 8 bits grey-scale format. Figure 4.2 show an image detailing the sample support stage of the the experimental setup.

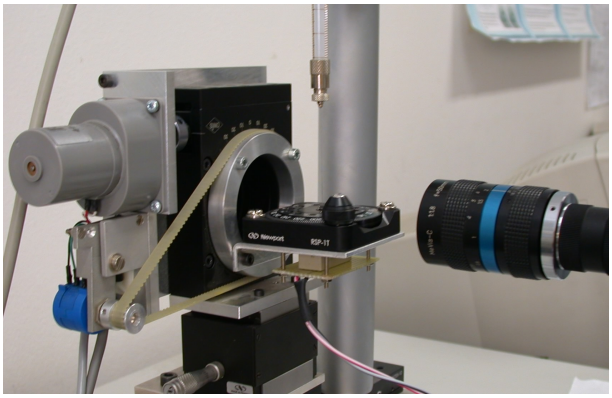

Figure 4.2: Detail of our home built Contact Angle goniometer.

4.3 Standard Measurement Procedure

The standard procedure for static contact angle measurements on isotropic surfaces involves repeated measurement of milli-Q droplets deposited on different portions of the sample. Usually a good statistics is given by at least 5 - 6 acquisitions. Image analysis is detailed described in section A. Advancing contact angles are obtained with Captive drop method. Images are acquired

in sequence and subsequently analyzed to the determination of the advancing value. An extensive characterization of behaviors is reported in section 4.6. The tilted plane configuration has been used for rolling droplets measurements.

4.4 Anisotropy Measurements

The principal kind of measurements performed with this setup is related with the droplet anisotropy. Anisotropy is defined by the simultaneous acquisition of droplet profiles at least in the two main directions, defined as orthogonal and parallel. The use of a single camera requires to take these images sequentially. In addition, evaporation effects strongly affect the amount of liquid, also when the droplet is still attached to the syringe needle ($200\mu m$). This problem may be an advantage for deposition of droplets with volume less than $0.3\mu l$. Pressure produced by the motorized syringe pump is not high enough to overcome the Laplace Pressure for drops of small radii. Itś easy to produce larger drops and wait for their reduction by evaporation. For this reason a third image is required of the droplet attached to the needle immediately before the deposition to give a more accurate determination of the droplet volume. This kind of image is required also because the amount of liquid supplied by the syringe pump may be affected by the presence of trapped air bubbles. For a precise determination of the drop volume the profile of the image is fitted to an elliptic shape which gives $V \cong \frac{\pi D_V D_H^z}{6}$, where D_H is the horizontal diameter and D_V is the vertical diameter. A fourth image with a top view of the droplet give a picture of the contact line shape when both contact angles are less than $90°$. In other cases this detail can not the experimentally investigated.

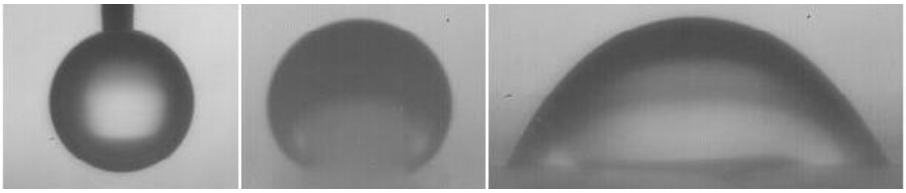

Figure 4.3: Left) Water droplet attached to the syringe needle before deposition; center) orthogonal view of the drop deposited onto a PDMS post; c) parallel view of the same drop measured parallel to the PDMS post.

A typical measurement procedure consists in the following steps: a) the substrate is correctly aligned in the orthogonal direction under the needle (pillar shadows are used as reference); b) liquid is injected and the first image is acquired; c) the droplet is gently deposed on the substrate and the second image is acquired; d) the sample is quickly rotated of $90°$ and aligned; e) the camera focus is adjusted and the third image is acquired; f) the liquid is removed with nitrogen

flow and the sample again placed under the needle. Time required from the first to the third image acquisition varies from 20 to 30 seconds.

4.5 Evaporation effects.

We have quantified the effects of evaporation for our experimenal conditions. We tested two different flat surfaces made of PDMS ($\theta \sim 117°$) and glass ($\theta \sim 55°$). We deposited the typical size droplet of volume $0.5\mu l$ and took three images at second per 2 minutes and extracted contact angles. Results are reported in figure 4.4. Points are scattered with a standard deviation of $0.2°$, according with calculations reported in A.6. In both cases the contact angle decreases by several degrees. However after 20 seconds the decrease is quantified in about 2 degrees for both substrates. Becouse of this we corrected the third measurement (along the parallel direction) by adding 2 degrees.

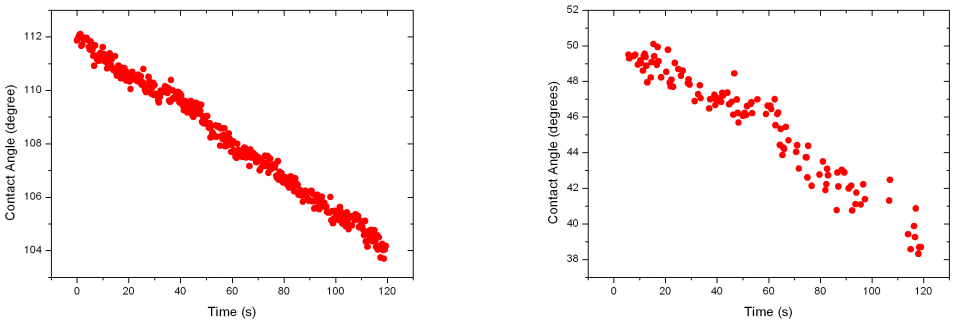

Figure 4.4: Left) Evolution of contact angle in time on a PDMS flat surface; right) the same on a flat glass surface. Initial volume is $0.5\mu l$.

4.6 Advacing Contact Angle

Advancing and receding contact angles are measured with the captive - drop goniometric (CDG) technique. Details of software analysis are reported in section A.7. A droplet is initially deposited on the substrate and the camera focused on its profile. Then a sequence of images is recorded. Frequency acquisition and injection rate may be optimized. In picture 4.5 is reported as example a superposition of profiles obtained by sequence analysis. In this case the acquisition frequency is 50 Hz and injection rate $1\mu l/s$. Measurements are performed on titania cluster assembled rough surfaces. A full characterization of these samples is reported in section 7. Here we

only report preliminary results of this kind of measurements, which are a recent upgrade of our system.

We observed that the elongation is not the same in the two directions. Different factors may affect this behavior and explain the asymmetry: a) our needle is $200\mu m$ wide: enough to affect the drop shape; b) pining effects on the contact line are not the same; c) Internal fluid dynamics during injection is fast and affects the local internal pressure.

This kind of measurements shall be improved by taking a smaller syringe and needle. In this case we should use two different needles consecutively: with the first larger one the initial amount of liquid is injected overcoming the Laplace pressure for small radii. After that the needle and the syringe body may be changed with narrower ones. This second needle should be inserted into the droplet just injected and the image acquisition with a slow rate flux can be performed. This procedure can minimize distorsions due to the needle size and fluid motions inside the droplet.

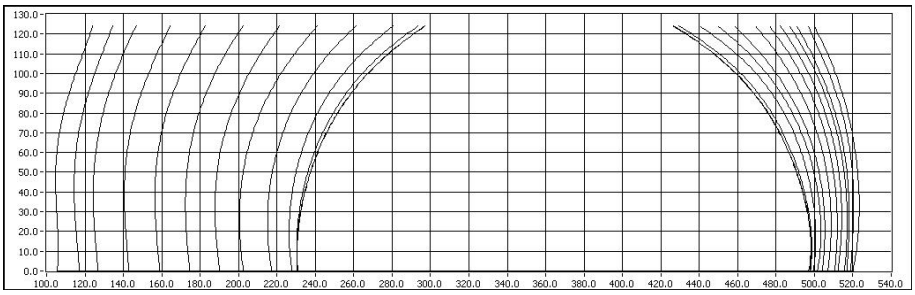

Figure 4.5: Example of advancing sequence. Measurements performed on titania cluster assembled surface. See section 7 for details.

A preliminary characterization of advancing angle on different substrates has been performed. In picture 4.6 measurements of the mean contact angle and base elongation as a function of time are reported. In this case fot $t < 0.4$ s the droplet is static. At $t \sim 0.4$ the injection starts and we register a fast increase of the contact angle from 107° to 116° while the base remains pinned and does not changes. At $t \sim 0.5$ the base starts increasing, and contemporarily we register the maximum contact angle. Successively the base advances. In this case no jumps are recorded. The volume increases linearly with time, so he base increases approximately as $B \sim t^{1/3}$. As the base increases the advancing contact angle shows a slow decreases. This may be interpreted in this way: The initial pinning is static, and allows an increase of the contact angle until a maximum value θ_{adv}.

In picture 4.7 we report a superposition od advancing measurements on four different samples where we see three different wetting behaviors: Sample D is characterized by the lower roughness and has been previously described. Samples B and C are found to have the same surface roughness,

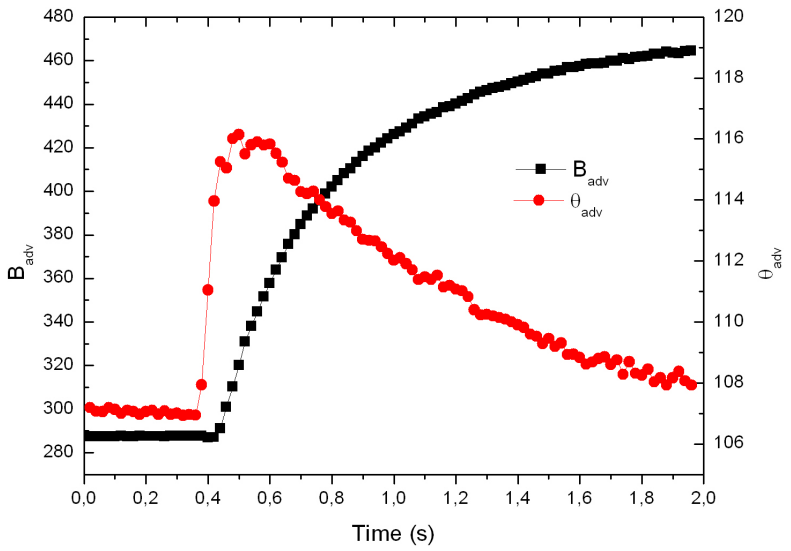

Figure 4.6: Superposition of Base elongation and Contact angle measurements from the image sequence.

while sample A presents the largest roughness. The complete characterization of these sample is reported in section 7. Static contact angles increases with roughness. Samples B and C and D show a slower increment of the contact angle, but while in samples B and C it comes back quickly to the static value, in sample D it remains near its maximum value after it has been reached. Similar measurements have been performed to measure the receding angle, and all sample show a marcate pinning on the substrate. The contact angle gets down until the liquid detach from the needle. This behavior proofs the collapsed wenzel state of the droplets on these substrates.

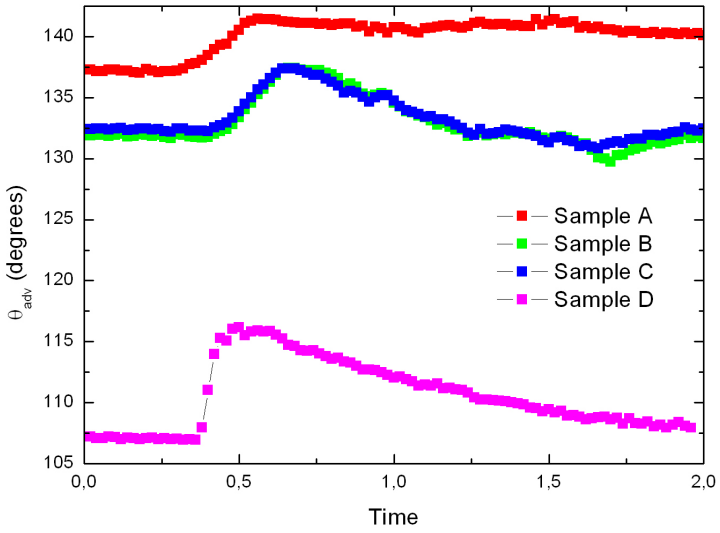

Figure 4.7: Three different behaviors from samples described in section 7.

Chapter 5

Numerical method: a Lattice Boltzmann Model

In this chapter, we shall describe the numerical approach that we have used to support the experimental measurements. It belongs to a class of hydrodynamic models, called diffuse interface models [64; 65; 66; 67], where the interface has a finite width. Far away from the contact line, these models solve the hydrodynamic equations of motion of the fluid, while close to the contact line, the finite interface width allows an effective slip length to be generated by either an evaporation-condensation mechanism [65; 66] or a diffusive transport across the interface [64; 67]. The effective slip length is needed to remove the stress singularity at the contact line (see e.g. [71; 72; 73]).

The hydrodynamic equations of motion of diffuse interface models can be solved in many different ways, but in this thesis, this is done using a particular mesoscopic modeling technique called the lattice Boltzmann method. It has proved to be a powerful tool to study many complex fluids problems [74; 83], and wetting phenomena on chemically and topologically patterned surfaces [84; 85].

The algorithm presented here is the liquid - gas model based on the so-called free energy lattice Boltzmann method, first introduced by Swift et al. [80], and later modified by Briant et al. [66; 67] to include the surface wetting term. We shall follow the models suggested by Briant et al. closely here.

5.1 Thermodynamics of the Fluid

The equilibrium properties of a one-component, the two-phase fluid of local density $n(\vec{r})$ and in contact with a solid surface, can be described by a Landau free energy functional [66]

$$\int_V \left(\Psi_b(T,n) + \frac{k}{2}(\partial_\alpha n)^2 \right) dV \tag{5.1}$$

The first term $\Psi_b(T,n)$ describes the Van der Waals bulk free energy of the system at temperature T,

$$\Psi_b(n) = nT \ln\left(\frac{n}{1-nb}\right) - an^2 \tag{5.2}$$

which we choose for convenience to have the double well form [66]

$$\Psi_b(n) = p_c(\nu_n + 1)^2 \left(\nu_n^2 - 2\nu_n + 3 - 2\beta\tau_w\right) \tag{5.3}$$

where $\nu_n = (n - n_c)/n_c$ and $\tau_w = (T_c - T)/T_c$. The parameters n_c, T, T_c and p_c are the critical density, local temperature, critical temperature and critical pressure respectively. In our simulations we used $k = 0.018$, $n_c = 7/2$, $p_c = 1/8$ and $\tau_w = 0.3$. β is a constant typically chosen to be 0.1. For $T < T_c$ the minimization of $\Psi_b(n)$ leads to two coexisting bulk phases of density $n_c\left(1 \pm \sqrt{\tau_w/10}\right)$ [66]. In addition to uniform phases $n = n_g$ or n_l, the free energy also allows an interface of the form $n = n_c\{1 + \sqrt{\beta\tau}\tanh[x/\sqrt{2}\xi]\}$ between two phases with width ξ and surface tension σ. It can be shown that [66]

$$\xi = \sqrt{(kn_c^2) \,/\, (2p_c\tau_w/5)} \tag{5.4}$$

$$\sigma_{lg} = \left(4n_c(\tau_w/10)^{3/2}\sqrt{2kp_c}\right)/3 \tag{5.5}$$

Thus the equilibrium properties of the model are determined by the choice of the free energy.

The time evolution of the drop is described by the continuity and Navier-Stokes equations

$$\partial_t n + \partial_\alpha(nu_\alpha) = 0 \tag{5.6}$$

$$\partial_t(nu_\alpha) + \partial_\beta(nu_\alpha nu_\beta) = -\partial_\beta P_{\alpha\beta} + \nu\partial_\beta[n(\partial_\beta u_\alpha + \partial_\alpha u_\beta + \delta_{\alpha\beta}\partial_\gamma u_\gamma)] \tag{5.7}$$

where $\vec{u}$ and ν are the local velocity and the kinematic viscosity respectively. We impose the no-slip boundary conditions $\vec{u} = 0$ on the surfaces.

The thermodynamic properties enter via the the pressure tensor $P_{\alpha\beta}$, which can be calculated from the free energy. Since the free energy function and the mass constraint are independent of position, it follows from Noether's theorem that in equilibrium the conservation of momentum takes the form

$$\partial_\beta P_{\alpha\beta} = 0 \tag{5.8}$$

for a pressure tensor $P_{\alpha\beta}$ given by

$$P_{\alpha\beta} = \frac{\partial\mathcal{F}}{\partial(\partial_\alpha n)}(\partial_\beta n) - \mathcal{F}\delta_{\alpha\beta} \tag{5.9}$$

where $\mathcal{F} = \Psi - \mu_b n + k(\partial_\gamma n)^2/2$ [68]. and $p_0 = n\partial_n \Psi - \Psi$ is the equation of state of the fluid. For our choice of Ψ this gives

$$P_{\alpha\beta} = \left(p_b - kn\partial_{\gamma\gamma} n - \frac{k}{2}(\partial_\gamma n)^2 \right) + k(\partial_\alpha n)(\partial_\beta n) \tag{5.10}$$

where the bulk pressure is

$$p_b = p_c(\nu_n + 1)^2 \left(\nu_n^2 - 2\nu_n + 3 - 2\beta\tau_w \right) \tag{5.11}$$

and the bulk chemical potential is

$$\mu_b = \partial_n \Psi_n|_{n=n_b} = \frac{4p_c}{n_c}(1 - \beta\tau) \tag{5.12}$$

5.2 The Lattice Boltzmann Implementation

The Lattice Boltzmann algorithm is defined in terms of the dynamics of a set of real numbers that move on a lattice in a discrete time. A set of distribution functions $\{f_i(\mathbf{r}, t)\}$ is defined on each lattice site $\mathbf{r}$. Each of these distribution functions can be interpreted as the density of the fluid at time t that will move in the direction i. The directions $\{i\}$ are discrete, and for a 3D system, in order to have an isotropic definition of the pressure tensor, one needs to take at least 15 velocity vectors $\{\mathbf{e}_i\}$:

$$\begin{pmatrix} e_{x\,0-6} \\ e_{y\,0-6} \\ e_{z\,0-6} \end{pmatrix} = \begin{bmatrix} 0 & c & -c & 0 & 0 & 0 & 0 \\ 0 & 0 & 0 & c & -c & 0 & 0 \\ 0 & 0 & 0 & 0 & 0 & c & -c \end{bmatrix},$$

$$\begin{pmatrix} e_{x\,7-14} \\ e_{y\,7-14} \\ e_{z\,7-14} \end{pmatrix} = \begin{bmatrix} c & -c & -c & c & -c & c & c & -c \\ c & -c & c & -c & -c & c & -c & c \\ c & -c & c & -c & c & -c & c & -c \end{bmatrix}.$$

c is the lattice speed defined by $c = \Delta\mathbf{r}/\Delta t$, where $\Delta\mathbf{r}$ and Δt represent the discretization in space and time respectively. The directions of the velocity vectors are shown in Fig. 5.1. The distributions are related to the physical variables by

$$\sum_i f_i = n, \;\; \sum_i f_i e_{i\alpha} = n u_\alpha \tag{5.13}$$

where $\mathbf{u} = \mathbf{v} - \mathbf{a}\Delta t/2$, and $\mathbf{a}$ generally is the acceleration associated with an applied body force. This distinction is required so that the lattice Boltzmann equation recover the continuity 5.6 and Navier-Stokes 5.7 equations in the continuum limit.

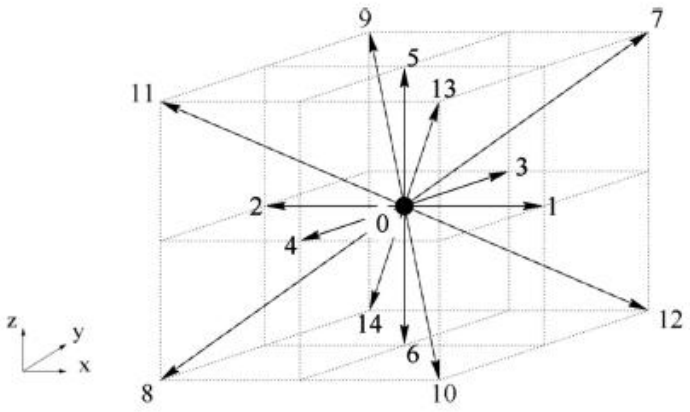

Figure 5.1: The directions of the lattice velocity vectors in the 15-velocity lattice Boltzmann model.

Taking a single-time relaxation approximation, the evolution equation for a given distribution function f_i takes the form

$$f_i(\mathbf{r} + \mathbf{e_i}\Delta t, t + \Delta t) = f_i(\mathbf{r}, t) + \frac{1}{\tau}[f_i^{\mathrm{eq}} - f_i] + nw_\sigma v_{i\alpha} g_\alpha, \tag{5.14}$$

where f_i^{eq} is the local equilibrium distribution function along the velocity direction i, the choice of which determines the physics inherent in the simulation. We have $w_\sigma = w_1 = 1/3$ if $|v| = c$ and $w_\sigma = w_2 = 1/24$ if $|v| = c\sqrt{3}$, and Δt is the time step, and τ is the relaxation time due to collisions. The last term in eq. 5.14 is the forcing term, which is related to the acceleration through $a_\alpha = c^2 g_\alpha / \Delta t$. Because $\Delta \mathbf{r}$ and Δt are tipically taken to be 1 in simulation units, the notations a_α and g_α are interchangeable here.

The conservation laws that determine the physics are introduced by choosing f_i^{eq}, such that the conserved moments of f_i are equal to the corresponding moments of f_i^{eq}. For example, if $p_\alpha = \sum_i f_i^{\mathrm{eq}} e_{i\alpha}$ taking the first moment of Eq. 5.14 indicates that p_α is a locally conserved quantity in the simulation. To obtain the continuum differential equations mimicked by eq. 5.14 we Taylor expad the left hand side to give

$$-\frac{1}{\tau}[f_i - f_i^{\mathrm{eq}}] = \sum_{k=1}^{\infty} \frac{1}{k!} \Delta t^k (\partial_t + e_{i\alpha}\partial_\alpha)^k f_i \tag{5.15}$$

for which eq. 5.14 is the exact discretization. ∂_t and ∂_α denote differentiation with respect to t and x_α, respectively. Retaining terms to $O((\Delta t)^2)$, Eq. 5.15 becomes

$$-\frac{f_i - f_i^{\mathrm{eq}}}{\tau \Delta t} = (\partial_t + e_{i\alpha}\partial_\alpha) f_i^{\mathrm{eq}} - (\tau - 1/2)\Delta t(\partial_t^2 + 2e_{i\alpha}\partial_t\partial_\alpha + e_{i\alpha}e_{i\beta}\partial_\alpha\partial_\beta) f_i^{\mathrm{eq}} + O((\Delta t)^2 \tag{5.16}$$

Taking moments of eq. 5.16 with respect to $\vec{e_i}$ gives equation relating the time evolution of moments of f_i to the derivatives of the higher moments of the equilibrium distribution function. The kinematic viscosity ν is tuned by the relaxation time τ via [66]

$$\nu = \frac{\Delta \mathbf{r}^2}{\Delta t} \frac{1}{3} \left(\tau - \frac{1}{2} \right) \tag{5.17}$$

It can be shown [80] that eq. 5.14 reproduces the Navier - Stokes equations of non - ideal gas if the local equilibrium functions are chosen as

$$f_i^{\mathrm{eq}} = A_\sigma + B_\sigma u_\alpha e_{i\alpha} + C_\sigma \mathbf{u}^2 + D_\sigma u_\alpha u_\beta e_{i\alpha} e_{i\beta} + G_{\sigma\alpha\beta} e_{i\alpha} e_{i\beta} \tag{5.18}$$

when $i > 0$ and

$$f_0^{\mathrm{eq}} = n - \sum_{i=1}^{z} f_i^{\mathrm{eq}} \tag{5.19}$$

for the rest particle ($i = 0$). Einstein notation is understood for the Cartesian labels α and β (i.e. $e_{i\alpha} u_\alpha = \sum_\alpha e_{i\alpha} u_\alpha$) and σ labels velocities of different magnitude. The coefficients A_σ, B_σ, C_σ, D_σ and G_σ are chosen so as to satisfy the relations

$$\begin{aligned} &\sum_i f_i^{\mathrm{eq}} = n, \qquad \sum_i f_i^{\mathrm{eq}} e_{i\alpha} = n u_\alpha, \\ &\sum_i f_i^{\mathrm{eq}} e_{i\alpha} e_{i\beta} = P_{\alpha\beta} + n u_\alpha n u_\beta + \nu [u_\alpha \partial_\beta n + u_\beta \partial_\alpha n + \delta_{\alpha\beta} u_\gamma \partial_\gamma n], \\ &\sum_i f_i^{\mathrm{eq}} e_{i\alpha} e_{i\beta} e_{i\gamma} = \frac{n c^2}{3} [u_\alpha \delta_{\beta\gamma} + u_\beta \delta\gamma\alpha + u_\gamma \delta_{\alpha\beta}], \end{aligned} \tag{5.20}$$

where $P_{\alpha\beta}$ is the pressure tensor and the last term of the third expression in Eq. 5.20 is included to ensure galileian invariance.

Considering a 15 velocity vectors lattice model and a square - gradient approximation to the

inerface free energy $k(\partial_\alpha n)^2/2$ [80], a possible choice of the coefficients is [93]

$$\begin{aligned} A_\sigma &= \frac{w_\sigma}{c^2}\left(p_b - \frac{k}{2}(\partial_\alpha n)^2 - kn\partial_{\alpha\alpha}n + \nu u_\alpha \partial_\alpha n\right), \\ B_\sigma &= \frac{w_\sigma n}{c^2}, \\ C_\sigma &= -\frac{w_\sigma n}{2c^2}, \\ D_\sigma &= \frac{3w_\sigma n}{2c^4}, \\ G_{1\gamma\gamma} &= \frac{1}{2c^4}\left(k(\partial_\gamma n)^2 + 2\nu u_\gamma \partial_\gamma n\right), \\ G_{2\gamma\gamma} &= 0 \\ G_{3\gamma\gamma} &= \frac{1}{16c^4}\left(k(\partial_\gamma n)(\partial_\delta n) + \nu(u_\gamma \partial_\delta n + u_\delta \partial_\gamma n)\right), \end{aligned} \tag{5.21}$$

We note that the choice for implementing the liquid gas model is not unique. There are equivalent models in the literature, for example [88; 90], that have been used to model liquid gas systems with considerable success. There has also been extensive work in the literature that aims to improve both the stability [91] and accuracy of the model [87; 92; 91].

5.3 Wetting Boundary Conditions

In his paper of critical wetting, Cahn showed how, by including short ranged surface - fluid interactions, the surface tensions σ_{sg} and σ_{sl} may be calculated [86] within mean field framework. Cahn assumed that the fluid - solid interactions are short ranged such that they contribute a surface integral to the total free energy of the system. The total free energy becomes

$$\int_V \left(\Psi_b(T,n) + \frac{k}{2}(\partial_\alpha n)^2\right) dV + \int_S \Psi_S(n_S) dS - \mu_b \int_V n dV. \tag{5.22}$$

Here $\Psi_S(n_s)$ is a surface density energy function which depends only on the density at the surface n_s, and S is the surface bounding V. Minimizing the free energy gives an equilibrium boundary condition on the surface S

$$k\partial_\perp n = \frac{d\Psi_S}{dn_s} \tag{5.23}$$

Following Briant [66] Ψ_S is expanded as power series: in this thesis, as usual, we consider only a linear term, so we write $\Psi_S = -\phi_1 n_s$ where ϕ_1 is a constant which we call wetting potential. thus eq. 5.23 becomes $k\partial_\perp n = -\phi_1$.

The results for the surface tensions are

$$\sigma_{sg} = -\phi_1 n_c + \frac{\sigma}{2} - \frac{\sigma}{2}(1-\Omega)^{3/2} \tag{5.24}$$

$$\sigma_{sl} = -\phi_1 n_c + \frac{\sigma}{2} - \frac{\sigma}{2}(1+\Omega)^{3/2} \tag{5.25}$$

where $\Omega = \phi/\beta\tau_w\sqrt{2kp_c}$ is the dimensionless wetting potential. The wetting angle is found by substituting Eqs. 5.24 and 5.25 into Youngś law (eq. 2.1). The result is

$$\cos\theta_w = \frac{(1+\Omega)^{3/2} - (1-\Omega)^{3/2}}{2} \tag{5.26}$$

Equation 5.26 may be inverted in the range $0 < \theta_w < \pi$ and gives

$$\Omega = 2\text{sign}\left(\frac{\pi}{2} - \theta_w\right)\sqrt{\cos\left(\frac{\alpha}{3}\right)\left[1 - \cos\left(\frac{\alpha}{3}\right)\right]} \tag{5.27}$$

where $\alpha = \arccos(\sin^2\theta)$ and the function sign returns the sign of its argument. Therefore, by chosing a desired angle θ_w we can calculate the wetting potential Ω. In the case of single posts θ_w may be related to the actual contact angle θ_a.

The problem of incorporating wetting into a lattice Boltzmann scheme in essence finding a way to include the boundary condition (5.23). This algorithm can be thought of a three basic steps as follows: first the desired wetting preperties of the surface are chosen (i.e. the wetting angle θ_w). Next the required value of $\partial_\perp n$ is calculated using Eqs. 5.27 and 5.23. Lastly this value of $\partial_\perp n$ is used rather than a numerical derivative when calculating $f^e q$ at the wall. In ref. [69] is shown that the correct equilibrium angle on a flat surface is obtained in the range $30^\circ < \theta_w < 150^\circ$ to within 2°.

Equation 5.26 is used to constrain the density derivative for sites on a flat part of the substrate. However, no such exact results are available for sites at edges or corners. The implementation used in this thesis follows the prescriptions of Dupuis and Yeomans [70] which work on the principle that the wetting angle at such sites should be constrained as little as possible so that, in the limit of an increasingly fine mesh, it is determined by the contact angle of the neighboring flat surfaces. For edges (labels 9-12 in Figure 5.2) and corners (labels 1-4) at the top of the post, each site has 6 neighbors on the computational mesh. Therefore, these sites can be treated as bulk sites. At bottom edges where the post abuts the surface (labels 13- 16 in Figure 5.2), density derivatives in the two directions normal to the surface (e.g., x and z for sites labeled 13) are calculated using

$$\partial_z n = \partial_{x/y} n = -\frac{1}{\sqrt{2}}\frac{\phi_1}{k} \tag{5.28}$$

where the middle term constrains the density derivative in the appropriate direction x or y. At bottom corners where the post joins the surface (labels 5-8 in Figure 5.2), density derivatives in both the x and y directions are known. Therefore, these sites are treated as planar sites.

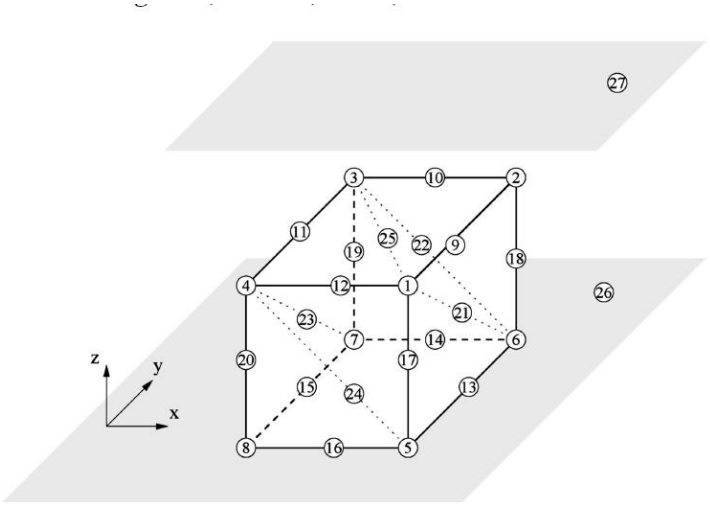

Figure 5.2: Sketch of a post on a substrate from [70]. Encircled numbers label sites in different topological positions. Labels 26 and 27 denote sites on the bottom ($z = z_{min}$) and the top ($z = z_{max}$) of the domain, respectively.

5.4 Velocity Boundary Conditions

Because the collision operator (the right hand side of eq. 5.14) is applied at the boundary, the usual bounce-back condition is not appropriate as it would not ensure mass conservation. Here we impose the condition proposed by Dupuis and Yeomans [93; 70], by determining the missing fields fullfilling the no-slip conditions given by Eq. 5.13 with $\mathbf{u} = 0$. This does not uniquely determine the f_i's. For most of the cases (i.e., 1-20), arbitrary choices guided by symmetry are used to close the system. This is no longer possible for sites 21-27 where four asymmetrical choices are available. Selecting one of those solutions or using a simple algorithm which chooses one of them at random each time step leads to very comparable and symmetrical results. Hence, we argue that an asymmetrical choice can be used. Possible conditions, proposed by Dupuis and Yeomans [70], which are used in the results reported here, are listed in Appendix B. The conservation of mass is ensured by setting a suitable rest field, f_0, equal to the difference between the density of the missing fields and the one of the fields entering the solid after collision. In a hydrodynamic description of wetting contact, line slip must be introduced insome way. As with other phase-field models, slip appears naturally within the lattice Boltzmann framework. The mechanism responsible for the slip is evaporation and condensation of the fluid because of a nonequilibrium curvature of the contact line [66; 64].

5.5 Discussion

In this chapter we have briefly exposed the basic concepts and some details of the implementation of the Lattice Boltzman simulation performed in this thesis. In the liquid gas model here adopted, the two fluid phases are of the same substance and, as a result, the liquid (gas) phase can evaporate (condense) to the gas (liquid) phase. The evaporation-condensation mechanism is important close to the contact line, where it provides a way to relax the no - slip boundary condition and hence allow the contact line to move. In this way the final volume of the droplet is often diferent from the initial one. Thanks to the simplicity of the simulated system, we can easily rescale the density profiles to compare results with the same volume. One of the difficulties of this model is that the liquid gas density ratio is often limited to unphysically small values by the stability of the algorithm and this may lead to an unphysical dynamical behaviour. For our purposes the dynamic is considered only a way to find the minimum energy configuration of a droplet, given the starting configuration and the boundary conditions. Another difficult arises from the unphysically width of the liquid - air interface, which affect the determination of the local contact angles near the corners of the posts. On the other hand, as we shall see in chapter 6, the anisotropy of the droplets involves consistent curvature deviations along the axial profile in order to respect the Laplace law. The impossibility to extract univocally a local contact angle represents a strong limitation of the method, particularly relevant with hydrophobic surfaces. A possible improvement of the method should consist in taking into account non linear terms in the expansion of the interface potential $\Psi_s(n_s)$.

Chapter 6

A detailed study of Anisotropy

In this chapter we discuss the results of systematic experiments, and numerical simulations. As a complement of this study, we will also present a simple geometrical model of the shape of droplets deposited on single posts of different widths and various surface energies. The choice of the single post requires a better analysis of the anisotropy of water droplets, resulting from the pinning of the droplet contact line, without the mentioned complications due to the presence of multiple grooves. Furthermore, if no structure is present under the droplet, the system can be considered size-independent in the limit of small droplets, and droplets with large aspect ratios can be simply obtained by reducing the post width.

For simplicity we organize the discussion in three separate sections: In the first we report a full experimental characterization, involving both a detailed description of the different samples and a global picture of anisotropy. In the second we report numerical simulations performed with the Lattice Boltzmann method while in the third a simple geometrical model is described and compared with previous results. We also performed some simulations with the Surface Evolver software, whose results are reported when needed inside these sections.

6.1 Experimental characterization

6.1.1 Samples

Using a variety of techniques described in section 3, we have fabricated numerous surfaces patterned with linear pillars having a rectangular cross section. Both hydrophobic and hydrophilic materials were investigated. In particular, we employed rapid prototyping techniques based on a commercial liquid thiolene optical adhesive, NOA61 from Norland products [101], a material that is moderately hydrophobic (characteristic equilibrium contact angle $\theta_a = 65^\circ$). With the procedure described in section 3.6 we prepared parallel pillars with a width w ranging from 500

to 900 microns and an height h of 100 microns. We have also used PMMA surfaces ($\theta_a = 75\,\mathrm{deg}$) patterned with a conventional 3 axis milling machine. The pillars had typical sizes W ranging from 500 to 900 μm and H=550 μm.

For a more stringent comparison with numerical simulations, we have sculpted rectangular posts on a stainless steel surface made by micro electrical discharge machining (micro EDM), operated in milling mode. Micro electrical discharge machining is a thermal process for contactless material removal of electrically conductive materials. The machined features consisted of a series of rectangular protrusions with length of 15 mm, height of 200 μm and widths of 200, 400, 600 and 800 μm obtained from a stainless steel substrate, using electrodes in tungsten carbides with a diameter of 300 μm. In picture 3.14 is reported a top view of the stainless steel sample. On its surface there is a residual anisotropic roughness of about $1\mu m$ along. After a lapping treatment (reducing the roughness to a few nanometers and homogeneous) we have then fabricated positive copies in polydimethilsiloxane (PDMS) by a standard double replica molding process.

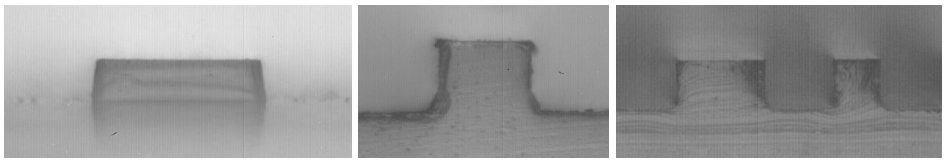

Figure 6.1: Post profiles of three materials investigated: left)NOA;center)PMMA; d)PDMS. .

An important detail is the sharpness of the post corners. If the corner is ideal, in principle the droplet should follow the Gibbs criterion and pin to the edge. Now we focus on the fact that the sharpness of our samples is not the same. In figure 6.1 examples of the post profiles for NOA, PMMA and PDMS samples are reported. The stainless steel profile is similar to the PDMS one, which is obtained by the double replica molding. The sharpest profiles are shown by PDMS and STEEL samples, while NOA and PMMA one present some irregularities. Specifically the NOA corner is a little rounded, and the lateral walls are not exactly vertical but a little tilted, while PMMA corners show micrometric asperities residual from the processing job, which we expect to affect the contact line with random effects.

Every sample before a measurement is washed with hot water and ethanol and dried with a nitrogen flow. We point out that samples in PDMS, NOA and PMMA show stable and constant values dependent on the cleaning procedure, while the stainless steel once cleaned with ethanol show angles lower than $40°$, but only a few depositions are sufficient to make it increase until $50°$, and in few more time increases until $90°$. For this reason, before any set of measurements the stainless steel sample is first completely cleaned with ethanol and acetone and then dipped into de-ionized water. This procedure ensures a stable value of θ_a of about $50°$ for the duration of

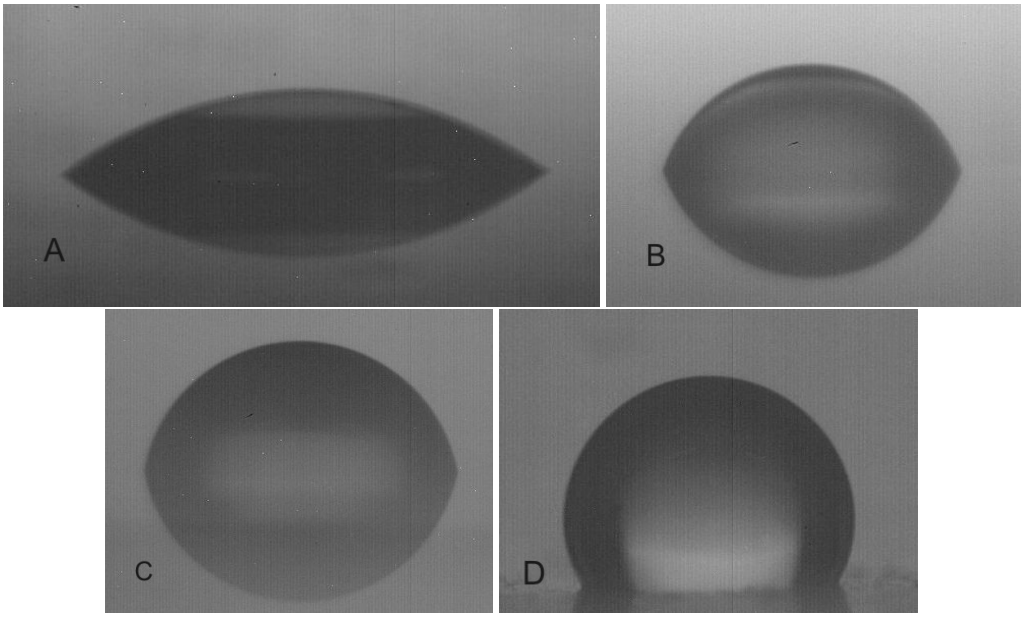

Figure 6.2: a) flat stainless steel; b) NOA; c) PMMA; d)flat PDMS.

Sample	Contact Angle
a) STEEL	49.5°
b) NOA	65°
c) PMMA	73°
d) PDMS	118°

Table 6.1: Apparent contact angles of water on the four different substrates with flat homogeneous surfaces.

acquisition.

6.1.2 Profile analysis: curvature deviations.

Specific details of the image acquisition procedure for anisotropic droplets are reported in section 4.4. The quality of images vary from sample to sample, and depends both on geometrical details and wetting behavior. In figure 6.3 we report as example some images of the orthogonal profiles taken for the four materials investigated: the mean quality of images gets better as the substrate hydrophobicity increases. This is due to the fact that water droplets deposited on hydrophilic surfaces are strongly elongated along the post in the parallel direction, while on hydrophobic surfaces have a more compact shape. As a consequence, in the first case, it is more difficult in the orthogonal view to focus on the droplet contour and the resulting image is somewhat blurred. Fur-

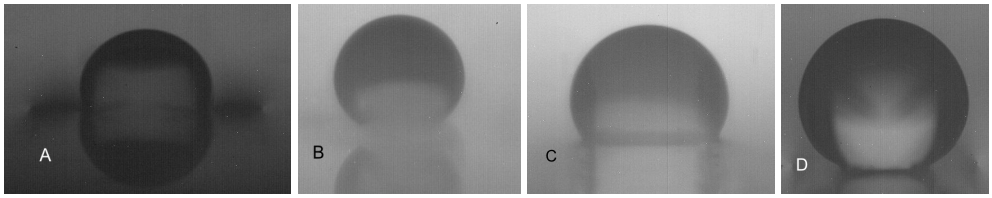

Figure 6.3: Examples of orthogonal profiles for the four materials investigated: the quality gets better as the substrate hydrophobicity increases: a)STEEL; b)NOA; c)PMMA; d)PDMS.

ther, in the case of the stainless steel (and PDMS) the height of the top of the post is the same as that of the other parts of the sample, while in the other materials the post is a protrusion on the surface. This creates two dark regions on the sides of the post which together with the blurring effect make also more difficult the contact angle estimation.

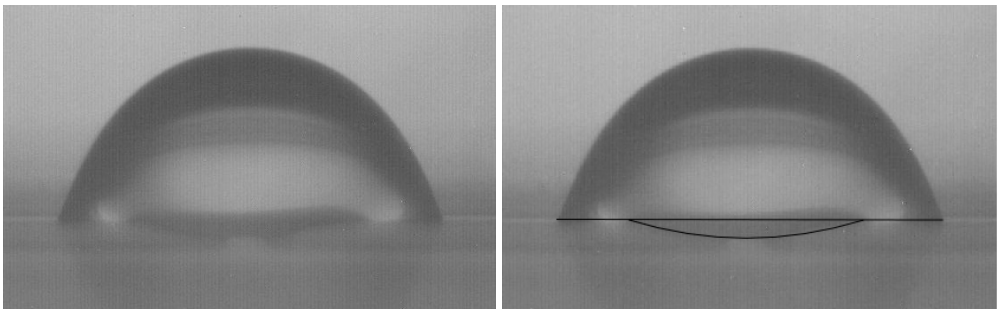

Figure 6.4: Spilling effects on noa samples: parallel views.

We notice that orthogonal droplet profiles not always are exactly pinned to the corner. Often NOA samples show a sort of spilling effect, and the droplet partially falls on the walls, as shown in figure 6.4. Unfortunately in the NOA samples the rounded corners and the tilted walls facilitate the spilling. This affects the comparison with other samples with sharper corners.

We developed several different fitting procedures to obtain contact angle values from an image. Usually the shape is assumed to have a circular profile. This is true if two conditions are satisfied: a) the droplet volume is sufficiently small to neglect gravity effects; b) the three phase contact line has a circular shape. Generally profiles are fitted with elliptic shapes. This procedure guarantees a better fit if condition of point a) is not fuly verified and possible deviations near the contact line are neglected [85]. In our case point a) may be considered at first order satisfied, while the default of point b) is the matter of our investigations.

As figure 6.5 shows, the local contact angle is generally different from the apparent contact angle determined by fitting the whole droplet profile with an ellipse. The difference $\delta\theta = \theta_{local} -$

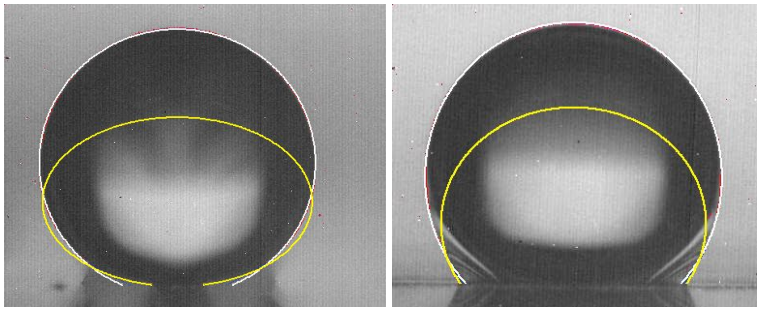

Figure 6.5: left) orthogonal view of the droplet deposited onto a PDMS post: white(yellow) line is a global (local) elliptic fit to the droplet profile; right) parallel view of the same droplet measured parallel to the PDMS post.

θ_{global} cannot be ascribed to gravitational effects because the maximum volume of the investigated droplets was less than $1\mu l$, corresponding to a typical radius of about $0.6mm$, smaller than the capillary length for water ($2mm$). It is rather a consequence of the droplet elongated shape. In fact, we observed the largest discrepancies between the two determinations when analyzing the most anisotropic droplets observed on the narrowest posts. Figure 6.6 shows the $\delta\theta$ calculated analyzing droplet images taken on PDMS posts of different width w both in the orthogonal and in the parallel views. In this data set neither the post width nor the droplet volume are fixed.

The difference $\delta\theta$ is plotted as a function of the ratio V/w^3, which represents the droplet volume V scaled to the post size. At small values of the scaled volume, the two fits are practically indistinguishable. As the volume increases, the droplet starts to assume an elongated shape and the results of the two fitting procedures deviate in an appreciate way. For very large ratios, the two determinations differ by more than 10° that cannot be neglected in a proper analysis of the droplet anisotropy. Interestingly, the deviations have different sign for the front and for the lateral views. This effect is also evident, although less pronounced, for the posts made out in PMMA. Instead, the difference is not appreciable for the NOA and the stainless steel samples. We outline that in the case of steel, the difficulty rises from the blurred definition of the profile, and we cannot say if the contact line is really pinned, or the droplet has a little spilling due to the low contact angle of the surface, despite the high sharpness of the corner. Vice versa in the case of NOA, deviations are smoothed by the presence of spilled liquid on the wall, and we cannot say if this is simply an effect of the of the rounded corners, or if would happen also if they were sharper.

In figure 6.7 we have analyzed the images reported in figure 8 of ref. [99], which show large droplets (volume about five times larger than that of the droplets we studied) forming a composite contact with the patterned surface and found a similar behavior. Differences between the local contact angle and the apparent angle were also mentioned in [85], although in this work only apparent angles were presented. In the final section, we will discuss the physical implications of

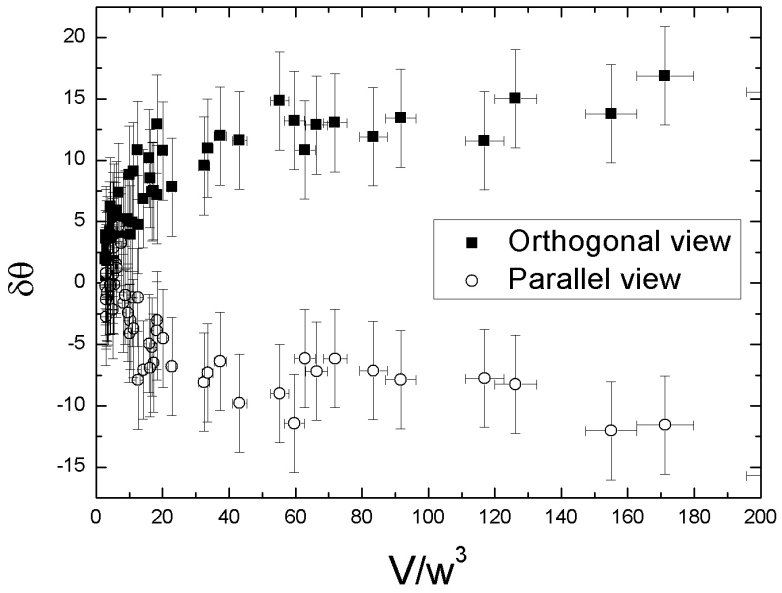

Figure 6.6: Differences in the fitted contact angles of droplets deposited on PDMS posts of different widths as a function of the scaled volume V/w^3.

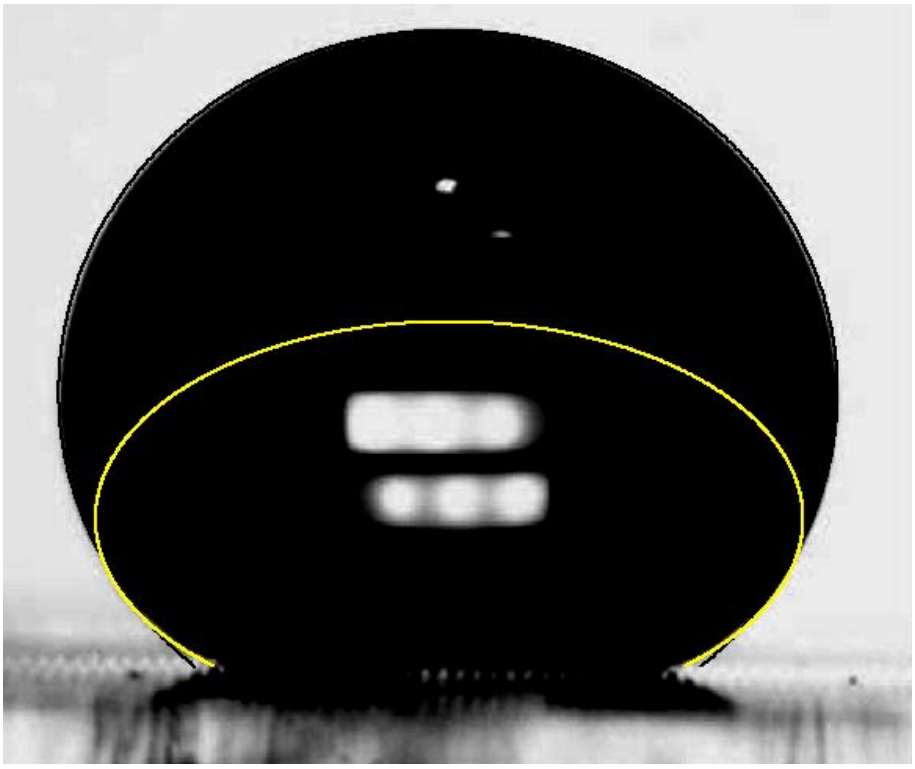

Figure 6.7: Profile reported in [99] with our fits superposed. There the masured contact angle is $\theta_{GON} = 149.5^\circ$ while our procedure gives $\theta_{LOC} = 154^\circ$ and $\theta_{GLOB} = 141.5^\circ$.

such $\delta\theta$ in the droplet elongation process.

6.1.3 Droplets anisotropy

In this section we attempt to provide a consistent picture of the geometry of an elongated droplet deposited on a single rectangular post based on systematic quasi - equilibrium contact angle measurements. After a water droplet is deposited on the top face of the post, it generally assumes an elongated shape parallel to the post direction. To simplify the analysis of the resulting geometry, we focus only on the two principal directions given by the symmetry of the system, e.g. parallel and perpendicular to the post, since the greatest difference in contact angle is expected along these two directions [85]. For each deposited droplet, we measured the equilibrium $\theta_\perp$ and $\theta_\parallel$ and the eccentricity ϵ of the contact line defined as $\epsilon = (B_\parallel - B_\perp)/(B_\parallel + B_\perp)$, where $B_\parallel$ ($B_\perp$) is the maximum base diameter along the parallel (perpendicular) direction.

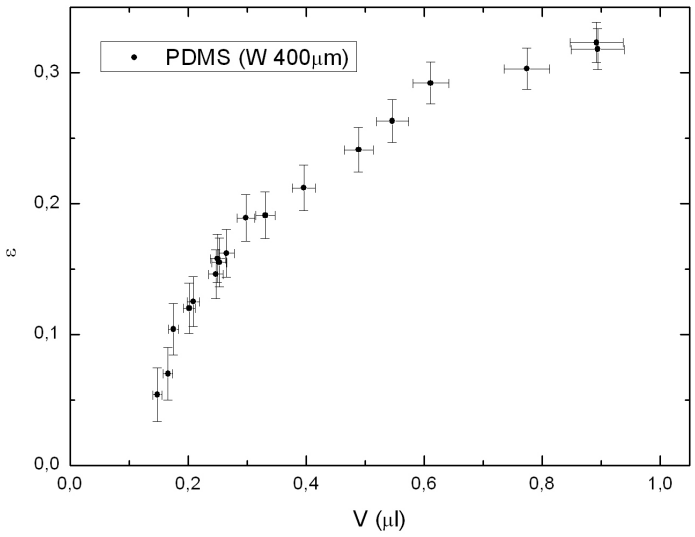

Figure 6.8: Eccentricity ϵ of water droplets deposited on a PDMS post having a width $W = 400\mu m$ as a function of the droplet volume.

Figure 6.8 shows the eccentricity of water droplets deposited on a rough PDMS post having a width $w = 400\mu m$ as a function of the droplet volume. The error bars on ϵ are determined by propagating the errors in the measurement of the base droplet dimension, which correspond to an uncertainty of 5 pixels in the corresponding image views. The smallest volume deposited ($\sim 0.13\mu l$) is large enough to occupy entirely the post width producing a small anisotropy. We

expect that at sufficiently small volumes, the contact line does not reach the post edges and the droplet assumes the shape of a hemispherical cup. As the volume increases, the contact line gets pinned to the edges and the droplet becomes elongated along it. Similar behavior has been found for all the investigated surfaces, although it is more pronounced for hydrophilic surfaces.

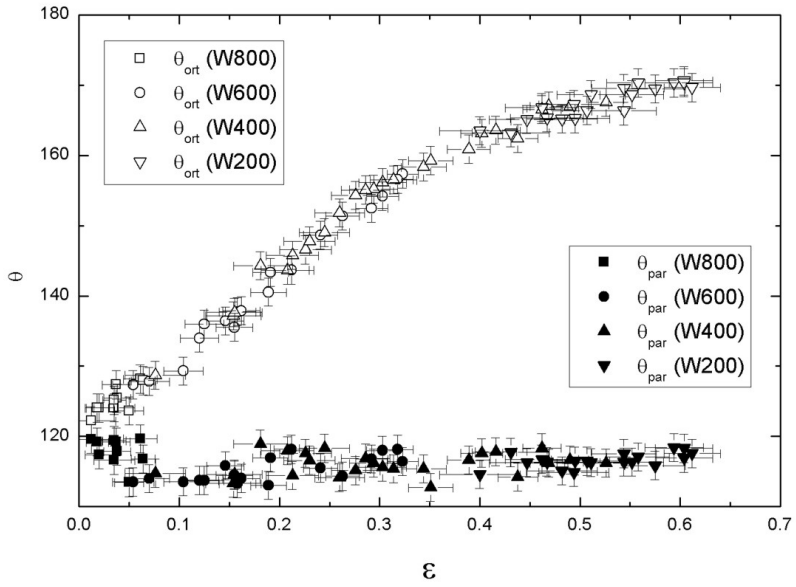

Figure 6.9: Contact angles of water droplets deposited on PDMS posts of different widths.

Figure 6.9 summarizes the contact angle measurements on PDMS posts of different width w and droplet volume V. It shows the orthogonal and parallel contact angles as a function of the base droplet eccentricity. From this graph it is possible to extract some general features common to all the posts investigated:

1. $\theta_\perp$ is always larger than $\theta_\parallel$, in agreement with previous studies on patterned surfaces [99; 100; 85];

2. $\theta_\perp$ is found to increase monotonically with ϵ (and therefore with the droplet volume) and reaches very large values near 180° on the smallest posts;

3. $\theta_\parallel$ is a constant (coincident with the typical value $\theta_e \sim 118^\circ$ measured on a flat PDMS), independent on the volume droplet and on the post width.

Data dispersion is likely due to the presence of surface defects on the post which act as pinning centers for the contact line moving along the parallel direction during the deposition phase.

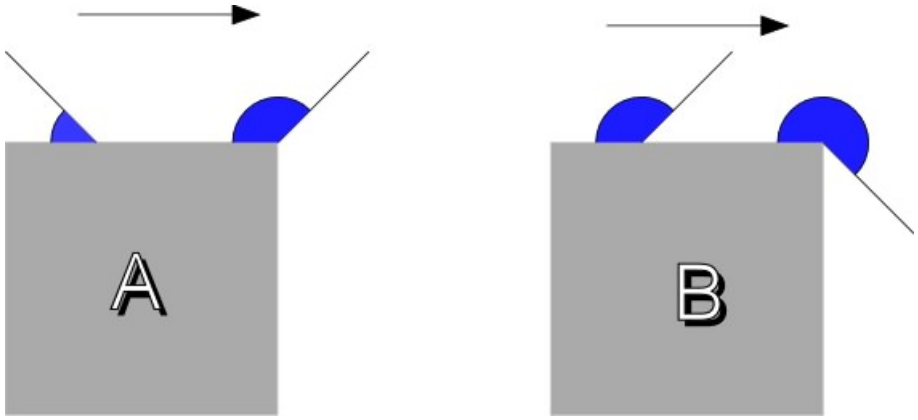

Figure 6.10: Schematization of the Gibbs criterion in case of hydrophilic (a) and hydrophobic (b) substrates.

This data suggests a very pronounced pinning effect exerted by the post edges and a practically free expansion along the post direction. After deposition, the droplet spreads uniformly in all directions till the contact line reaches the outer edges of the post where it gets pinned. In fact, for the contact line to move orthogonally to the post, it has to wet its vertical walls which, according to the Gibbs' criterion [17; 85], occurs when the advancing contact angle in the perpendicular direction $\theta_\perp$ satisfies the relation $\theta_\perp = \theta_e + 90°$. More generally, for a two dimensional droplet profile $\theta_\perp = \theta_e + \Psi$, where Ψ is the maximum inclination of the side wall with respect to the top of the post. In three dimensions, the value of the advancing contact angle is not extreme as that predicted by Gibbs' criterion, due to the energy costs associated with the surface deformation from the spherical cap shape [85]. Nonetheless, $\theta_\perp$ is generally larger than the advancing angle parallel to the post $\theta_\parallel$ and the contact angle varies along the contact line. As a consequence, the droplet spreads preferentially along the parallel direction and hence the droplet shape is elongated parallel to the post.

This equilibrium behavior agrees qualitatively with very recent advancing contact angle measurements for a water droplet spreading on a photoembossed surface $\theta_e \sim 70°$ characterized by a periodic arrays of parallel ridges of pitch equal to $80\mu m$ and depth of $4.3\mu m$ [85]. Increasing the volume of the droplet, $\theta_\parallel$ remains essentially constant, while $\theta_\perp$ shows a saw tooth variation with the volume indicating periodic lateral pinning. However, from a quantitative point of view, the observed rises in $\theta_\perp$ with increasing volume are significantly different: in the range of ϵ considered here, it is less than $4°$ for the photoembossed surface, to be compared with increases of $50°$ observed in our study. This less efficient pinning effect may be a consequence of the rounded,

shallow profile of the photoembossed surface, whose ridges do not present the sharp angles of the PDMS posts.

The observed anisotropy in the measured contact angles is simply quantified in terms of the contact angle difference $\Delta\theta = \theta_\perp - \theta_\parallel$. Figure 6.11 shows this difference as a function of the eccentricity ϵ for all the droplets deposited on the various single posts. The error bars of the stainless steel data are large because of the difficulty in measuring small angles. The eccentricity values span a much ampler interval than previous works which investigated the anisotropy of water droplets forming a composite contact with arrays of PDMS grooves[99] ($\epsilon_{\max} < 0.2$) and a wetted contact with photoembossed surfaces [85] ($\epsilon_{\max} < 0.15$). In our case the PDMS set presents eccentricities varying from a few decimals to more than 0.6 (i.e. elongation $e = B_\parallel/B_\perp > 4$), while hydrophilic samples show only $\epsilon > 0.2$, due the limited post width related to the droplet volume. Smaller volumes were not considered because of uncertanties related to evaporation effects. As a first approximation, regardless of the nature of the surface and of the size of the post, most of the data nicely collapses on a straight line passing from the origin. Even the data taken on the NOA posts, which do not present a very regular rectangular cross-section, does agree with this linear trend. In figure 6.11 we superimposed the results of numerical simulations for $\theta_a = 75°$, which are found in good agreement with all hydrophilic samples. To get a better comparison we plotted two different linear relations $\Delta\theta = m\epsilon$ with $m = 120$ and $m = 150$. Most of experimental data are included in these relations. However, the PDMS data show significant deviations for ϵ above 0.4. Also for small values of ϵ we notice a different behavior of the PDMS data which lie above the $m = 150$ line.

The behavior for large ϵ values of the measurements in Fig. 6.11 can be better understood if we consider that in general the anisotropy $\Delta\theta$ depends not only on the droplet eccentricity ϵ but also on its volume as well. In terms of nondimensional variables, one can write $\Delta\theta = f(V', \epsilon)$, where $V' = 12V/\pi D^3$ is the droplet volume normalized to the droplet mean diameter $D = (B_\perp + B_\parallel)/2$ [99]. Following prescriptions reported in [99] we performed numerical simulations with the Surface Evolver software assuming an elliptic shape for the base contact line.

$$\left(\frac{|x - x_c|}{A}\right)^3 + \left(\frac{|y - y_c|}{B}\right)^3 = 1 \tag{6.1}$$

Details of the algorythim are reported in appendix D. The homogeneous contact angle of the surface is $\theta_a = 136°$ which reproduces the Cassie value on a PDMS ($\theta_a = 114°$) substrate where the air fraction is 1.113 times the PDMS fraction[1].

Results reported in figure 6.12 show the same linear increase of $\Delta\theta$ versus ϵ of the original data [99]. Furthermore, for the same value of ϵ, $\Delta\theta$ decreases as V' increases: the droplet tends

[1]These prescription are exactely the same of reference [99].

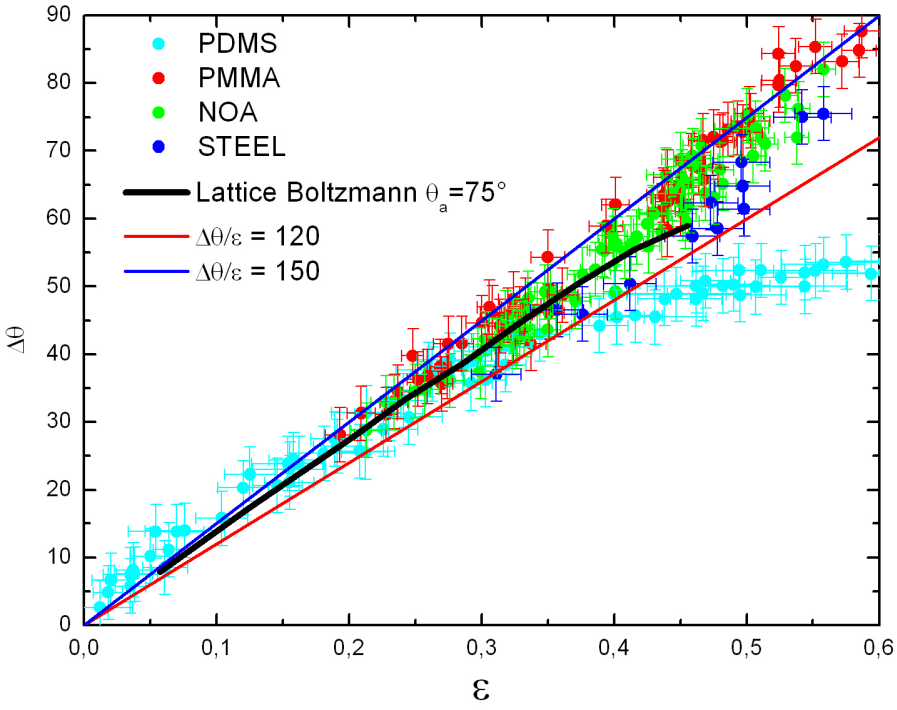

Figure 6.11: Experimental values of $\Delta\theta$ as a function of eccentricity ϵ. The curves represent numerical results for $\theta_a = 75^\circ$ (blue line) and the equations $\Delta\theta = 120\epsilon$, $\Delta\theta = 150\epsilon$.

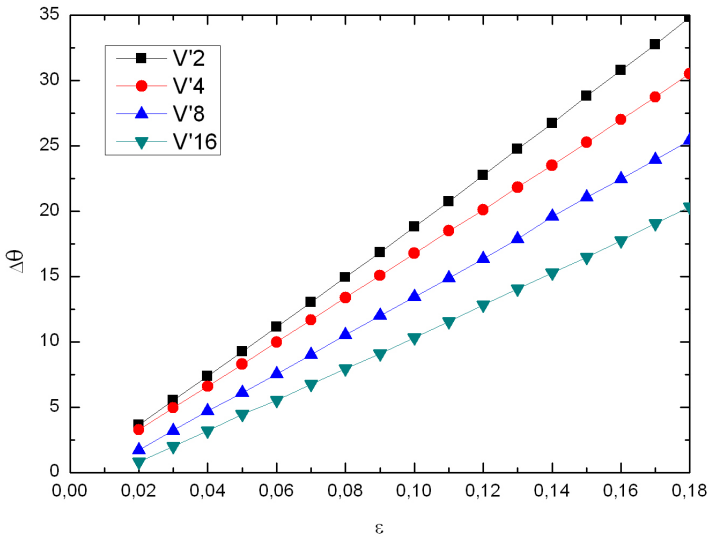

Figure 6.12: Plot of $\Delta\theta$ as function of ϵ for increasing values of V'. The plot is similar to the results of [99], assuming an elliptic contact line at the base of the droplet, for an hydrophobic substrate ($\theta_a = 136°$).

to be more spherical for larger volumes on hydrophobic substrates. These features should be qualitatively the same for a non-elliptic contact line. They are also shared by our experimental data, as shown in fig. 6.13 which plots the $\Delta\theta$ data in terms of V'. In these new coordinate axes, it appears evident that most of the data refer to the same reduced volume V' approximately comprised in the interval $0.5 < V' < 2$, while the PDMS data presents much larger V' values. The smaller $\Delta\theta$ measured on highly anisotropic droplets deposited on PDMS posts are in agreement with the numerical simulations.

The PDMS trend reported in figure 6.11 suggests that, when the droplet eccentricity approaches to 1 (i.e. the ratio between the two bases tends to infinity), the maximum $\Delta\theta$ should be close to $60°$. Assuming for simplicity an actual contact angle of about $\theta_a = 120°$, this fact implies that the maximum value of $\theta_\perp$ should be close to $180°$, while the Gibbs criterion perdicts $210°$. The limit value of $180°$ for the PDMS may be related to the particular post geometry: in this case the liquid prefers to move along the parallel direction on the pillar even though it costs some surface energy, rather than increase its curvature. We expect that a further confinement in this direction will produce also an increment of the contact angle, reducing the surface deformation and its energy cost. In the case of the hydrophilic samples, the Gibbs criterion predicts maximum orthogonal angles lower than $180°$. Experimental data show values of $\Delta\theta$ increasing linearly until

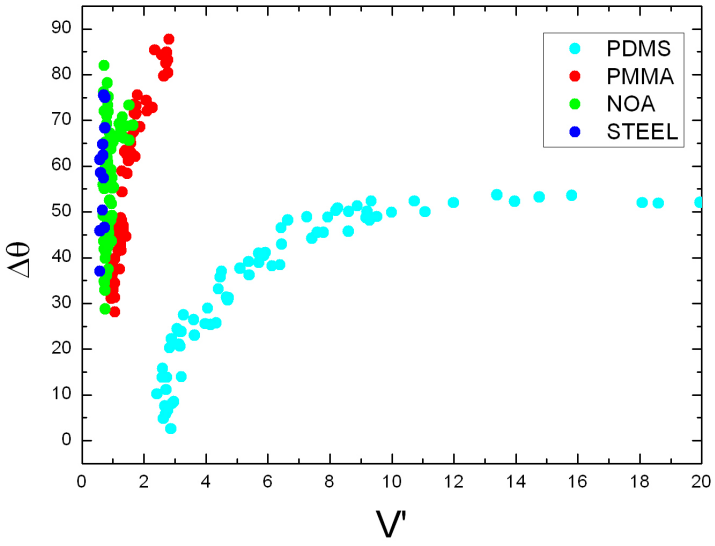

Figure 6.13: $\Delta\theta$ versus normalized volume V'.

90° when ϵ is about 0.6. This trend suggests that for higher values of ϵ, the $\Delta\theta$ should further increase.

6.2 Lattice Boltzmann simulations

In this section we report results of Lattice Boltzmann simulations. The method is described in detail in section 5. In most of the simulations, the system size is $L_x \times L_y \times L_z = 40 \times 60 \times 35$ lattice units (l.u.). The surface is characterized by a single post of width varying from 14 to 34 l.u. and height 5 l.u. The initial droplet is introduced by setting the density of liquid to $n_f = 4.128$ (simulation units) within a spherical cup of radius 13 l.u. The sphere is centered 12 lattice sites over the post plane. In this way, the initial configuration has a very little contact area mimicking the deposition process of the droplet. The remaining volume of the system is finally filled up with a gas of density $n_g = 2.913$. The initial droplet is then equilibrated on the post by iterating the LB algorithm for ~ 40000 number of steps. Note that an equilibrium interface of width of about 7 l.u. is formed between the liquid and gas phases, which corresponds to about 20% of the mean droplet diameter.

6.2.1 Density map scans

The profile of each droplet is obtained by performing a linear interpolation of the lattice points at which the local density assumes the threshold value $n_t = (n_g + n_f)/2$. This has been done by scanning the symmetry planes of the droplet in the orthogonal and parallel directions for the profiles and the height of the post for the contact line of the droplet. Numbering points with density $n > n_t$ one gets the volume of the droplet.

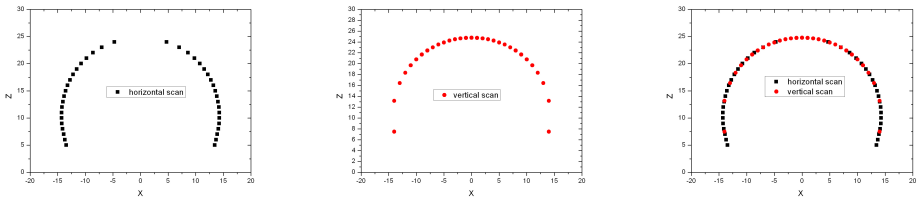

Figure 6.14: Construction of the simulated droplet profile by superposition of horizontal and vertical scans This example is referred to the orthogonal profile. The same for the parallel one, the contact line on the post and any other section of the droplet.

From the equilibrated profiles it is also possible to estimate the apparent contact angle along the parallel and the perpendicular directions of the pillar. The apparent contact angle should be in principle estimated by looking at the way the profile meets the solid surface of the pillar (contact line). However, while along the parallel direction the contact line is always horizontal, along the orthogonal direction the situation is less clear since there are situations in which the orthogonal droplet profile can spill over the edges of the post. This gives rise to a vertical contact line, as shown in figure 6.15 and for wide interfaces, as the one we are obtaining numerically, the local estimate of the contact angle strongly depends on the value of n_t chosen. This large uncertainty in the orthogonal contact angle estimate is due to the width of the liquid-gas interface in the Lattice Boltzmann approach, which is unphysically large with respect to the overall size of the system and it will be attenuated when simulations of larger system will be available.

6.2.2 Evolution of the droplet approaching equilibrium

Figures 6.16 and 6.17 show synthetically the evolution of the droplet during the minimization of the free energy. Data refers to the triple phase contact line [2] on the post and the two orthogonal profiles. Profiles are taken every 1000 simulation steps. These pictures nicely describe the time

[2] Strictly speaking profiles in figure 6.16 are the density map sections at the height of the post. If the droplet entirely resides on the post, they represent the numerical triple phase contact line.

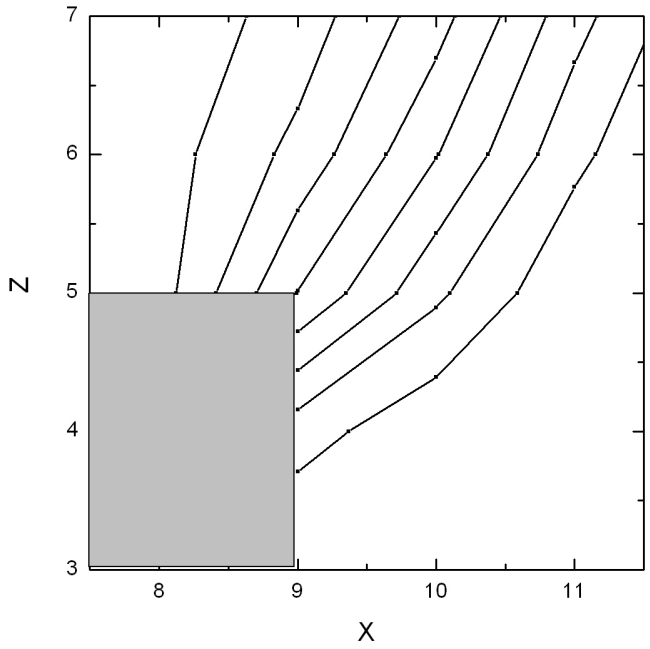

Figure 6.15: Droplet profiles obtained varying density threshold between 3.1 and 3.9 and comparison between elliptic fits in three cases. Data refer to a post 22 units wide and with $\theta_a = 70^\circ$.

behavior which mimics the droplet during the deposition process: initially the droplet appears as a sphere suspended on the post with a small contact. It quickly enlarges itself in an isotropic way, until it reaches the edge. After that the anisotropy starts increasing.

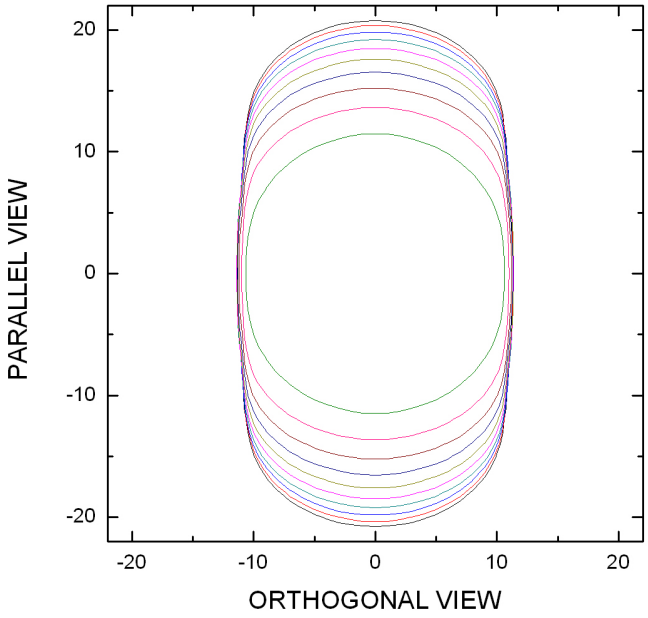

Figure 6.16: Evolution of the contact line during the simulation. This example refers to the 22 l.u. post width and $\theta_a = 60^\circ$ simulation.

Figure 6.18 shows the evolution of the droplet volume. Different curves correspond to different surface hydrophobicities while the post width is the same. Initially the volume is the same for all simulation. It is interesting to observe that in the three cases with low θ_a the volume decreases while for the highest value considered $\theta_a = 110^\circ$ it increases. In general the final volume is increasing with θ_a.

On the other hand, in figure 6.19 we consider a substrate with θ_a of 60°: increasing the post width the final volume increases (or, in other words, decreases less from initial configuration). To better compare simulation results, the linear dimensions are scaled by a factor $s = \sqrt[3]{12/\pi V}$. This normalization is chosen because the reference volume $V_r = \pi/12$ corresponds to a perfect hemispherical cup with a contact angle $\theta = 90^\circ$ and diameter 1.

As shown in figure 6.15, if we take the final configuration of a simulation and extract the

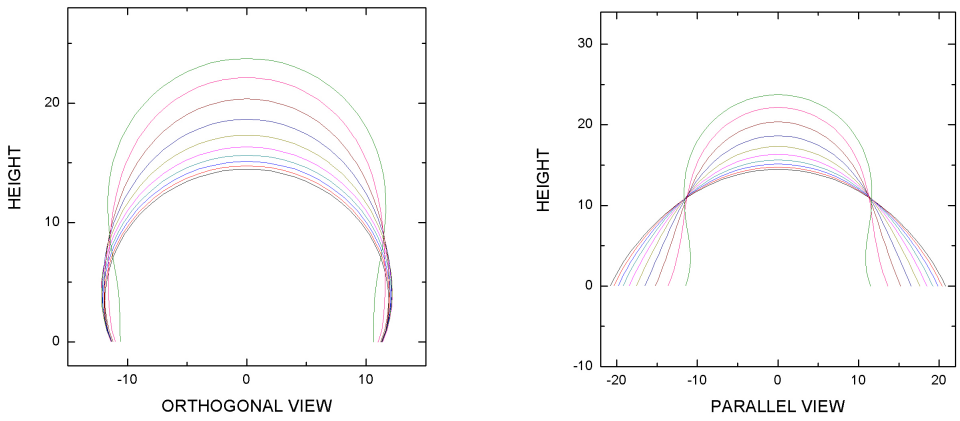

Figure 6.17: Evolution of the orthogonal (left) and parallel (right) profiles during the simulation. This example refers to the 22 l.u. post width and $\theta_a = 60^\circ$ simulation.

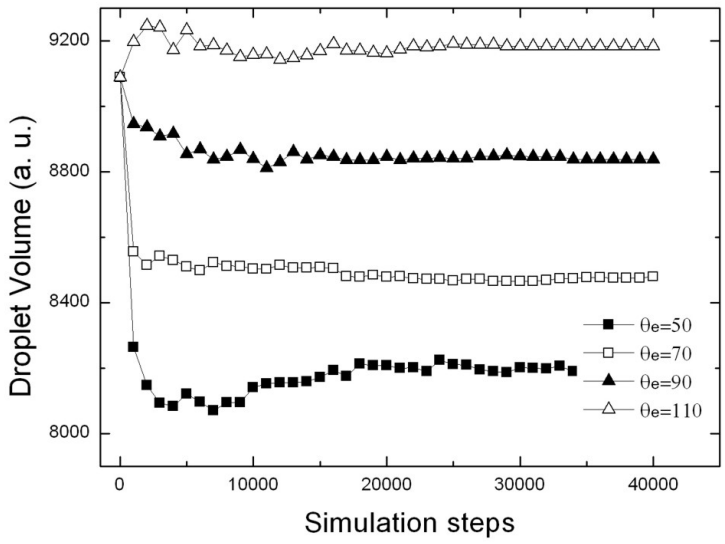

Figure 6.18: Time evolution of the volume of a droplet deposited an a single post of width 22 l.u. Different curves correspond to different surface hydrophobicities.

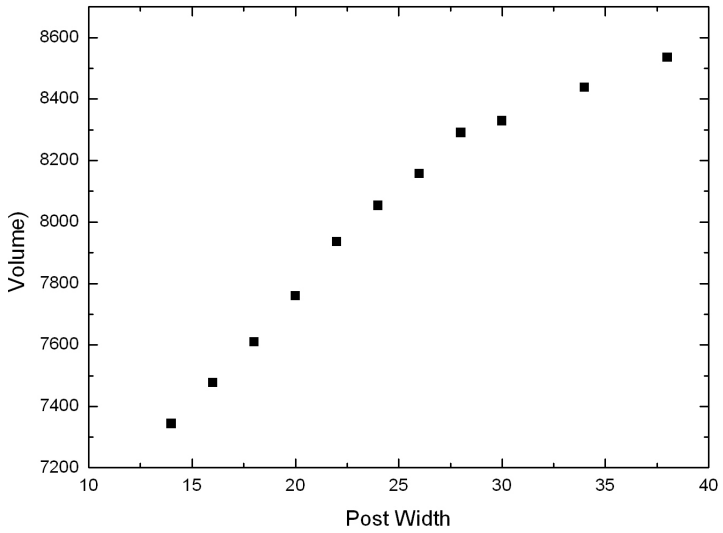

Figure 6.19: Details of simulations of posts with $\theta_a = 60^\circ$: dependence of volume from post size.

droplet profile by scanning the density map at various threshold densities n_t, the three phase contact line can fall on the post before the edge, or can spill out and touch the post on its vertical wall. If we use the same threshold density n_t to scan the final configurations of different post widths, for large posts the contact line is located before the edge while for narrow posts the contact is on the vertical wall. As a result, in this case the droplet width is exactly the same as the one of the post. In figure 6.20 we show the mismatch between the nominal post width and the effective droplet width in the orthogonal direction by plotting the difference scaled by the factor s as a function of the nominal post width. In this way all quantities are referred to the same nominal volume. We note that for small widths the difference is 0, and from a certain value which depends on θ_a it starts increasing. The value of the width where the difference appears, identifies the case where the contact line is close to the edge.

6.2.3 Contact line characterization

We report a superposition of the scaled profiles from set of simulations with homogeneous contact angle $\theta_a = 60^\circ$ (fig 6.21) and $\theta_a = 120^\circ$ (fig 6.22) for different post widths. Because of the variation of about 10% in the volume of the final configurations, we plot the profiles rescaled by $s = \sqrt[3]{12/(\pi V)}$. In the $\theta_a = 60^\circ$ case we observe that a progressive reduction of the post width

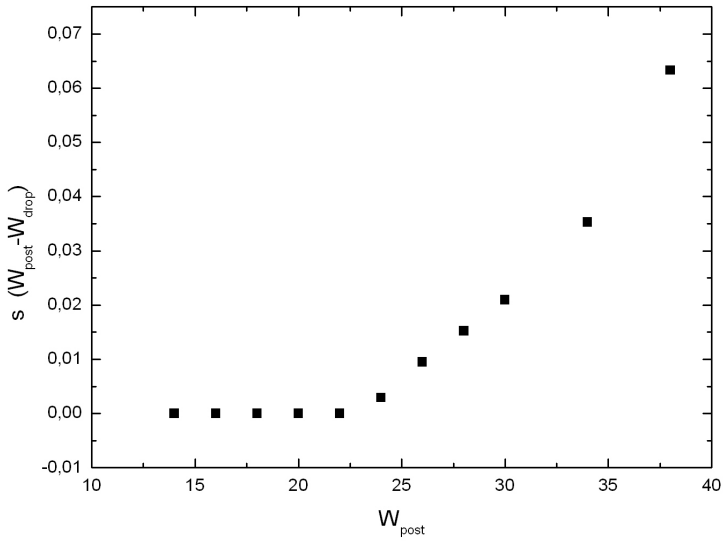

Figure 6.20: Details of simulations: difference between post size and contact line scaled by the factor $s = \sqrt[3]{12/\pi V}$ along the orthogonal profile.

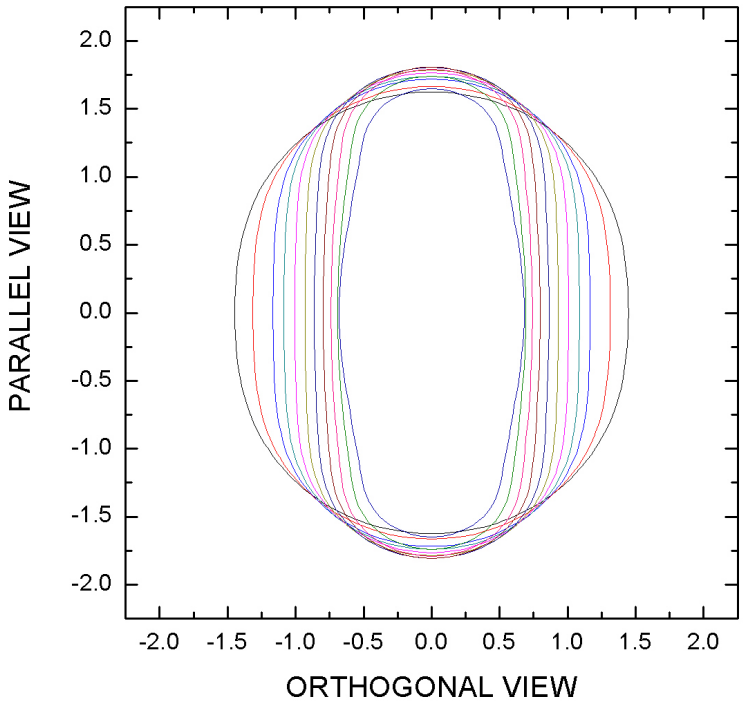

Figure 6.21: Superposition of the equilibrium three phase contact line for different post widths for $\theta_a = 60^\circ$.

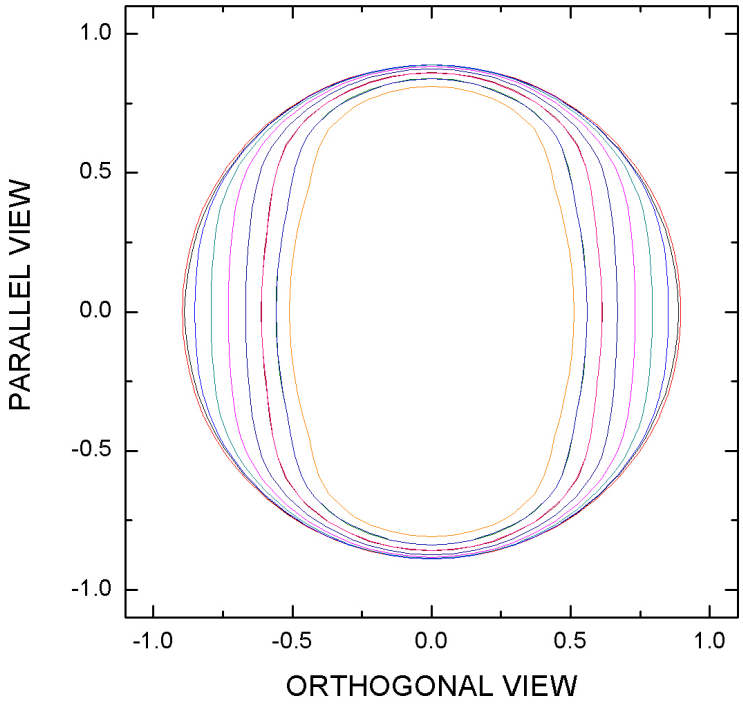

Figure 6.22: Superposition of the equilibrium three phase contact line for different post width in case of $\theta_a = 120^\circ$

.

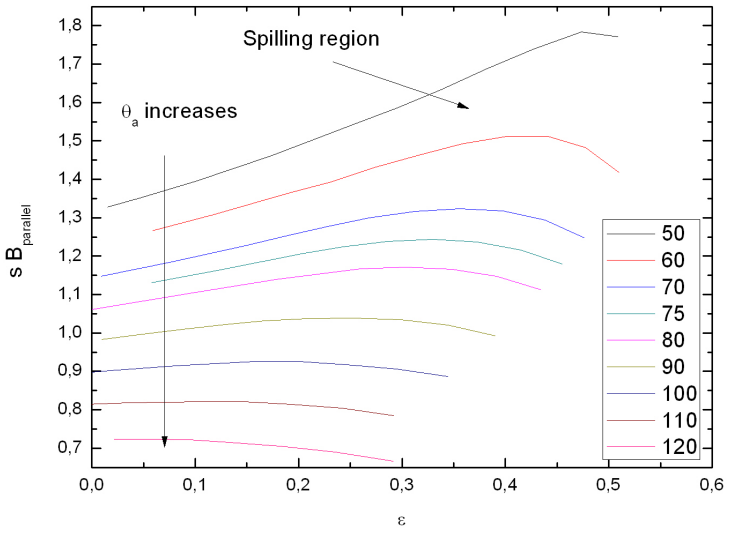

Figure 6.23: Behavior of the scaled parallel elongation $s \times B_{\|}$ as a function of eccentricity ϵ for various θ_a.

causes an increase of the parallel elongation. An exception is the narrowest configuration, where the elongation gets again smaller. This may be explained considering that in this case the droplet spills out partially, and so part of the volume moves in the spilling region. As a consequence, the other part of the droplet is slightly smaller and the parallel elongation decreases. The $\theta_a = 120°$ shows a quite different trend, where the parallel elongation does not change as the post width decreases. Also in this case, for large anisotropies, the spilling occurs again and the elongation decreases.

The simple system studied in this work allows a good characterization of the contact profile. We simply fit the numerical curves with a more general shape, where the exponent α is a free parameter.

$$\left(\frac{|x - x_c|}{A}\right)^{\alpha} + \left(\frac{|y - y_c|}{B}\right)^{\alpha} = 1 \tag{6.2}$$

Details of the calculations are reported in section A.1. In ref [99] results with $\alpha = 2$ and $\alpha = 3$ are compared, and $\alpha = 3$ is found to be in better agreement with experimental data. In figure 6.24 we show α values as a function of the base eccentricity ϵ for surfaces with different θ_a: Generally, the shape exponent α is a growing function of ϵ and for small anisotropies it is close to 2. Curves in figure 6.24 show a decrease of α for large anisotropies. This is due to the spilling effect observed in

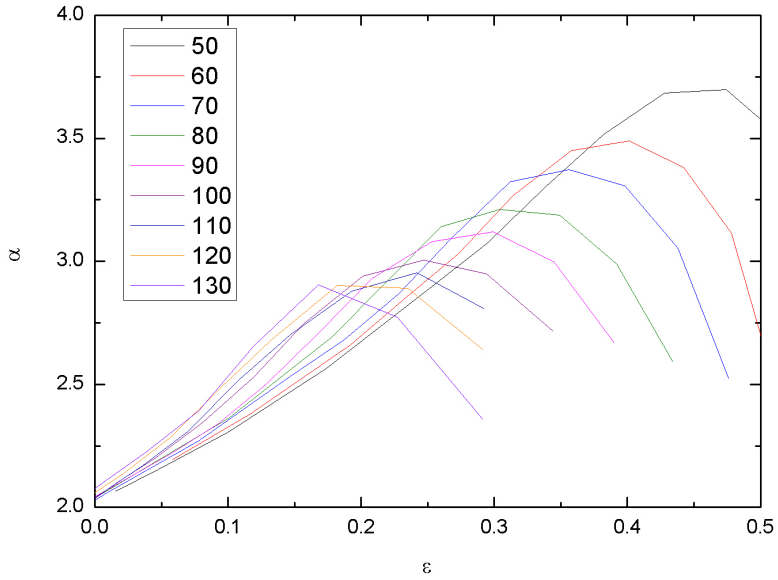

Figure 6.24: Values of the exponent α as a function of droplet eccentricity ϵ for various θ_a. The decrease registered for large ϵ is due to spilling effects, related to the unphysically large interface. Larger size simulations show that the growing trend continues also for large ϵ.

our simulations, and which are related to the unphysical large size of the interface. We performed a few simulations of larger size, observing that the spilling effect is proportionally reduced and the growing trend of α respect to ϵ continues also for large ϵ.

6.2.4 Profile characterization

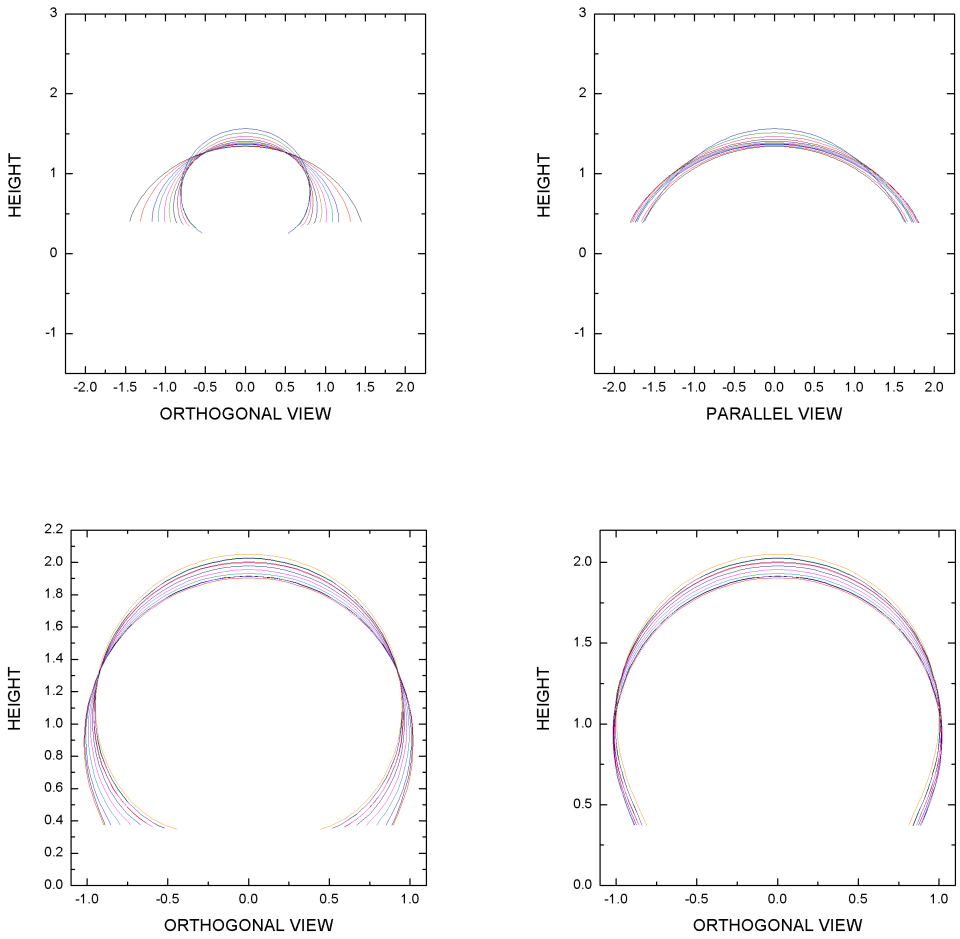

Figure 6.25: Superposition orthogonal (left) and parallel (right) profiles for different post width in case of $\theta_a = 60^\circ$ (top) and $\theta_a = 120^\circ$ (bottom)

In figure 6.25 a superposition of orthogonal and parallel profiles as a function of the post width is reported for $\theta_a = 60^\circ$ and $\theta_a = 120^\circ$. Here, one can measure the effects of base eccentricity on the droplet profiles in the two main directions. The elliptic fit seems to better describe the

numerical curve, although it does not fully take account of curvature deviations along the profile. In the experimental section the problem was solved by taking an elliptic fit only with points close to the surface. This choice was useful and found to work better than any linear / polynomial fit or than any global fit. In the numerical case, we met strong limitations to any local solution because of the very few points available For consistence we opted for a global elliptic fit, which is found to work well with small anisotropies, but no longer for larger ones.

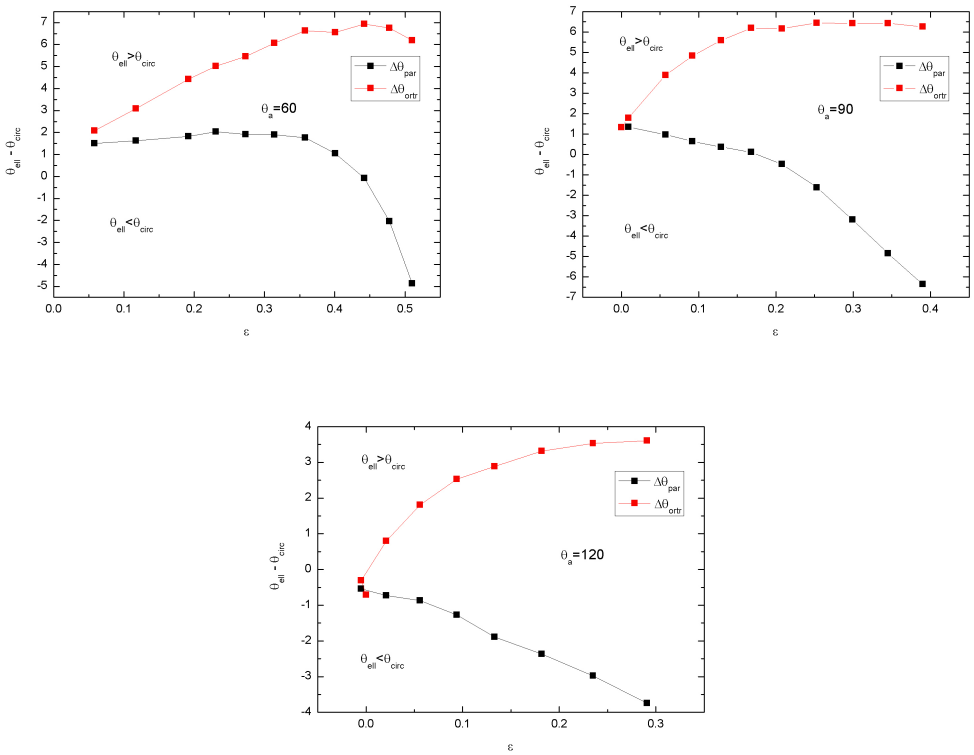

Figure 6.26: Difference between contact angle determinations from elliptic and circular fits both for orthogonal and parallel profiles. Set data refers to $\theta_a = 60°$ (left), $\theta_a = 90°$ (center) and $\theta_a = 120°$ (right)

To give an extimate of the deviations in the results, in figure 6.26 we plot the difference between the two determinations of the contact angles from the elliptical fit and the circular one as a function of eccentricity. Calculations refers to the $\theta_a = 60°, 90°, 120°$ set of simulations. For $\epsilon = 0$ the two determinations are similar both for the orthogonal and the parallel profiles. This means that no deviations are present and both the fitting procedures reproduce correctly the orthogonal contact angle. As ϵ increases the orthogonal difference increases (i.e, the elliptic determination is greater than the circular one) and for higher ϵ it tends to stabilize. The flatten portion

of the curve correspond to the spilling off region. This behavior is similar in all three cases analyzed and means that profile deviations are measured. We remark that in this case none of the two fits well reproduce the correct contact angle, but the elliptic one is closer to it. In this case a polynomial interpolation should work better if the contact line lies far from the corner. Unfortunately this condition is not verified and the elliptic fit remains the better determination. The same calculation for parallel contact angles shows an interesting difference: considering the no-spilling region, while for the $\theta_a = 60°$ case the difference remains constant as ϵ increases, for $\theta_a = 90°$ and $\theta_a = 120°$ we observe a clear decrease of the difference.

6.2.5 Global picture

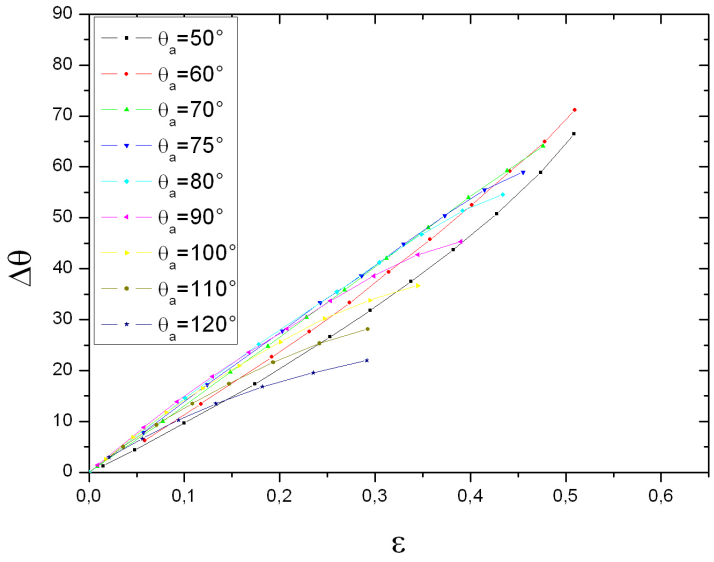

Figure 6.27: Plot of $\Delta\theta$ versus ϵ: Data refer to Lattice Boltzmann simulation for different values of θ_a.

In previous paragraphs details of the anisotropy quantities numerically simulated have been discussed . The main anisotropic relation between $\Delta\theta$ and ϵ is reported in figure 6.27: for different surface wettabilities the linear relation with low anisotropies is well reproduced. We note that generally hydrophilic substrates tend to increase the ratio $\Delta\theta/\epsilon$ as ϵ increases, while those hydrophobic show the opposite and in that case $\Delta\theta$ increase slowly. In addition in the hydrophobic case the growth is lower than experimental data of PDMS. This fact is related with the inadequacy of the elliptic fit adopted. Specifically the determination of $\theta_\perp$ is underestimated on hydrophobic

substrates, while $\theta_{\|}$ is overestimated. This means that the difference $\Delta\theta = \theta_{\perp} - \theta_{\|}$ is double underestimated for large anisotropies.

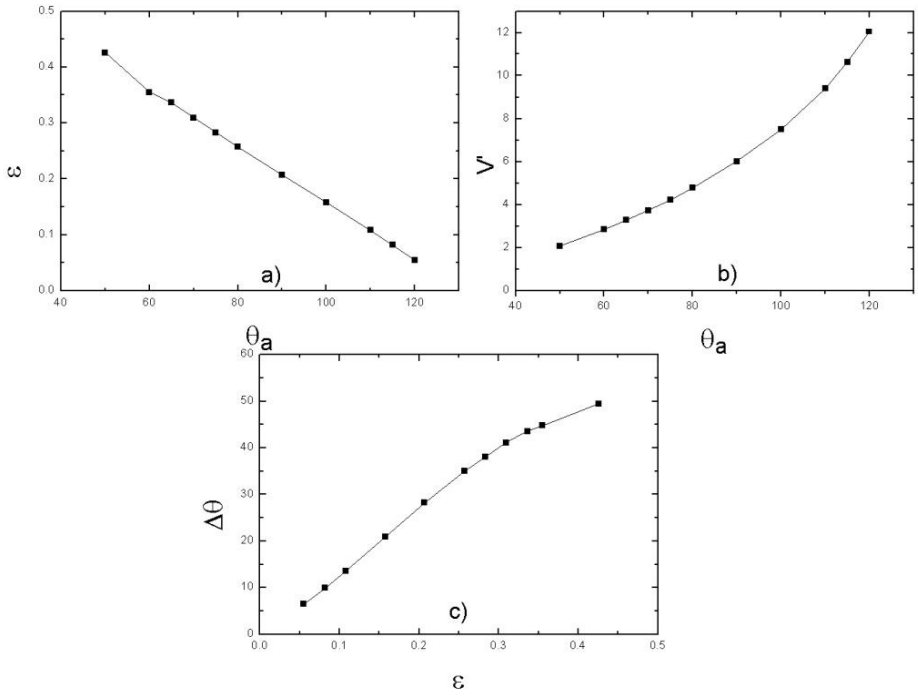

Figure 6.28: Lattice Boltzmann simulations with fixed droplet Volume and Post Width (22 l.u.). Each point refers to a different wettability of the surface θ_a ranging from 50° to 140°: a) The base eccentricity ϵ decrease with θ_a; b)V' increase as θ_a increase; c) $\Delta\theta$ vs ϵ.

To gain further information on the relationship between the droplet geometry and surface wettability we consider simulations for droplets sitting on a fixed post width $w = 22l.u.$ and different values of θ_a. The results are reported in figure 6.28 where we plot the base eccentricity ϵ as a function of the surface contact angle.

We find that ϵ decreases monotonically with θ_a. This is somehow expected since, if all other parameters are kept fixed, it is less energetically favorable for the droplet to move along the parallel direction of the post. For icreasing θ_a we have previously shown that the experimental data, if plotted as a function of the non-dimensional volume V', tend to fall into two distinct classes. This suggest that V' is a good indicator of the global geometry of the droplet even when it is highly distorted. It is then interesting to explore how V' varies with the contact angle θ_a for droplets

with a givenme volume V deposited on posts of orthogobal width w. In figure 6.28b we plot V' as a function θ_a. Note that V' increases faster than linearly as θ_a increases. On the other hand the higher is the surface hydrophobicity, the higher is the V' requested to increase the eccentricity ϵ. This results could explain the counter-intuitive results in figure 6.11 where we have very high eccentricity also for PDMS posts: they are characterized by having an extremely high value V'. Strictly speaking configurations with high V' are allowed because, due to the large hydrophobicity of the surface, it is not energetically favorable for the droplet to wet the sides of the very narrow post considered here. On the other hand, if the surface were made by a regular sequence of grooves, these rather extreme situations would not observed, because the droplet would find neighboring pillars to wet. Finally, in figure 6.28c we plot the relation between $\Delta\theta$ and ϵ obtained with this set of simulations. As remarked in the comment of figure 6.11, we see a linear relation between these two quantities. At low eccentricities, in addition, if we fix post size w (always entirely occupied by the droplet) and the liquid volume we demonstrate that for small anisotropy ($\epsilon < 0.3$) the main effect of changing θ_a is not the modification of this relation but simply the selection of the magnitude of the pair ($\Delta\theta$, ϵ) inside the same relation.

6.3 Geometrical model

In this section we propose a simple calculation of anisotropic parameters in the case of small eccentricity, e.g, when the droplet is close to an hemispherical cup, in order to obtain a qualitative behavior of anisotropy at varying of θ_a.

6.3.1 Relation between ϵ and $\theta_\perp$

Following [85] we consider the droplet profiles to be circular. In this approximation, the apparent contact angles can be written as

$$\tan\theta_\parallel/2 = h/B_\parallel \qquad \tan\theta_\perp/2 = h/B_\perp. \tag{6.3}$$

As a result,

$$\tan\theta_\perp/2 = e\tan\theta_\parallel/2 \tag{6.4}$$

where

$$e = \left(\frac{B_\parallel}{B_\perp}\right) = \left(\frac{1+\epsilon}{1-\epsilon}\right) \tag{6.5}$$

These relations allow to calculate the orthogonal contact angle $\theta_\perp$ simply as a function of the base eccentricity ϵ and surface wettability[3]. θ_a

[3]Details are reported in appendix C

$$\theta_{\perp}(\epsilon,\theta_a) \quad = \quad \arccos\left(\frac{\sin^2\theta_a - \left(\frac{1+\epsilon}{1-\epsilon}\right)^2(1-\cos\theta_a)^2}{\sin^2\theta_a + \left(\frac{1+\epsilon}{1-\epsilon}\right)^2(1-\cos\theta_a)^2}\right) \tag{6.6}$$

This equation is not correct for large values of ϵ because the assumption of constant curvature along each profile (circular shapes) does not satisfy the Laplace's law. In particular we have experimentally observed that this implies deviations of the curvature of the profile increasing with ϵ. The model should become more consistent for large ϵ if we introduce a mathematical description of curvature deviations, which at the moment is missing. However we can calculate the ratio $\frac{\Delta\theta}{\epsilon}|_{\epsilon\longrightarrow 0}$, which gives the initial slope as a function of θ_a. In this case it can be simply obtained by taking the first derivative of equation 6.6[4]

$$\frac{\partial\Delta\theta}{\partial\epsilon} = 2\sin\theta_a \times \frac{180}{\pi} \tag{6.7}$$

This equation is drawn in figure 6.29 and has a maximum for $\theta_a = 90^\circ$ equal to $360/\pi \sim 114$, and goes to 0 for both $\theta_a = 0^\circ$ and $\theta_a = 180^\circ$. We have calculated the same quantities from Lattice Boltzmann simulations, by fitting points with eccentricity $\epsilon < 0.2$. Error bars represent the standard deviations of the fits . The trend is qualitatively reproduced, and the maximum value is also found for $\theta_a = 90^\circ$, but its value is about 140. This higher finding is consistent with experimental results, for which the slopes are found between 120 and 150. Quite different is the behavior of the experimental PDMS sample, for which the ratio for small ϵ seems to be higher. Probably the curvature deviations are not the same in the case of hydrophilic and hydrophobic posts.

6.3.2 Calculation of the droplet volume

This geometrical model can be solved to give an extimate of the droplet volume for fixed ϵ and θ_a. In order to do this we must assume a shape to the base of the droplet. A possible choice is the generalized elliptic shape discussed in section 6.2.3

$$\left(\frac{|x|}{A}\right)^{\alpha} + \left(\frac{|y|}{B}\right)^{\alpha} = 1 \tag{6.8}$$

where the droplet is centered at the origin of the axis and $A = B_{\perp}/2$ ($B = B_{\parallel}/2$) is the perpendicular (parallel) semi axis. The local orthogonal elongation $x(y)$ is given by

[4]Details of calculation are reoprted in section C

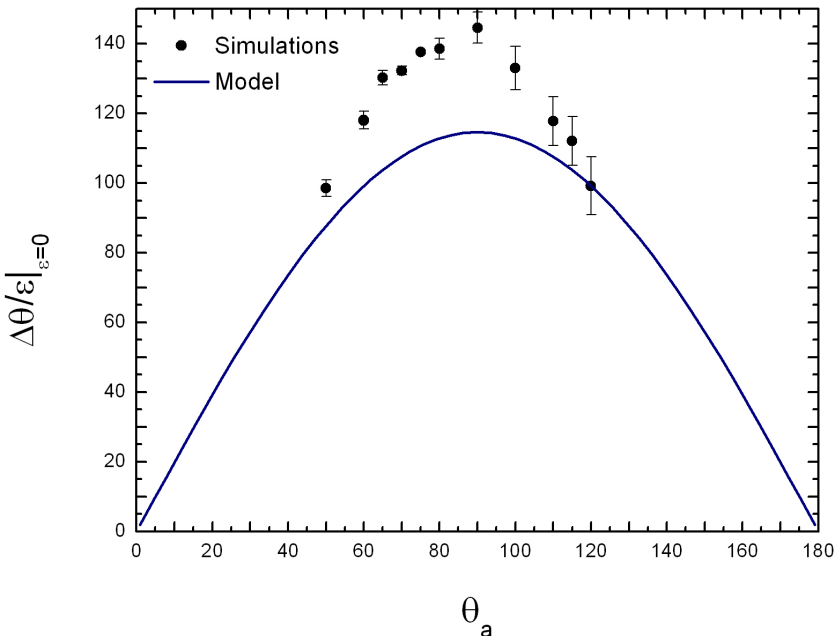

Figure 6.29: Derivative $\frac{\partial \Delta\theta}{\partial \epsilon}$ as function of θ_a: Points superposed are obtained from Lattice Boltzmann simulations.

$$x(y) = \sqrt[\alpha]{A^\alpha - \left(\frac{1-\epsilon}{1+\epsilon}\right)^\alpha y^\alpha} \tag{6.9}$$

and the local heigth of the droplet along the y axis is given by

$$h(y) = \frac{\sqrt{B^2 - y^2 \sin^2\theta_a} - B\cos\theta_a}{\sin\theta_a} \tag{6.10}$$

To get the droplet volume one needs to integrate the area of the circular portion from $-B$ to B if $\theta_a < 90°$. In case of $\theta_a > 90°$ the integration is extended to disks of radius $(h(y) - Z(y))/2$ from $-R$ to $-B$ and from B to R.

$$V = \int_{-B}^{B} \left[\frac{h^2(y) + x^2(y)}{h(y)} \arccos\left(\frac{h^2(y) - x^2(y)}{h^2(y) + x^2(y)}\right) - x(y)\left(\frac{h^2(y) - x^2(y)}{2h(y)}\right)\right] dy \tag{6.11}$$

We performed this calculation numerically and applied it to determine the influence of the three phase contact line shape in the volume of a droplet with the same base lengths and contact angles. It is also useful to estimate the behavior of ϵ as a function of the droplet volume, once fixed the droplet width, like in experiments, or as a function of the post width once fixed the droplet volume by the scaling factor $s = \sqrt[3]{12/\pi V}$, as in numerical simulation.

6.3.3 Influence of the three phase contact line

As reported in section 6.2.3 the shape of the three phase contact line depends on ϵ in a similar way for different θ_a. First we check the qualitative dependence of the droplet volume on the base shape. In figure 6.30 we report droplet volumes against α at varying ϵ in three particular cases: $\theta_a = 60°$, $\theta_a = 90°$ and $\theta_a = 120°$. In order to compare calculations the volume is divided by the volume obtained with the elliptic shape. As expected in all cases the volume increase as α increases and decrease as ϵ increases. In the hydrophilic cases the volume difference between the elliptic shape $\alpha = 2$ and when $\alpha \longrightarrow \infty$ is about 14% when $\epsilon = 0$, and less for greater ϵ. In the hydrophobic case this difference is about 10% for $\epsilon = 0$ and becomes very small as ϵ increases. The choice of $\alpha = 3$ proposed in [99] is found to produce intermediate volumes between the elliptic and square cases.

6.3.4 Behavior for $\epsilon \longrightarrow 0$

Assuming $\alpha = 3$, we calculated the volumes of droplets of given ϵ for different θ_a. To make a comparison with axperimental data, we plot in figure 6.31 the values of ϵ versus the scaled volume V/w^3: as noticed in section 6.8, for small volumes the eccentricity is null. Once the

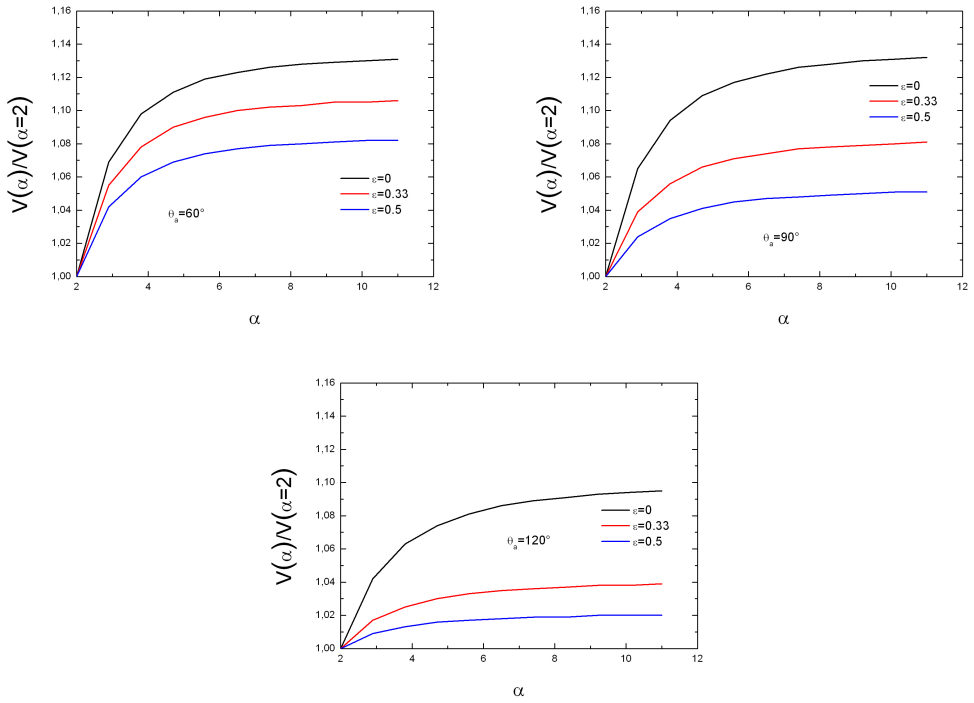

Figure 6.30: Droplet volume normalized to he elliptic case as functions of α and ϵ: left) $\theta_a = 60°$; center) $\theta_a = 90°$; right) $\theta_a = 120°$.

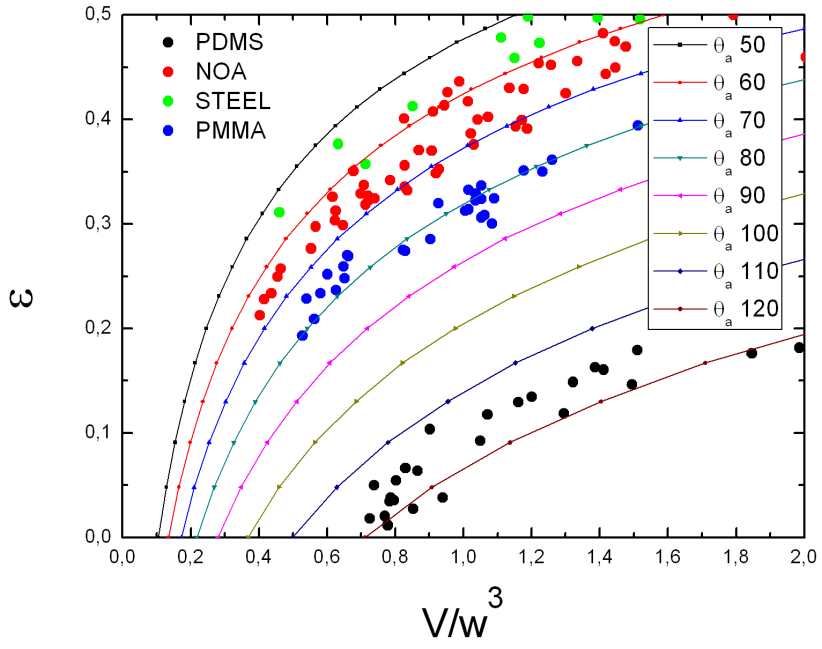

Figure 6.31: Eccentricity ϵ as function of scaled volume V/w^3 Experimental data from different samples are superposed.

volume reaches a threshold value which depends on the apparent contact angle of the substrate, the anisotropy starts appearing. The threshold value is given by equation 6.12.

$$\frac{V}{w^3} = \frac{\pi(1-\cos\theta_a)^2(2+\cos\theta_a)}{24\sin^3\theta_a} \tag{6.12}$$

The same calculation may be performed considering $\Delta\theta$ instead of ϵ. Also in this case (see fig 6.32) $\Delta\theta$ start increasing from the threshold volume. Behavior is similar to that of figure 6.31.

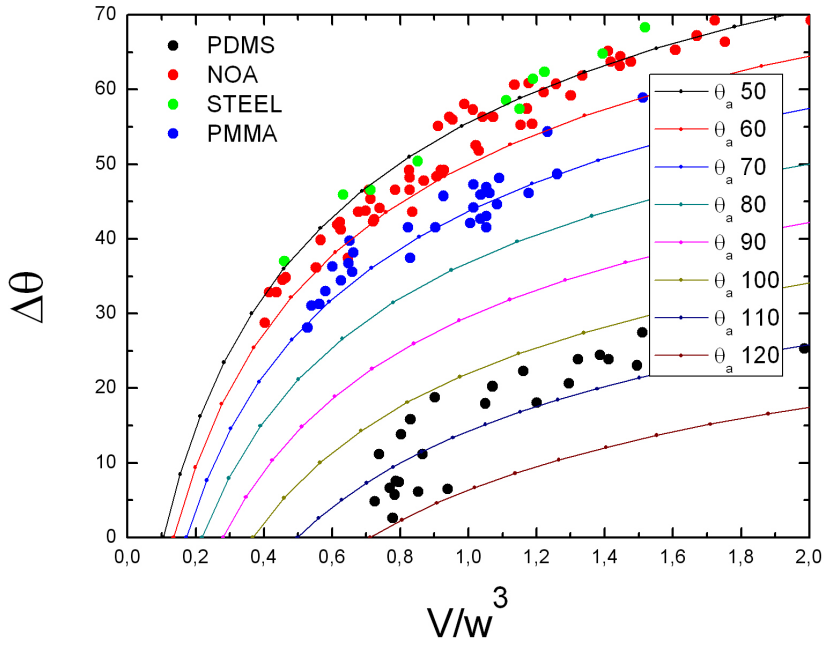

Figure 6.32: $\Delta\theta$ as function of scaled volume V/w^3 Experimental data from different samples are superposed.

To gain further informations on the relation between the anisotropy and the non-dimensional volume, we consider equation 6.12. In the case of $\epsilon = 0$ (spherical cup), the non-dimensional volume V' is proportional to $\frac{V}{w^3}$:

$$V' = \frac{12}{\pi} \times \frac{V}{w^3} \tag{6.13}$$

As pointed out previously, when $\epsilon = 0$ this relation is equivalent to the definition of the contact angle, and should be used to characterize the surface wettability. By definition, $V' = 1$ when $\theta_a = 90°$. Hydrophilic surfaces are characterized by $V' < 1$ and $\theta_a < 90°$ while hydrophobic ones by $V' > 1$ and $\theta_a > 90°$. If we consider equation 6.7, we can plot the slope values in the limit $\epsilon \longrightarrow 0$ as a function of V' (see fig. 6.34). It is clear that in this limit, the $V' = 1$ represent

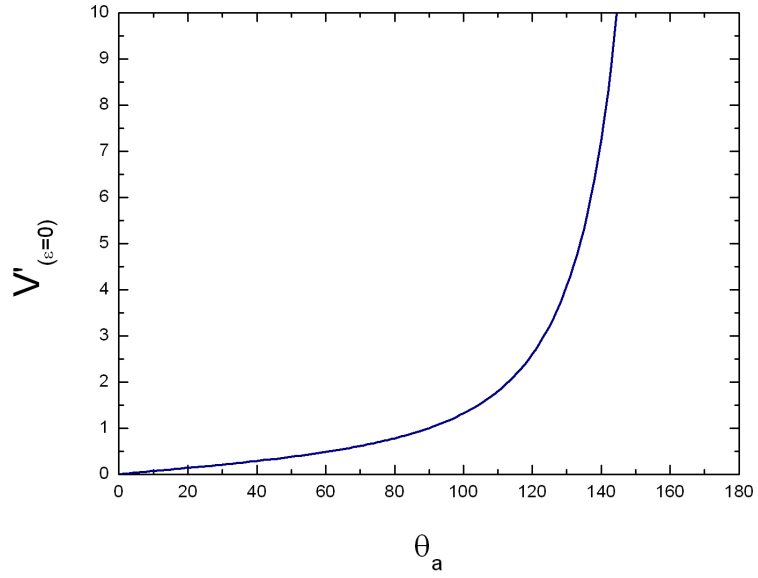

Figure 6.33: Nondimensional volume V' in the case of $\epsilon = 0$ as a function of θ_a

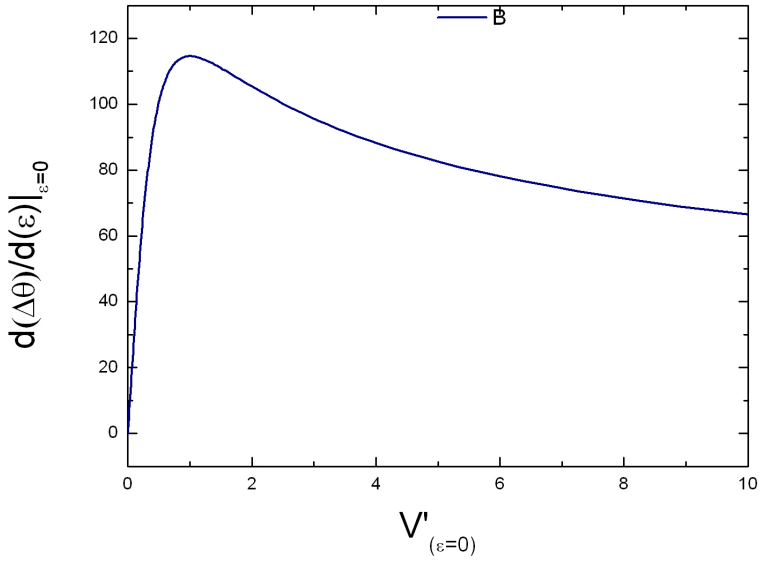

Figure 6.34: Derivative $\frac{\partial \Delta\theta}{\partial \epsilon}$ as a function of $V'(\theta_a)$

a maximum in the slope. Both for higher and lower values of V' the ratio $\Delta\theta/\epsilon$ is lower. In other words, in the condition of $\epsilon = 0$, this relation suggests that when $V' < 1$, an increase of V' is related to an increase of the slope, while when $V' > 1$ an increase of V' is related to a decrease of the slope. Now consider the situation of small ϵ: an increase of V' when $V' < 1$ implies an increase of $\Delta\theta$, while when $V' > 1$ it implies a decrease of $\Delta\theta$. This behavior is the same as that observed with the Surface Evolver simulations for hydrophobic substrates and $V' > 1$, reported in 6.12. We verified a similar simulations reproducing a hydrophilic substrate characterized by a contact angle $\theta_a = 50°$ (figure 6.35). As expected $\Delta\theta$ increases with increasing ϵ, and for the same value of ϵ, $\Delta\theta$ increases as V' increases. We notice that despite the same trend, the calculation

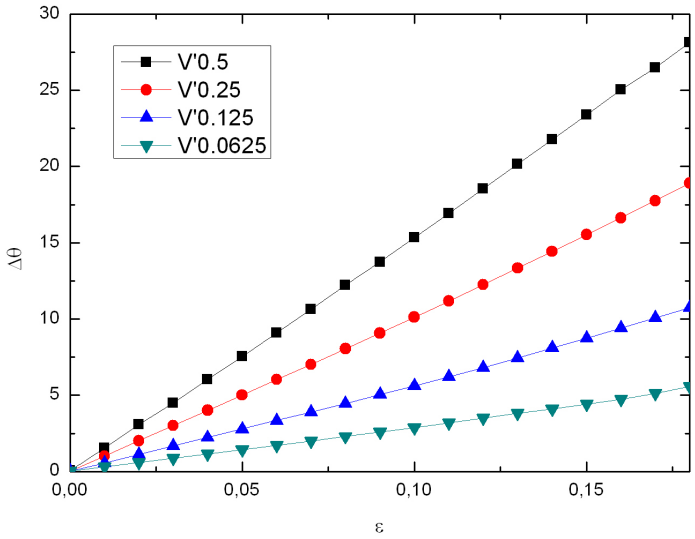

Figure 6.35: Plot of $\Delta\theta$ as function of ϵ for increasing values of V' for an hydrophilic substrate ($\theta_a = 50°$).

with the model and the Surface Evolver simulations are characterized by a strong difference: in the first case ϵ is considered constant and small, and the V' variation is caused by a variation of θ_a; in the second case we have the opposite: θ_a is considered constant (hydrophobic or hydrophilic) and ϵ varies causing a variation of V'.

A qualitative dependence of V' from ϵ may be obtained from Lattice Boltzmann simulations (see figure 6.36). When $\epsilon \longrightarrow 0$ the values are close to that in equation 6.33. As ϵ increases V' also increases. The higher is the starting value, the higher is the increase.

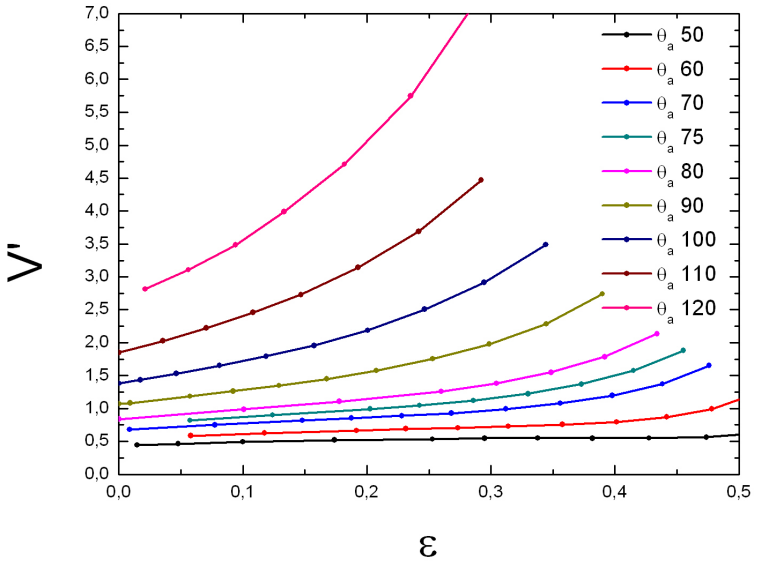

Figure 6.36: Plot of V' as a function of ϵ for different values of θ_a.

6.4 Discussion

In this chapter we have presented a wide characterization of the anisotropy, based on both experimental and numerical studies of a simple system constituted by a single linear post which substains the whole droplet and limits its expansion along the orthogonal direction. The main advantage of this approach is the absence of a defined micrometric structure under the droplet and the ability to study very narrow supports compared to the droplet volume. In this way we could study droplets with a much higher anisotropy than that obtained on plain patterned substrates. In previous works like in [99] the anisotropy was studied by considering the surface hydrophobicity as a given parameter and varying the surface geometry. In our case we can focus on the relation between the contact angles and the base eccentricity by widely varying the surface hydrophobicity by taking different materials for experiments or by tuning the actual contact angle of the simulated posts.

When the surface is fine patterned with stripes or grooves, the parallel contact angle $\theta_{||}$ is found to follow the Cassie or Wenzel models [85; 103] and not to depend from the droplet volume, but only by the fine chemical or geometrical structure. In our case we have a flat structure, where the contact angle corresponds not more to a Cassie or Wenzel model, but simply to the Young contact angle θ_a of the flat substrate. In agreemet with these abservations we found that the parallel contact

angle $\theta_{\parallel}$ is constant within a few degrees, and equal to that predicted by the surface hydrophobicity θ_a. On the other hand the orthogonal contact angle $\theta_{\perp}$ is found to be greater than θ_a due to the pinning at the post edge. When the substrate is a collection of parallel spaced pillars and grooves, like in [85; 103], the final shape of the droplet depends on the ability of the liquid to overcome the multiple energy barriers. In this way it is strongly related to the deposition process. In our case the deposition process does not influence the final configurations, except for the presence of uncontrolled surface defects which act as local pinning centers and obstacle the elongation in the parallel direction.

Following Chen [99] we have characterized the anisotropy by two nondimensional parameters: the difference between orthogonal and parallel contact angles $\Delta\theta$ and the base eccentricity ϵ. According to previous studies we found these two parameters to increase as the droplet volume increases when the post width w is the same. Moreover, if we consider the volume normalized to the cube of the post widh for different posts, all data nicely collapse onto a single curve. We also found that $\Delta\theta$ and ϵ are related by very close linear relations, which appears to be the same into the error bars, for substrate of different wettability and hydrophilic character. However the set of measurements on the hydrophobic (PDMS) substrate show a quite different behavior: for small values of ϵ, $\Delta\theta$ is greater than in other samples, while for higher values of ϵ it increases with a slower rate, and seems to approach a limit value of about $60°$. We observe that the increase of anisotropy is related to an increase of curvature deviations of the droplet profile. We explain this behavior by noticing that, respect to an isotropic droplet, a greater anisotropy imply a greater radius of curvature along the parallel direction in proximity of the three phase contact line. In this way the liquid - air interface, in oder to obey to the Laplace law, changes its curvature by reducing the radius in the orthogonal direction. Probably the energetic cost of these curvature deviations prevents a further increase of $\theta_{\perp}$ greater than $180°$ when ϵ becomes large. We point out that these findings are located in a range of anisotropy ($0.3 < \epsilon < 0.6$) which has never been measured for hydrophobic substrates in previous studies.

Another advantage of our system consists in the possibility to test the Gibbs criterion for not stright contact lines: in the case of multiple grooves patterned surfaces the value of $\theta_{\perp} = 180°$ represents a geometrical limit because a further increase of $\theta_{\perp}$ causes the liquid to touch the following pillar, which is assumed to be close. In this way $\theta_{\perp}$ is reduced and the droplet width $B_{\perp}$ increased. Differently in our system $\theta_{\perp}$ could become higher than $180°$, if the liquid does not collapse down. We observe that in the case of PDMS the value of $180°$ seems to be the limiting value, due to the energy cost of the interface deviations related the the increase of $\theta_{\perp}$. In the hydrophilic case we observe that $\Delta\theta$ increases linearly until about $90°$ when $\epsilon \sim 0.6$. A further increase of the droplet volume or a decrease of the post width causes the droplet to collapse down. This observation seems to agree with the 2D Gibbs criterion, but we have to consider that the

droplet profile is blurred in the orthogonal view because of the elongate shape of the droplet (all cases) or because of the presence of dark regions in the images (Stainless Steel sample) or because the post corners are slightly rounded (NOA) and facilitate the droplet to collapse.

This behavior may be also explained in terms of the nondimensional volume of the droplet V', which is found to increase as ϵ increases. As reported in [99], a change of V' implies a change in the ratio $\Delta\theta/\epsilon$. Our measurement, in agreement with these statements, show very similar values of V' fo the hydroplilic substrates, while the hydrophobic one show great values with a wide variation inside the same set of measurements, and depending on the base eccentricity.

All these results are nicely reproduced by numerical simulations based on the Lattice Boltzmann algorithm. The main difficulty found with the numerical simulations are related to the unphysical large width of the liquid - air interface, with respect to the droplet volume. This problem is particularly relevant when one tries to extrapolate the orthogonal contact angle, because sometimes the profile touches the post on the vertical wall and sometimes on its top, depending on the post width and on the surface hydrophobicity. Because of the transition between these two states, a local determination of the contact angle is not consistent and a possible choice is to fit the whole droplet profile with an elliptic shape. In this way we loose partially the details of the curvature deviations. This effect is particularly relevant with hydrophobic posts, for which $\Delta\theta$ determinations are strongly underextimated. Despite these problems, results are in good agreement with experimental findings, and allow to investigate the changes in anisotropy by varying θ_a continously at fixed post widths. Results show that in these conditions, ϵ decreases linearly with θ_a, while V' increases faster than linearly with θ_a, and the main effect of changing θ_a is a change in $\Delta\theta$ and ϵ, while their ratio remains approximately constant.

We also developed a simple model based on the assumption of spherical shapes for the droplet profiles both in the orthogonal and parallel views, in the case of small ϵ. The main finding is that the ratio $\Delta\theta/\epsilon$ when $\epsilon \longrightarrow 0$ is not the same, but varies as $\sin\theta_a$, showing a maximum when $\theta_a = 90^\circ$. These findings are in qualitative agreemet with Lattice Boltzmann simlations, which show the same trend, but with higher values. On the other hand, the numerical results are compatible with experimental data, considering that in the range of tested wettabilities the relative differences are comparable with experimental error bars. Finally we extended the Surface Evolver simulation of [99] to the hydrophilic case, finding that the relation between $\Delta\theta$ and V' (at the same ϵ) is inverted.

In conclusion, the use of single posts having a very sharp profile simplifies the investigation of the droplet anisotropy reducing hysteretic effects caused by multiple wedges and allows to easily reach very elongated shapes. The main results of this work has been accepted for publishing on the scientific review Langmuir [104]

Chapter 7

Wetting on Cluster-assembled nanostructured titania substrates

Wetting properties of solid surfaces have fundamental importance in all phenomena regulated by the presence of interaction between the surface and the liquids or vapors. The possibility to control the wettability on surfaces of titanium oxide provides much interest because directly involved in the functionality of devices and systems of great importance: in the field of electrochemistry (gas sensors), catalisys, air purification and sterilization of the water [105]). Here we focus on the nanostructured titania oxide surfaces becouse their potential use as a substrate to grow human tissues.

The use of nanostructured titania ($ns - TiO_2$) is convenient because of the production of high porous material with high surface reactivity. This is an useful characteristic in those applications in which the interaction surface-atmosphere plays a fundamental role. An accurate study needs the production of homogenous films with controlled morphology and roughness. This has been possible by the use of the SCBD (Supersonic Cluster Beam Deposition) technique.

Recent studies carried at LGM laboratory in Milan [107] have demonstrated that the nanostructured TiO_2 films obtained by the deposition of a supersonic beam of TiO_x clusters are promising candidates for the immobilization of proteins. That study was involved with regards both a morphological and a wetting analysis of titanium thin oxide films produced at LGM using two different carrier gas in the deposition process.

In the following sections, after a short introduction to the properties of titanium and the biocompatibility of ($ns - TiO_2$), the SCBD deposition method for the coverings production is described. We then present a morphological characterization using AFM thechniques, which gives informations on Aspect Ratio, Surface Roughness and Fractal exponents. Finally results are compared with wetting measurements after several thermal treatments at temperatures of 100, 200 and

400 $^{\circ}C$.

7.1 Physical properties of titanium

Titanium is situated in the IV group of the periodic table with atomic number 22 and has excellent properties useful in engineering applications: low density, high mechanical resistance (like steel and twice that of aluminum), low elastic modulus, low heat conductivity, low thermal expansion, excellent resistance to corrosion, easy to work, biocompatible, not magnetic and stable up to extreme temperatures (thanks to its high melting point). Titanium exhibits an exceptional resistance to acids, alkali, natural water and industrial chemicals; at last, it offers a great resistance to the erosion (is at least twenty times more resistant to the erosion than copper-nickel alloys).

Environment resistance of titanium depends on a very thin superficial oxide film (mainly TiO_2) very stable above a very wide range of voltage and temperature. The film formation is particularly favorite when the oxidating character of the atmosphere increases; for this reason, titanium generally resists to reducing, slightly neutral and highly oxidants atmospheres till reasonably high temperatures. Titanium develops stable superficial oxides with high integrity, tenacity and good adhesion. Surface oxide on titanium, if scratched or damaged, can immediately reconstruct itself in water or air presence.

Titanium dioxide [108] owes its fortune to some peculiar properties: when stoichiometrically pure appears transparent; its refractive index is the highest after the diamond, but much cheaper; it is not toxic and absorbs UV rays. Titanium dioxide exists in three different crystalline forms: anatase, brookite and rutile. The thermodynamically stable phase is the rutile and is also that most common one in nature while the brookite one is the rarest. The various phases show different properties and have therefore preferential applications.

Titanium nanocrystalline dioxide films during the last years have been object of growing interest because of the wide use in multiple applications: its photocatalytic properties have been studied in the past twenty-five years for the removal of organic or inorganic components from the water or the contaminated air or for the disinfection from virus, algae, bacteria or fungi. Another application regards the photoelectrolytic solar cells; thanks to its biocompatibility it can also be employed in prosthesis coverings; moreover it is used for the realization of gas sensors.

7.1.1 Biocompatibility of $ns - TiO_2$ surfaces

Cellular behavior in vivo and in vitro is influenced by the mechanical, biochemical and topographical properties of the extracellular microenvironment where cells grow [110; 111; 112]. In particular, the biochemical composition and the mechanical behavior of the extracellular matrix (ECM) play an important role in many developmental phenomena. According to the most recent

studies on biomaterials [113; 114], cells can actively 'sense' and adapt to the surface of adhesion and activate specific intracellular signals that influence cell survival and behavior. In vivo, cell attachment is the consequence of the binding with specific cell adhesion proteins in the ECM, and it is intrinsically influenced, besides by receptor-ligand specific interactions, by the physical and mechanical signals arising from the topography of the external environment [110; 111]. In vitro, on the other hand, cells set up a complex network of interactions both with the artificial surface and with the secreted and serum ECM proteins. The possibility of optimizing cell-substrate interactions can open up new perspectives in the design of biomimetic supports [115; 116].

The topography of the ECMs is characterized by features over different length scales ranging from the nano to the mesoscale and it regulates the cellular behavior in a way that it is still far from a complete understanding. The coexistence of ECM features at different length scales is probably one of the key factors, however it is not clear if there is a hierarchical organization of different structures and to what extent the various length scales can influence cellular response.

In order to elucidate the role of substrate topography and to fabricate biocompatible interfaces capable of mimicking the physiological conditions of the extracellular environment, a large number of studies have been devoted to the investigation of cell interactions with artificially produced nanostructures such as pits, pillars, grooves, dots or random structures obtained by chemically or physically etching metallic, semiconducting and polymeric surfaces.

Particular efforts have been devoted to the topographical modification of titanium and titanium dioxide surfaces since these materials are amongst the most studied and well-characterized biomaterials [108]. Pure titanium and titanium alloys are frequently used as dental and orthopedic implants because of their excellent mechanical strength, chemical stability, and biocompatibility [117], which ultimately arise from the thin oxide layer that spontaneously forms on the titanium surfaces [108].

The aim of this study is to indagate wetting properties of nanostructured TiO_2 films obtained by the deposition of a supersonic beam of TiO_x clusters.

7.1.2 Controlling wetting properties of TiO_x

The ability to control the wettability of a solid surface is very important, and therefore it is useful to know the way of how to modify this property with opportune surface treatments. Several methods exist [125] in order to modify a TiO_2 surface to increase its wettability, in which rely on heat treatments, an electric field, UV radiation and modifications of surface chemistry. The photo-induction of wettability on TiO_2 sufaces is particularly effective. As an example a TiO_2 surface, although being originally slightely hydrophilic, becomes highly hydrophilic thanks to the excitation of charge carriers through the band-gap by means of UV light exposure.In the dark the surface gradually comes back to its little original hydrophilic properties.

Recent studies [126] have demonstrated that the laser treatment is a controllable and flexible method to modify wetting characteristics. The use of homegeneous pulse Nd: YAG laser beams on the surface, modify aspects like wettability. The measured angle θ is remarkablly reduced, index of the increase of wettability. The increase as a result of the laser treatment turns out being not proportional to the increase in surface roughness. This disproportion is due to the fact that the laser beams simultaneously alter other factors besides the surface roughness, like the surface chemistry (increase of the superficial oxygen content) and the characteristics of the surface energy (more polar microstructure). It is moreover demonstrated that the proliferation rate of osteoblasti is remarkablly increased on laser treated surfaces, which simultaneously show a quick increase of wettability.

An other study reported in [127]describes a pronounced change of wetting properties when the solid surface is exposed to low energy electron beams. A small exposure brings a decrease of wettability and to an increase of the contact angle. The beam has an energy $E_p = 100eV$ which modifies the surface free energy inducing a variation in the charge distribution. This method is much effective and precise becouse it is possible to control wetting properties and surface energy varying the time exposure to the electronic beam (and therefore the absorbed charge).

In our case we modified the chemical properties of samples with different morphology from SCBD depositions by applying thermal treatments and annealing at different temperatures in environment atmosphere. Generally the film is partially hydrossilated and becomes more hydrophilic, depending on tretment parameters.

7.2 Deposition technique

Nanostructured TiO_2 films were grown on round glass coverslips (15mm diameter, 0.13-0.16mm thickness, Electron Microscopy Sciences) by depositing under high vacuum a supersonic seeded beam of TiO_x clusters produced by a pulsed microplasma cluster source (PMCS). A detailed description of the PMCS and its principle of operation and can be found in Refs. [118; 119]. Briefly, the PMCS operation is based on the ablation of a titanium rod by a helium plasma jet, ignited by a pulsed electric discharge. After the ablation, TiO_x ions thermalize with helium and condense to form clusters. The mixture of clusters and inert gas is then extracted in vacuum through a nozzle to form a seeded supersonic beam, which is collected on a substrate on a robotized arm located in the beam trajectory.

By exploiting the aerodynamic separation and focusing effects typical of supersonic beams [120] it is possible to produce nanostructured TiOx films with a controlled spread not only of the thickness and morphology but also of the crystalline dimensions and the rutile/anatase ratio as described in Refs. [120; 121]. The principle of the aerodynamic focalization is discussed in

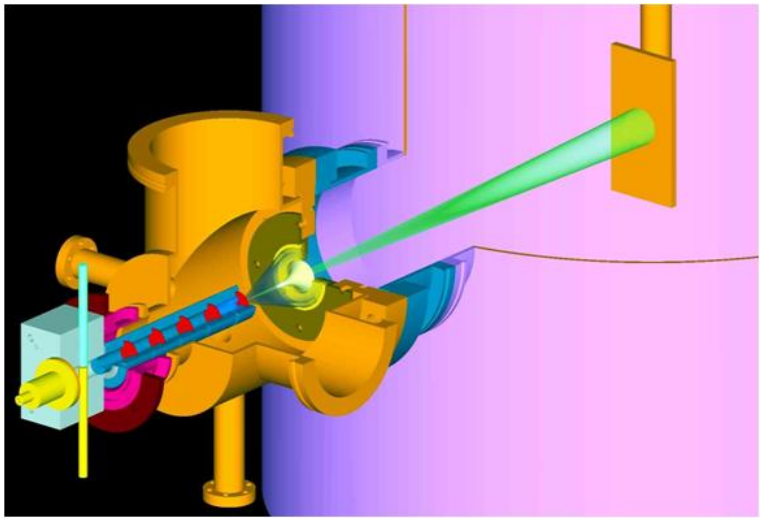

Figure 7.1: Schematic representation of the deposition apparatus: the deposition room (1) contains the substrate mounted on a robotized arm (2). The PMCS source operates outside the vacuum although been connected directly to the expansion room (3). The source consists in a pulse valve (6) for the injection of gas and in a ceramic body (4). In the cavity of the ceramic body there are two electrodes, the inner anode and the cathode which is eroded (5) perpendicular to the cavity. A system of aerodynamic valves (7) with five aerodynamic focusing lens, connects the source and the room of expansion. The cluster bundle formed in the expansion room enters in the deposition room passing through the skimmer and intercepts the substrate on which it is deposited.

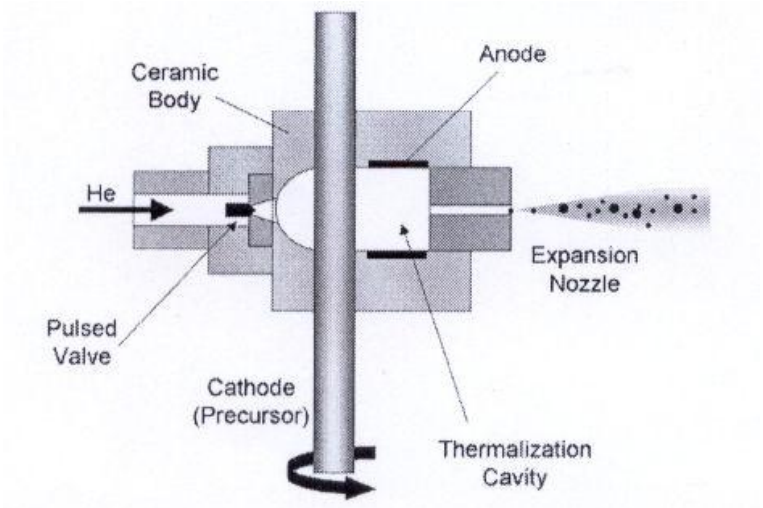

Figure 7.2: Schematic representation of the PMCS source

detail in [123; 124]. Shortly, an aerodynamic valve takes advantage on the competition between the dragging effect of the transport inert gas and on the inertia of the particle. Crossing every lens the gas is contracted and expanded. According to their inertia, the transported particles behave in different ways (figure 7.3). The two limit cases are typical of very small particles that closely follow the streamlines of the gas, and of very large particles that, because of their inertia, accelerate radially towards the beam axis when approaching the hole and therefore are projected above the axis going to impact on the opposite wall of the spacer. Between these two extreme cases, there are particles of intermediate dimension that are accelerated towards the axis but thanks to the smaller stop distance they finish their radial motion on a streamline closer to the axis than that on which they were originally. This allows an enrichment of this kind of particles on the axis of the beam.

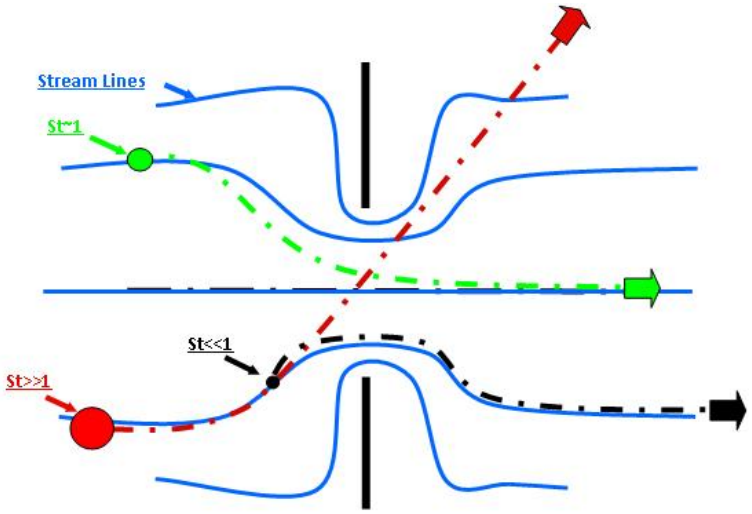

Figure 7.3: Schematic representation of an aerodynamic lens working: the key parameter is the number of Stokes (St), defined as the rate between the stop distance and the characteristic lenght of the system, and depends by the initial pressure, the nozzle diameter, and by the beam density and cluster dimensions. For a certain number of Stokes (St*) particles cross the center of the beam at the infinite, whic means that ther is no divergence of particles in the outing beam. If St is lower than St* particles has no enough energy to reach the center of the beam, ad follow the tream lines, while if St is grater, particles cross the center at a finite length and the divergence angle increases asyntotically with St. The optiman number of Stokes is 1.

The clusters kinetic energy is low enough to avoid fragmentation and hence a nanostructured film is grown. Further oxidation of TiOx clusters takes place upon air inlet in the deposition chamber [122].

The surface morphology of cluster-assembled films was characterized by atomic force microscopy (AFM) employing a Digital Instruments Nanoscope multimode IV atomic force micro-

scope in tapping mode. The nanostructure of the films was characterized by transmission electron microscopy (TEM), performed with a JEOL JEM-4000EX II operated at 400 KeV.

7.3 Characterization of cluster-assembled $ns - TiO_x$.

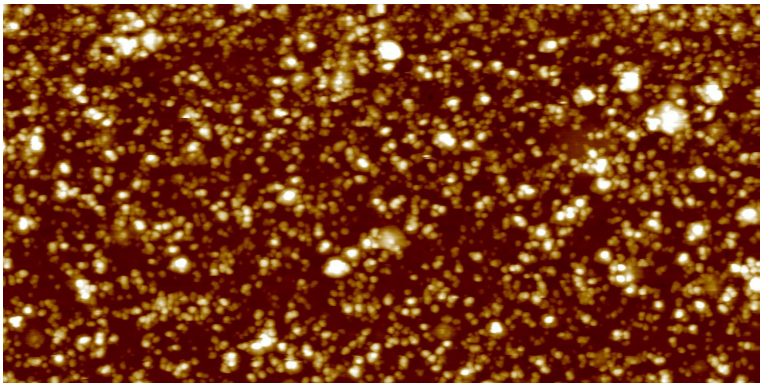

Figure 7.4: AFM image of a cluster-assembled $ns - TiO_x$ (Ar)

With the techniques previously described, several cluster-assembled TiO_x coverings has been produced

using both Argon and Helium as carrier gas, named

- Helium series (Dep1A, Dep2A, Dep1B, Dep2B)
- Argon series (3A, 3B, 3C, 3D)

Sample production and AFM characterization have been performed at the LGM laboratory of Department of physics of the university of Milan,while thermal treatments and contact angle measurements have been performed in Padua, at LAFSI laboratory. The full characterization shall be presented as follow:

1. Investigation of the influence of thermal treatments on surface
2. Characterization of the correlations between different morphological parameters related to wettability.
3. Characterization of the spatial scaling of the $ns - TiO_x$ interface.
4. Correlation of contact angles to morphological parameters.

Carrier gas	$\Delta\sigma(\%)$	$\Delta A_{spec}(\%)$	$\Delta(\sigma/\xi)(\%)$
He	1	1.7	2.8
He bis	0.3	0.7	7.8
Ar	3.4	3.2	9.6

Table 7.1: Relative discrepancies of morphological parameters after annealing (400 C).

7.3.1 Influence of thermal treatments on surface morphology.

Ns-TiO_x samples have been annealed at different temperatures (typically 100C, 200C, 400C for 2 hours) in Padua. The treatment consists of three phases: first a climb ramp from room temperature to 100 (200,400) °C at 240 °C/hour; second the thermal treatment over a time period of 2 hours; third a descending ramp whom velocity is not constant and depends on the thermal inertia of the apparatus (GERO standard furnace F-VS 100-500/13). As operating criterion samples are extracted from the furnace when the temperature has fallen down to $100 \pm 30°C$ for all treatments. Far from measurement operations, the samples are maintained in a vacuum cell to avoid contaminations from the environment. After each thermal treatment the samples Dep2B (He series) and 3A (Ar series) have been characterized by AFM and sent back to Padova for further characterization. In addition, a second $ns - TiO_x$ sample produced using He (He bis) has been annealed and imaged. We report the values of roughness, spec. area, and average slope measured after different thermal treatments at different temperatures. The relative discrepancy[1] for the different parameters is reported in Table 7.1. Samples deposited using He as carrier gas show very weak dependence on thermal treatments up to 400 C. Argon data are more scattered. We think this scattering can be mostly attributed to the fact that the thickness of Ar series samples was not extremely uniform. The slope parameters show the largest fluctuations. Average slope values however are affected by the large uncertainty in the correlation length (up to 20%). We conclude that post-deposition thermal treatments in air up to 400C have only negligible effect on the morphology of nsTiOx films, the fluctuations being well within the error bars.

7.3.2 Characterization of the correlations between different morphological parameters related to wettability

We could not obtain reliable measurements of thickness on samples deposited with He. Two of them were too thin (completely transparent), their thickness can be estimated to be in the range 1-10 nm; in the other cases, we measured the thickness of nominally identical samples that turned out to be not identical. The measurement of thickness for the Ar series can also be affected by

[1] Δ = std/mean

the presence of a residual thickness gradient on these samples. The knowledge of thickness is not critical for our study. The other morphological parameters can be directly related to the measured contact angles, because contact angles and morphological parameters have been measured in the same locations. In the following table it is shown the correlation of Specific Area and Slope with roughness.

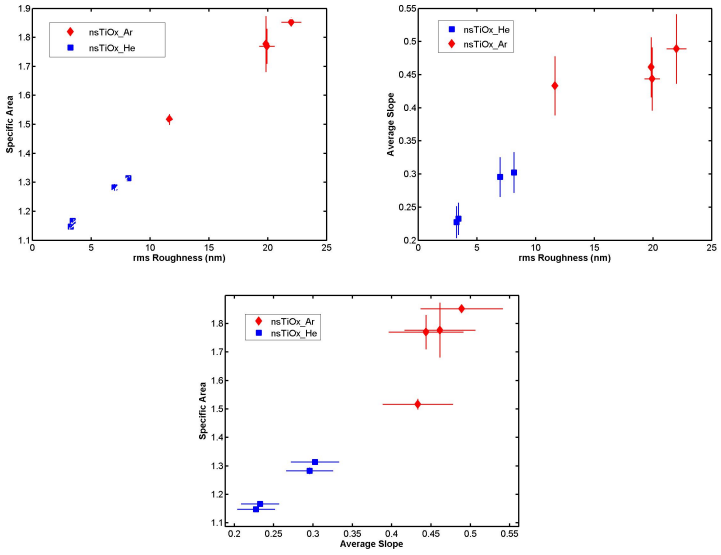

Figure 7.5: He and Ar series - Morphological parameters

Morphological data correlate well, apart from the slope of sample 3D of the Ar series. We have already noticed that this parameter is affected by the uncertainty on the measured correlation length. It can be noticed that the carrier gas (He or Ar) does not influence the scaling of morphology. It has in turn a strong influence on the maximum thickness: Ar allows depositing thicker samples, and obtaining the largest roughness and specific area values.

7.3.3 Characterization of the spatial scaling of the $ns - TiO_x$ interface.

We have characterized the scaling of the growing $ns - TiO_x$ interfaces. The scaling is typically described by two exponents, β and H, governing the evolution of the rms roughness σ with deposition time t (with thickness h in our case), and the in-plane height correlations [128]:

$$\sigma \sim t^{\beta} \sim h^{\beta} \tag{7.1}$$

Sample	σ **(nm)**	ξ **(nm)**	H
Dep1A(He)	3.64 ± 0.30	14.75 ± 1.40	0.837 ± 0.040
Dep1B(He)	3.30 ± 0.30	14.33 ± 1.40	0.860 ± 0.040
Dep2A(He)	8.17 ± 0.80	26.96 ± 2.70	0.796 ± 0.040
Dep2B(He)	7.11 ± 0.70	23.61 ± 2.30	0.814 ± 0.040
Reduced data	$\mathbf{0.997 \pm 0.003}$[3]	$\mathbf{0.999 \pm 0.014}$[4]	$\mathbf{0.807 \pm 0.010}$
3A(Ar)	22.08 ± 2.00	45.00 ± 4.70	0.788 ± 0.030
3B(Ar)	19.92 ± 2.00	43.00 ± 4.70	0.803 ± 0.030
3C(Ar)	20.38 ± 2.00	44.95 ± 4.50	0.840 ± 0.040
3D(Ar)	11.97 ± 1.00	26.87 ± 2.60	0.814 ± 0.040
Reduced data	$\mathbf{0.996 \pm 0.005}$	$\mathbf{1.001 \pm 0.017}$	$\mathbf{0.808 \pm 0.010}$

Table 7.2: Calculation of H exponent following $C2(r) = 2\sigma^2[1 - e^{-(r/\xi)2H}]$ [129].

$$\begin{aligned} C_2(r) &\sim r^{2H} \qquad (r \ll \xi) \\ &\sim 2\sigma^2 \qquad (r \gg \xi) \end{aligned} \tag{7.2}$$

where $C_2(r)$ is the height-height correlation function described in ref. [128], representing the mean-squared height difference of two points separated by a distance r. When the separation exceeds a typical distance ξ, the two points are uncorrelated. The thicker is the sample, the larger is ξ. For ξ spanning several decades, scale-invariance (fractality) is addressed.

We have calculated H an ξ of each sample fitting $C_2(r)$ vs. r with the following expression: $C2(r) = 2\sigma^2[1 - e^{-(r/\xi)2H}]$ [129]. Relative errors of 10% and 5% have been assigned to x and H accordingly. We have also fitted the reduced data of all samples of a given series with the same function[2]. Data are reported below.

The slope of the loglog plot of σ vs. h for the Ar series provides $\beta = 0.380 \pm 0.005$. Fitting data corresponding to $ns - TiO_x$ samples produced by Tethis srl provides $\beta = 0.42 \pm 0.01$. The data of the He series cannot be fitted because thickness measurements are unreliable

In summary, the scaling of cluster-assembled nanostructured $ns - TiO_x$ is characterized by the pair of exponents:

[2]We used the standard form (3 free parameters) instead of the reduced one: $C2(r)/(2\sigma^2) = [1 - e^{-(r/\xi)2H}]$ (1 free parameter) in order to account for uncertainties in the estimation of the correlation length and roughness associated to each curve. As expected, the first two parameters are compatible with unity within the error.

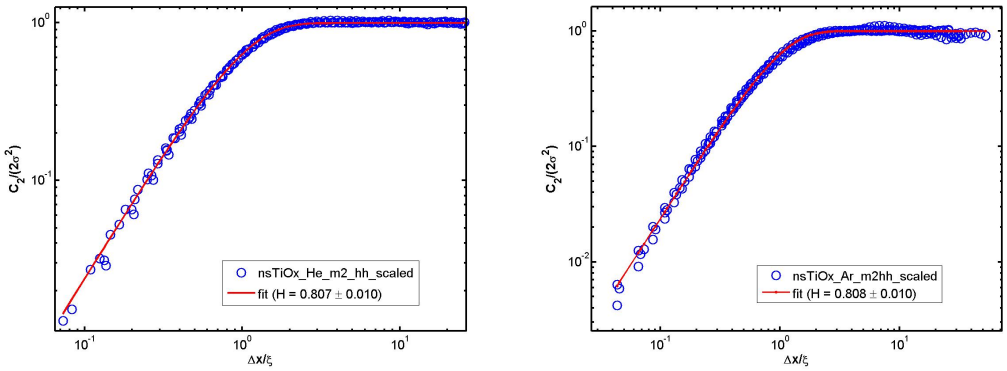

Figure 7.6: Scaling of the reduced height-height correlation function for He and Ar series.

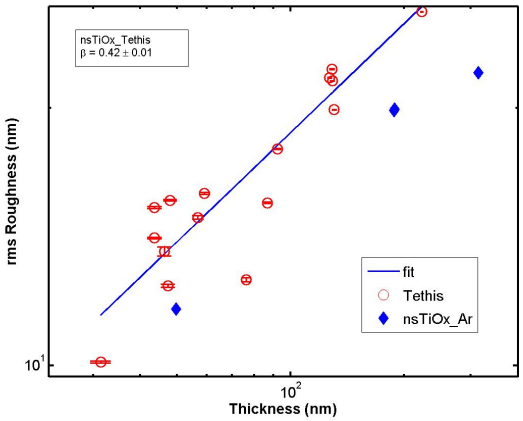

Figure 7.7: loglog plot of σ vs. h.

Sample	$\mathbf{T = 0^\circ}$	$\mathbf{T = 100^\circ}$	$\mathbf{T = 200^\circ}$	$\mathbf{T = 200^\circ}$ **(recovery)**	$\mathbf{T = 400^\circ}$	$\mathbf{T = 400^\circ}$ **(recovery)**
Dep1A(He)	95 ± 3	93 ± 2	76 ± 2	93 ± 2	30 ± 20	95 ± 1
Dep1B(He)	98 ± 2	97 ± 2	73 ± 3	91 ± 3	14 ± 8	95 ± 3
Dep2A(He)	123 ± 1	130 ± 1	71 ± 4	127 ± 2	0	126 ± 1
Dep2B(He)	118 ± 3	123 ± 3	73 ± 4	114 ± 4	0	114 ± 2
3A(Ar)	135 ± 4	140 ± 2	31 ± 4	142 ± 1	0	140 ± 1
3B(Ar)	130 ± 1	139 ± 1	27 ± 3	143 ± 1	0	140 ± 1
3C(Ar)	136 ± 2	141 ± 1	28 ± 4	142 ± 1	0	135 ± 4
3D(Ar)	108 ± 2	130 ± 4	47 ± 5	139 ± 1	0	131 ± 3

Table 7.3: Contact agle measurements on samples without treatments and after T100, T200 and T400 treatments. For treatments where wetting changes is shown the stable value after the recovery.

$$\beta = 0.42 \pm 0.01$$

$$H \approx 0.81 \pm 0.01$$

7.3.4 Contact angle measurements

Contact angles of water have been measured with the apparatus described in section 4. Small drops (volume $\sim 0.5ml$) of Milli-Q water were produced with the syringe pump and gently deposited on the surface. For each image, the overall drop profile was fitted with an elliptic curve and the error related to the fitting procedure was typically less than $\pm 1^\circ$. In order to get statistically sound results, at least five drops for each sample were typically analyzed. The representative contact angle θ was then taken as the mean of these different determinations and the corresponding standard deviation was around $\pm 2^\circ$. The contact angles have been measured on the samples "as received" and after thermal treatments at 100, 200 and 400 °C. In the table 7.3 is reported a summary of results, while in figures 7.8 and 7.9 are repported the curves of recovery for the highest temperature treatments. These curves are explained considering that thermal tretments produce a hydrosilation process, which clean the surface from OH-groups making it more hydrophilic (and for the higher temperature coplitely hydrophilic). As samples stay at rest they adsorb impurities from air and the environment, which give them back their original wetting character.

7.3.5 Correlation of contact angles to morphological parameters

To give a better comparison we plot the cosine of the contact angles vs morphological parameters for both the He and Ar series: it is clear from the measurements performed on the samples

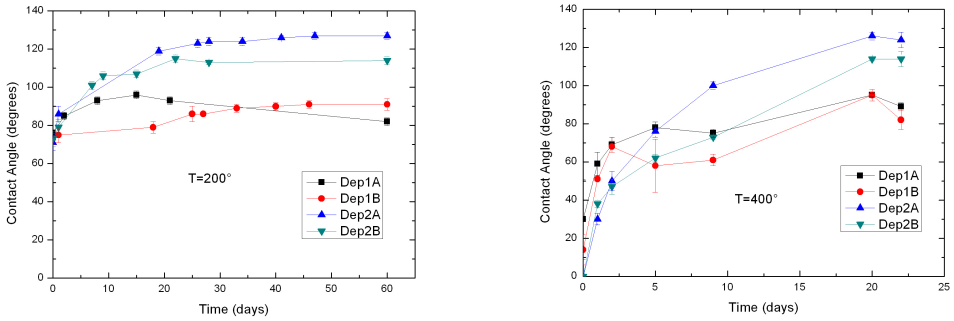

Figure 7.8: Recovery for He series, after T200 and T400 treatments.

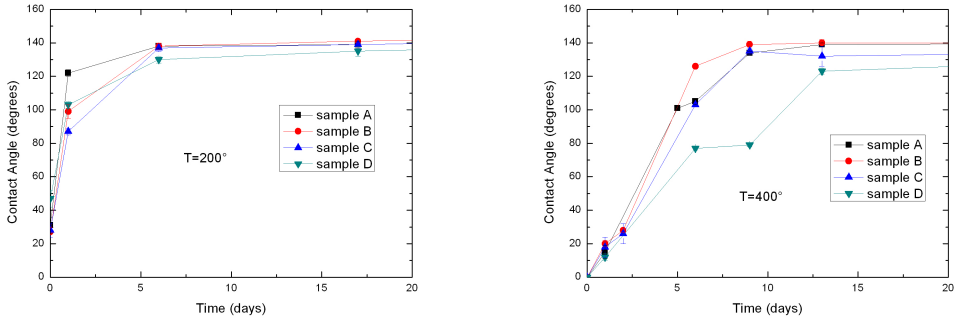

Figure 7.9: Recovery for Ar series, after T200 and T400 treatments.

as deposited that hydrophobicity increase both with specific area and roughnes. The heating up to $T = 100°$ substantially does not change this situation. The heating up to $T = 200°$ show a decrease of the contact angle in both the series. Intersertingly disappear any dependence on morphological parameters. This fact suggests that the chemical modifications produced by the thermal treatment overcome the the morphological ones, which are the same. The heating up to $T = 400°$ show a complete wetting behvior for most samples (except the less hydrophobic of the He series). Another intersting observation regards that after the recovery, the oiginal wetting properties are restored, and so the dependence of the contact angle from the surface roughness.

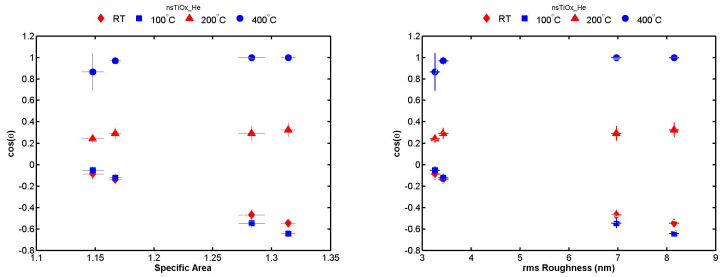

Figure 7.10: He series: contact angle vs. morphology: left) Specific Area; right) ms Roughness

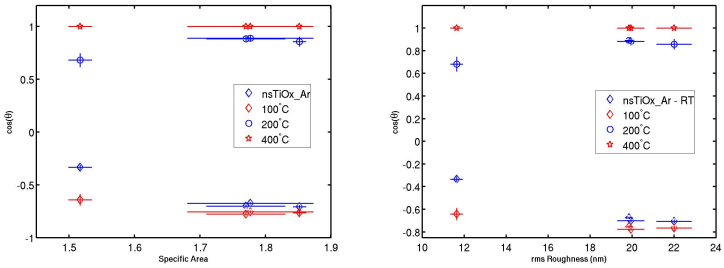

Figure 7.11: Ar series: contact angle vs. morphology: left) Specific Area; right) ms Roughness

Finally we compare together the measurements ot the two series, taken as deposited before any tretment. Data are linear interpolated by two well defined and different curves. We argue that this discrepancy is related to the different carrier gas ussed during the deposition process. Despite this discrepancy, we point out that these two fits converge to the same contact angle when the roughness goes to zero (flat surface) We measured this value on a flat rutile sample, and found the correct value.

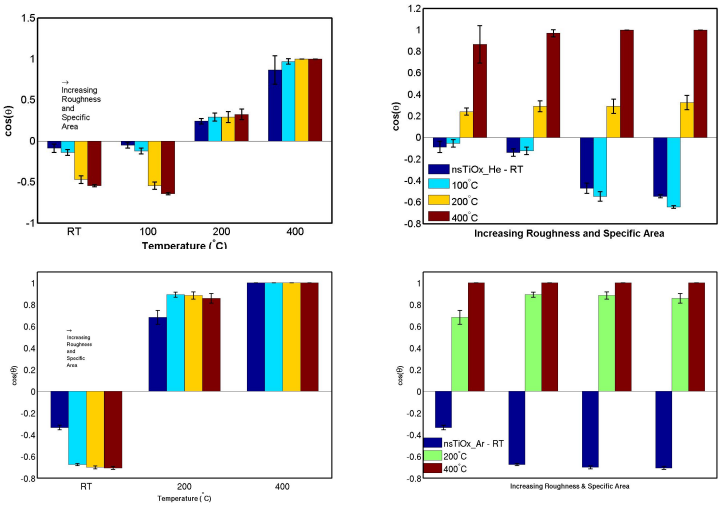

Figure 7.12: He and Ar series: comparison between morphologies and thermal treatments.

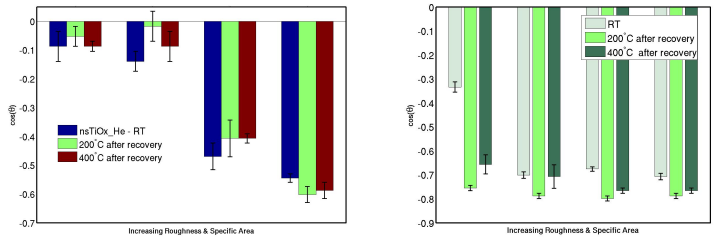

Figure 7.13: He and Ar series: comparison between morphologies and thermal treatments.

7.4 Discussion

In this chapter we characterized in detail the wetting properties related to surface morphology of nanostructured titania $ns - TiO_2$ surfaces. The surfaces were produced at LGM Laboratory in Milan, by the SCBD (Supersonic Cluster Beam Deposition) technique. This technique exploits the PMCS (Pulsed Microplasma Cluster Source) to ablate a titanium rod and produce clusters, which are filtered in size by aerodynamic separation. Samples were obtained using either He and Ar as carrier gas. Their morphology has been investigated by AFM measurements. Samples produced show different roughness, and specific area, but the unfortunately same fractal exponent H, which probably is related to this particular deposition technique. Morphological parameters were found to be stable after several thermal treatments, performed at growing temperatures respectively of $T = 100°C$, $T = 200°C$ and $T = 400°C$. Wetting properties were indagated by contact angle measuremets on the samples as produced and after each treatment. We found the contact angle to increase as the roughness and specific area increase, from values just beyond $90°$ to more than $130°$. Taking the cosine of the contact angle The $T = 100°C$ treatments does not produced substantial wariations in the wetting behavior, while the $T = 200°C$ significatively reduced the contact angle. We noted that in this case all samples show a common value. This fact suggests that in this case the chemical modifications of the surfaces induced by the thermal treatment makes not relevant the morphological differences between the samples. The $T = 400°C$ treatment show a further decrease, until the complete wetting for all samples of the Ar series. On the other hand, only the two most hydrophobic samples of the He series showed complete wetting for this treatment, while the two less hydrophobic ones showed a small but non vanishing contact angle. After about 20 days all samples recoverd the original wetting properties. We monitored these recovery curves in time, by taking periodic measurements. Another difference between the two series rises if we look to the cosin of the contact angle versus the roughness parameter: data are linear interpolated by two different curves. Probably this difference rises from the different carrier gas used during the deposition. However the two fits converge to the same value in the limit of a flat surface, which well reproduces the contact angle measured on a flat rutile crystall of titania.

These measurements represents a useful characterization of this kind of substrates in biological field. A more basic interest concerned a study of the correlation between wetting properties and fractal parameters of the surface. A numerical study was performens by Tartaglino et al. [130], which investigated the influence of surface roughness and its fractal exponent on superhydrophobicity, showing that while an increase of the roughness produces an increase in the contact angle, for the same fractal exponent, a variation of the fractal exponent at the same roughness does not produce a sgnificant variation in the contact angle. The first statement is confermed by our measurements, while, unfortunately, we could not werify the second one becouse of the impossibility of having samples with different fractal exponent.

Conclusions and Perspectives

In this thesis we have systematically investigated with experiments and with numerical simulations the elongated shapes of water droplets deposited on rectangular posts of mesoscopic size and different hydrophobicities. Except the case of the stainless steel sample, which has been produced in collaboration with the Department of Mechanical Engeneering, all samples have been produced in our laboratory with standard microfabrication techniques. We have measured the local contact angles and the base contact line elongations in directions parallel and orthogonal to the post with an homemade apparatus. The contact angle analysis software has been deveoped within this thesis. The contact angle meaured across the post has been found to increase with the drop volume, while that measured along the post, practically does not change, as observed in previous studies on patterned surfaces [99; 100; 85]. This has been explained in terms of pinning at the outer edges of the post and of free expansion along the post. The drop anisotropy has been simply quantified in terms of differences in the contact angles measured in the two views and of the eccentricity of the base contact line ϵ. All experimetal data collapse at the same linear relation between $\Delta\theta$ and ϵ except the hydrophobic PDMS sample. We related this discrepancy to the wide variation of the non-dimensional volume of the droplet. These experimental observations have been backed up by numerical lattice Boltzmann and Surface Evolver simulations and confirm previous investigations [99]. We also developed a simple geometrical model valid for small ϵ, whose analytical predictions are consistent with the experimental and numerical data.

The simplicity of the system we have studied, allowed us to focus on the strong curvature deviations of the profile, related to the anisotropy. To better understand the pining effects at the edges, we are planning to study the shape of a drop deposited on a pillar having a circular or rectangular section. To do this we are preparing new stainless steel masters (see fig. 7.14) with the micro electrical discharge milling technique formed by single micrometric pillars of different size and shape (cilindrical, square and rectangular). In particular we are interested in investigating the cotact angle increase as a function of the droplet volume for the square and circular pillars. We also plan to complement these measurements with Lattice Bolzmann simulations. In this case we also plan to improve the algorithm by taking account of the second order parameter in the expansion of the wetting potential of the Cahn theory and to rethink the wetting boundary

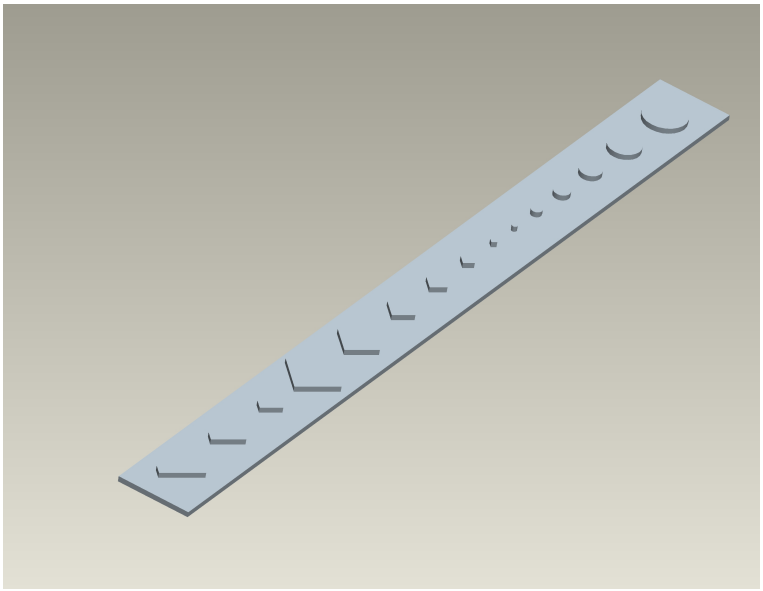

Figure 7.14: 3D view of the sample for the study of droplets suspended on single posts of different shapes.

condition at the pillar edges and corners, in order to allow a better determination of the local contact angles. Another improvement wil involve the optimization of the paralellized code, in order to faster the communications between computer nodes. This should allow larger simulations, with a lower interface / volume ratio, and a better definition of local properties.

In this thesis we also performed a characterization of wetting properties of nanostructured titania $ns - TiO_x$ films, relating them with their morphological parameters as deposited and after several thermal treatmens at different temperatures. We found the hydrophobicity to increase with surface roughness. Thermal treatments produced a consistent decrease of the contact angle, untill complete wetting. We also observed that the original wetting preperties were recoverd in about 20 days.

Appendix A

Analysis Tools.

In this section we will describe in details all numerical tools developed for the image analysis and for numerical simulations. All these tools have been developed ad hoc and upgraded during the work to match new problems and details. Tools are written with Labview software, and provide an upgrade of the facilities available of our laboratory. Here are reported only the latest compiled versions.

A.1 A generalized elliptic fit.

The core of all following analysis is the ability to fit points with circular and elliptic shapes in the best possible way. Several routines are available in several languages, but we chose to write down a new one to easily include in other programs. The most general shape we use to fit is given by

$$\left(\frac{|x-x_c|}{A}\right)^{\alpha}+\left(\frac{|y-y_c|}{B}\right)^{\alpha}=1 \tag{A.1}$$

where x_c and y_c are the coordinates of the center of the shape, A and B are the two main semiaxis and α is the exponent. When $\alpha = 2$ and $A = B$ we have the usual circular shape. When $\alpha = 2$ and $A \neq B$ we have the elliptic shape whose two semiaxes lie on the Cartesian axes and when $\alpha > 2$ we have a more general shape where the corners may be squared. This last freedom degree allows the fitting of contact lines of elongated drops and is very useful, where other methods are poorly fail. Given a set of points of coordinates $(\mathbf{x}, \mathbf{y})$, the distance from each of them to the curve is

$$\delta_i=\sqrt{\left(\frac{|x_i-x_c|}{A}\right)^{\alpha}+\left(\frac{|y_i-y_c|}{B}\right)^{\alpha}}-1 \tag{A.2}$$

and the global square distance of the points from the curve is given by

$$\begin{aligned} Q &= \frac{1}{N}\sum_i(\delta_i) = \frac{1}{N}\sum_i\left(\sqrt{\left(\frac{|x_i-x_c|}{A}\right)^{\alpha}+\left(\frac{|y_i-y_c|}{B}\right)^{\alpha}}-1\right)^2 \qquad (A.3)\\ &= \frac{1}{N}\sum_i\left(\left(\frac{|x_i-x_c|}{A}\right)^{\alpha}+\left(\frac{|y_i-y_c|}{B}\right)^{\alpha}-2\sqrt{\left(\frac{|x_i-x_c|}{A}\right)^{\alpha}+\left(\frac{|y_i-y_c|}{B}\right)^{\alpha}}+1\right) \end{aligned}$$

The partial derivatives respect x_c, A and α are given by

$$\begin{aligned} \frac{\partial Q}{\partial x_c} &= \alpha\frac{1}{N}\sum_i|x_i-x_c|^{\alpha-1}A^{-\alpha}\text{sign}(x_i-x_c)\times \qquad (A.4)\\ &\quad\left[\left(\left(\frac{|x_i-x_c|}{A}\right)^{\alpha}+\left(\frac{|y_i-y_c|}{B}\right)^{\alpha}\right)^{-1/2}-1\right]\\ \frac{\partial Q}{\partial A} &= -\frac{1}{N}\sum_i|x_i-x_c|^{\alpha}A^{-(\alpha+1)}\text{sign}(x_i-x_c)\times \qquad (A.5)\\ &\quad\left[\left(\left(\frac{|x_i-x_c|}{A}\right)^{\alpha}+\left(\frac{|y_i-y_c|}{B}\right)^{\alpha}\right)^{-1/2}-1\right]\\ \frac{\partial Q}{\partial \alpha} &= -\frac{1}{N}\sum_i\left[\left(\frac{|x_i-x_c|}{A}\right)^{\alpha}\ln\left(\frac{|x_i-x_c|}{A}\right)+\left(\frac{|y_i-y_c|}{B}\right)^{\alpha}\ln\left(\frac{|y_i-y_c|}{B}\right)\right]\times \qquad (A.6)\\ &\quad\left[\left(\left(\frac{|x_i-x_c|}{A}\right)^{\alpha}+\left(\frac{|y_i-y_c|}{B}\right)^{\alpha}\right)^{-1/2}-1\right] \end{aligned}$$

and $\frac{\partial Q}{\partial y_c}$ and $\frac{\partial Q}{\partial B}$ are analogous of $\frac{\partial Q}{\partial x_c}$ and $\frac{\partial Q}{\partial A}$. Parameters are changed in a loop j that minimizes the mean square distance following a steepest descent procedure ($P_i \longrightarrow P_i - k_i\frac{\partial Q}{\partial P_i}$), where P_i is respectively x_c, y_c, A, B and k_i is a useful velocity parameter which modulates corrections inside the loop. It may be set with different values if a faster descent of a parameter with respect to the others is requested. The ending loop condition is given by $Q_j - Q_{(j-1)} \leq 10^h$, where h is the precision requested. Usually $h = -9$. This minimization finds several local minima, and a check is required to verify the result. Usually this is obtained by a visual superposition of the resulting curve to the points, but if the this procedure is repeated many times, great accuracy is needed in the choice of the initial parameters. Solutions adopted will be discussed in the appropriate sections.

A.2 Profile Scan

Most of the experimental part of the work in this thesis regards an accurate measurement of the droplet contact angle. In chapter 4 the methods adopted are described with generality and the experimental apparatus is reported. Here we show the detailed description of how profiles are extracted and how they are fitted.

A point belonging to the droplet profile is obtained from a linear scan when its intensity varies more than the defined contrast C averaging F points. Usually $C = 20$ and $F = 4$. It is not always easy to have points on the whole profile, because the background of the image is not always uniform and light spots and geometrical details of the substrate (i.e. see figure A.2) or the presence of the syringe introduce points far from the profile. So the scan operation requires multiple area selections to define the regions of interest and the regions to avoid. Usually two selections are sufficient. The region of interest are always scans in the horizontal direction and, on request, also in vertical direction either on the top and / or on the bottom of the image.

A.3 Profile Cleaning

Despite this, the profile is always noisy, in reason of wrong pixels or shadows and reflections on the droplet. Before the fitting procedure, a "'cleaning"' one is requested. This operation is performed in three steps: first we calculate the best elliptic fit on the whole profile and perform aa coarse grained filter deleting all points far more than the tolerance parameter δD in the radial direction from this elliptical fit. Usually $\delta D = 25$ pixels. In this case the procedure is stable only if points belong to the whole profile. In the case of profiles constituted by only a small angular portion a visual check is required to avoid systematic errors. A second filter is performed dividing points in two separated sets (top and bottom) and fitting them respctively. This procedure allows to take account of curvature deviations on the bottom of the droplet, near the three phase contact line: when the profile is highly disterted, a filter based only on a single fit of the whole profile with small tolerance parameter δD would exclude some good points near the three phase contact line. Here usually $\delta D = 10$. Finally, a very fine filtering is performed on the remaining points by dividing them in 8 sets on their angular positions and separately filtered with $\delta D = 1$. This procedure is necessary when the profile is strongly distorted and the unique elliptic fit is poor when superposed to scan points, as shown in figure A.1.

A.4 Fitting Procedure

The software works fine when the drop profile is axial symmetric. In this case the double side determination can be replaced with the more efficient elliptic fit. If the fit is performed on

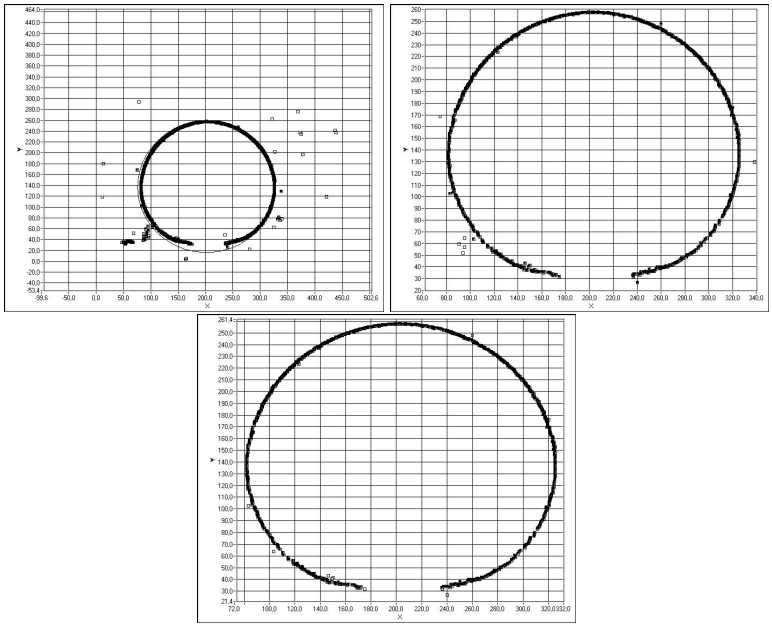

Figure A.1: Example of three consecutive cleaning steps. Left: a coarse grained selection. The Global elliptic fit is superposed; Center: Medium grained clean; Right: Fine clean. All subsets are merged again together.

the whole filtered profile, the program produces the best global fit. Alternatively, a subset into a band of given maximum height from the contact line (hand selected from the picture) can be chosen. It gives a local determination of the contact angle. Usually both these determination are simultaneously performed and plotted to give a visual check and comparison.

A.5 Curvature Calculation

One of the latest update of the software includes a standard calculation of the curvature of the droplet. In this case, all profile points are sorted by their polar coordinate with respect to the center of the best elliptical fit and grouped in small intervals of given angular amplitude, each of them fitted with a circular shape. Initial fitting parameters are the center and radius resulting from the global fit. Relevant parameters like the center and the radius of the droplet are recorded for further analysis. We note that the results of the fitting procedure described in section A.1 are strongly dependent from initial conditions when points are close together. This consideration makes this procedure not consistent in order to calculate the local radius of curvature, but allows a nice local determination of the vector orthogonal to the profile.

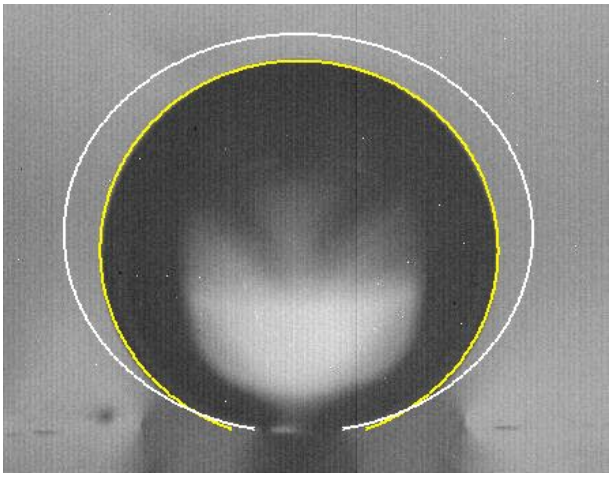

Figure A.2: Comparison between global and local elliptic fit shapes for a highly distorted droplet.

A.6 Error Calculation

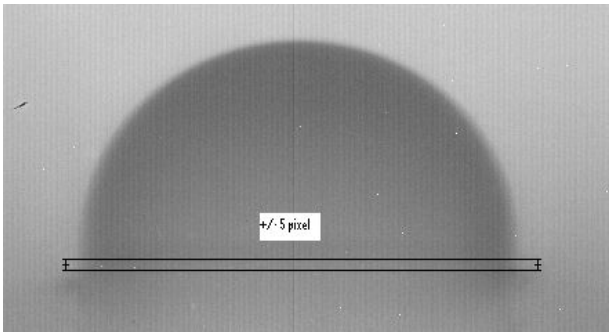

Figure A.3: Example of an error bar of ± 5 pixel in contact height determination .

The error related to the numerical procedure is essentially related to two contributions. The first is the adherence of the fitting curve to the droplet contact line. Usually a local fit is expected to give the best determination of the contact angle but the global fit is needed when the droplet profile is not too warped and experimental conditions do not allow a good determination of the profile near the contact line (i.e an elongated drop viewed from the orthogonal direction shows a profile often out of focus). Sometimes it is interesting a comparison between these two determinations. Once the region of interst is selected, the errors related to the way the algorithm finds the best fit are negligible, with respect to the differenced produced by changing the selection. The second aspect is the determination of the position of the contact line. This operation is performed by

hand when selecting the regions of interest. For values of contact angles $\theta \gg 90^\circ$ or $\theta \ll 90^\circ$, a choice of the x-axis of the intersection point is more accurate, while for $\theta \sim 90^\circ$ the more accurate choice lies on the y-axis. As an example, taking the spherical profile of a droplet of volume ($0.5\mu l = 1.17 \times 10^7 \text{pixel}^3$) we have calculated the position of the contact line with respect to the center of the droplet in pixel dimensions by the relation

$$h(\theta) = \left(\frac{3V}{\pi(1-\cos\theta)^2(2+\cos\theta)} \right)^{1/3} \cos\theta \tag{A.7}$$

Assuming to give a determination of the height differece from 1 to 3 pixels around the real value, we have calculated the corresponding angle difference as a function of the real contact angle θ. Results are reported in figure A.4. It is shown that also in the worst case of a 3 pixels of discrepancy this error lies under 1 degree until $\theta < 90^\circ$. For higher contact angles the error increases, but by no more than 2 degrees for $\theta < 140^\circ$. For higher angles the local height is determined by the intersection of the profile with the x-axis coordinate. This calculation suggests that the numerical error in the contact angle determination is negligible if compared with deviations related to surface imperfections and other kinds of noise.

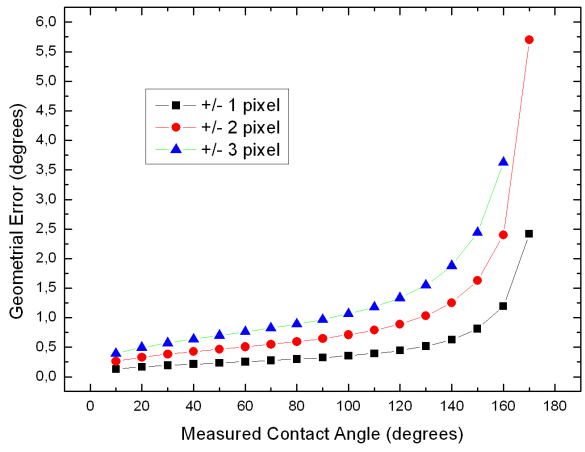

Figure A.4: Half difference of geometrical contact angle evaluation in case of errors of 1,2 and 3 pixels in contact height determination for a droplet of volume $0.5\mu l$.

A.7 Image Sequence Analysis

The calculation of advancing and receding contact angles is obtained with a repeated application of the previous operations on all the sequence of images. In principle each time all software parameters should be varied to match images. This tedious operation may be avoided assuming that most parameters remain the same. This is not completely true. The first problem is that the investigation window changes size. Giving a larger window for all the sequence is a solution, but sometimes defects on the substrate or around the profile may affect results. Fortunately, when these errors appear they are large, and may be easily filtered from the sequence results. Another problem is related with the droplet expansion, which moves out of focus the profile for large volumes. In this case, only the first part of the sequence is mantained. As shown in section 4.6, the profiles may deviate from the spherical cup shape principally because of the needle size. In this case two polinomial fits on the two sides of the droplet work better than a global elliptic one. In any case, all fitting procedures are implemented and may be chosen depending on experimental conditions.

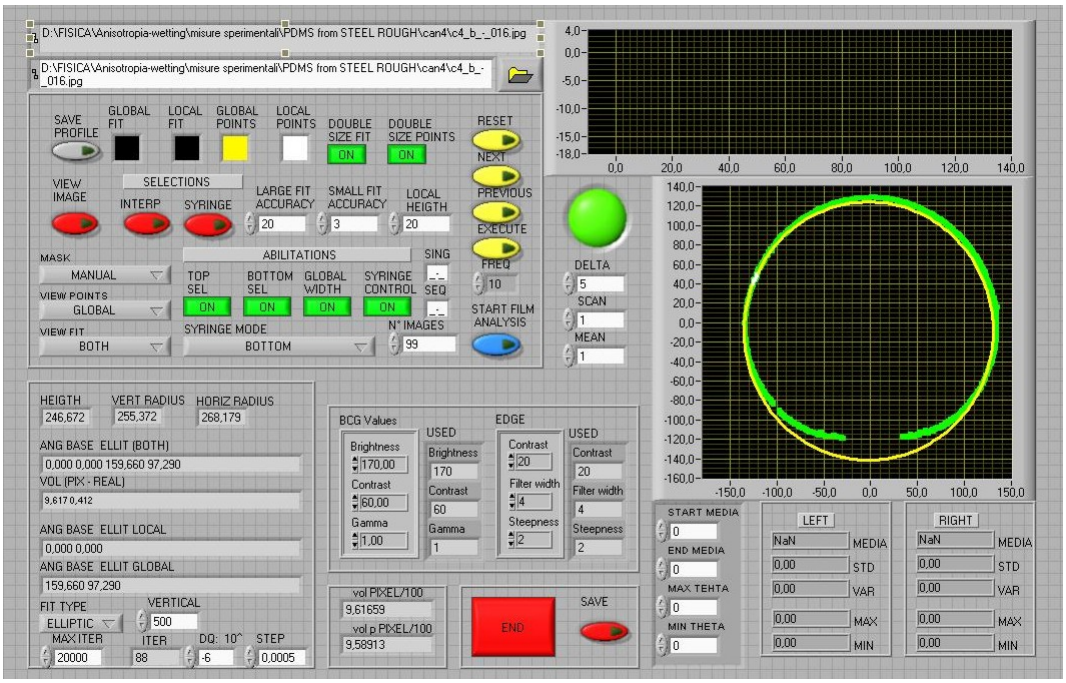

Figure A.5: Screenshot of the Image Analysis Tool Front Panel

Appendix B

Possible Bondary conditions in Lattice Boltzman

Here are listed the boundary conditions used to define missing distribution functions, i.e., those that stream from positions outside the simulation box, taken from [70].

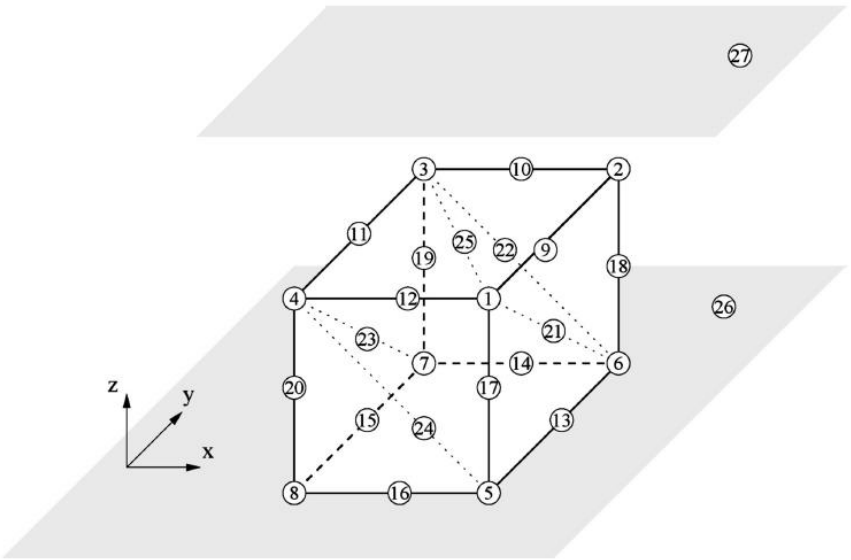

Figure B.1: The directions of the lattice velocity vectors in the 15-velocity lattice Boltzmann model.

Label (see fig. B.1)	Conditions
1	$f_{13} = f_{14}$
2	$f_7 = f_8$
3	$f_9 = f_{10}$
4	$f_{11} = f_{12}$
5	$f_5 = f_6$ $f_{13} = (f_3 - f_4 - f_1 + f_2)/2 + f_9 + f_{14} - f_{10}$ $f_{11} = (f_1 - f_2)/2 - f_9 + f_{10} + f_{12}$ $f_7 = (-f_3 - f_4)/2 + f_8 - f_9 + f_{10}$
6	$f_5 = f_6$ $f_{13} = (f_3 - f_4)/2 - f_{11} + f_{12} + f_{14}$ $f_9 = (f_1 - f_2)/2 - f_{11} + f_{10} + f_{12}$ $f_7 = (-f_1 + f_2 - f_3 + f_4)/2 + f_8 + f_{11} - f_{12}$
7	$f_5 = f_6$ $f_{11} = (f_3 - f_4)/2 - f_{13} + f_{12} + f_{14}$ $f_9 = (f_1 - f_2 - f_3 + f_4)/2 - f_{13} - f_{14} + f_{10}$ $f_7 = (-f_1 + f_2)/2 + f_8 - f_{13} + f_{14}$
8	$f_5 = f_6$ $f_{11} = (f_3 - f_4 + f_1 - f_2)/2 + f_7 - f_8 + f_{12}$ $f_9 = (-f_3 + f_4)/2 - f_7 + f_8 + f_{10}$ $f_{13} = (-f_1 + f_2)/2 - f_7 + f_8 + f_{14}$
9	$f_{13} = f_{14}$ $f_7 = f_8$
10	$f_9 = f_{10}$ $f_7 = f_8$
11	$f_9 = f_{10}$ $f_{11} = f_{12}$
12	$f_{13} = f_{14}$ $f_{11} = f_{12}$
13	$f_5 = f_6$ $f_1 = 2(-f_{10} + f_9 + f_{11} - f_{12}) + f_{12}$ $f_{13} = (f_3 - f_4)/2 - f_{11} + f_{12} + f_{14}$ $f_7 = (-f_3 + f_4)/2 + f_8 - f_9 + f_{10}$

Label (see fig. B.1)	Conditions
14	$f_5 = f_6$ $f_9 = (f_1 - f_2)/2 - f_{11} + f_{10} + f_{12}$ $f_7 = (-f_1 + f_2)/2 + f_8 - f_{13} + f_{14}$ $f_3 = 2(-f_{12} + f_{11} + f_{13} - f_{14}) + f_4$
15	$f_5 = f_6$ $f_2 = 2(-f_{14} + f_7 + f_{13} - f_8) + f_1$ $f_{11} = (f_3 - f_4)/2 - f_{13} + f_{12} + f_{14}$ $f_9 = (-f_3 + f_4)/2 + f_8 - f_7 + f_{10}$
16	$f_5 = f_6$ $f_{11} = (f_1 - f_2)/2 - f_9 + f_{10} + f_{12}$ $f_{13} = (-f_1 + f_2)/2 - f_7 + f_8 + f_{14}$ $f_4 = 2(-f_{10} + f_7 + f_9 - f_8) + f_3$
17	$f_{10} = f_9$ $f_{13} = f_{14}$
18	$f_7 = f_8$ $f_{12} = f_{11}$
19	$f_9 = f_{10}$ $f_{14} = f_{13}$
20	$f_8 = f_7$ $f_{11} = f_{12}$
21	$f_1 = f_2$ $f_7 = f_8$ $f_{12} = (-f_3 + f_4)/2 + f_{11}$ $f_{13} = (-f_5 + f_6)/2 + f_{14}$ $f_{10} = (f_3 - f_4 + f_5 - f_6)/2 + f_9$
22	$f_3 = f_4$ $f_7 = f_8$ $f_9 = (-f_5 + f_6)/2 + f_{10}$ $f_{13} = (f_1 - f_2 + f_5 - f_6)/2 + f_{13}$ $f_{10} = (-f_1 + f_2)/2 + f_{11}$

Label (see fig. B.1)	Conditions
23	$f_2 = f_1$ $f_8 = f_7$ $f_{11} = (f_3 - f_4)/2 + f_{12}$ $f_{14} = (f_5 - f_6)/2 + f_{13}$ $f_9 = (-f_3 + f_4 - f_5 + f_6)/2 + f_{10}$
24	$f_8 = f_7$ $f_4 = f_3$ $f_{11} = (f_1 - f_2)/2 + f_{12}$ $f_{10} = (f_5 - f_6)/2 + f_9$ $f_{13} = (-f_5 + f_6 - f_1 + f_2)/2 + f_{14}$
25	$f_7 = f_8$ $f_5 = f_6$ $f_{11} = (f_1 - f_2 + f_3 - f_4)/2 + f_{12}$ $f_9 = (-f_3 + f_4)/2 + f_{10}$ $f_{13} = (-f_5 + f_6 - f_1 + f_2)/2 + f_{14}$
26	$f_7 = f_8$ $f_5 = f_6$ $f_{11} = (f_1 - f_2 + f_3 - f_4)/2 + f_{12}$ $f_9 = (-f_3 + f_4)/2 + f_{10}$ $f_{13} = (-f_5 + f_6 - f_1 + f_2)/2 + f_{14}$
27	$f_6 = f_5$ $f_8 = f_7$ $f_{10} = (f_3 - f_4)/2 + f_9$ $f_{14} = (f_1 - f_2)/2 + f_{13}$ $f_{13} = (-f_3 + f_4 - f_1 + f_2)/2 + f_{11}$

Appendix C

Detailed calculations of the anisotropic model

C.1 Calculation of $\theta_\perp$ and Volume

Following [85] we consider droplet profiles as circular shapes. In this case, the apparent contact angles can be written as

$$\tan\theta_\parallel/2 = h/B_\parallel \qquad \tan\theta_\perp/2 = h/B_\perp \tag{C.1}$$

where $B_\parallel$ and $B_\perp$ are the drop base lengths in the two principal directions. As a result,

$$\tan\theta_\perp/2 = e\tan\theta_\parallel/2 \tag{C.2}$$

where

$$e = \left(\frac{B_\parallel}{B_\perp}\right) = \left(\frac{1+\epsilon}{1-\epsilon}\right) \tag{C.3}$$

Consider the shape of the three phase contact line of the droplet generalized as in equation 6.2.3

$$\left(\frac{|x|}{A}\right)^\alpha + \left(\frac{|y|}{B}\right)^\alpha = 1 \tag{C.4}$$

where the droplet is centered in the origin of the axis and $A = B_\perp/2$ ($B = B_\parallel/2$) is the perpendicular (parallel) semi axes. The local orthogonal elongation $x(y)$ is given by

$$x(y) = A\sqrt[\alpha]{1 - \frac{y^\alpha}{B^\alpha}} = \sqrt[\alpha]{A^\alpha - e^{-\alpha} y^\alpha} = \sqrt[\alpha]{A^\alpha - \left(\frac{1-\epsilon}{1+\epsilon}\right)^\alpha y^\alpha} \tag{C.5}$$

Assuming that the parallel profile is an arc of circumference with base length $B_\parallel$, radius R and contact angle θ_a we have

$$R = \frac{B}{\sin\theta_a} \tag{C.6}$$

while the height of the center Z_{CM} of the circumference is given by

$$Z_{CM} = R\cos\theta_\parallel = B\cot\theta_a \tag{C.7}$$

and the local heigth of the droplet along the y axis is given by

$$h(y) = \sqrt{R^2 - y^2} - Z_{CM} = \frac{\sqrt{B^2 - y^2\sin^2\theta_a} - B\cos\theta_a}{\sin\theta_a} \tag{C.8}$$

We assume that not only the main orthogonal profile has a circular shape, but also every other orthogonal section of the droplet, full defined when requested to pass between points

$$[P_1 = (0, h(y)); P_2 = (-x(y), 0); P_3 = (x(y), 0)]$$

Solving the system one get the height center coordinate and radius of the circular section located in (y), and the local contact angle

$$Z(y) = \frac{h^2(y) - x^2(y)}{2h(y)}; \qquad R(y) = \frac{h^2(y) + x^2(y)}{2h(y)} \tag{C.9}$$

$$\theta_\perp(y) = \arccos\left(\frac{x^2(y) - h^2(y)}{x^2(y) + h^2(y)}\right) \tag{C.10}$$

Substituting equations C.5 and C.8 intoequation C.10 for $y = 0$ we get $\theta_\perp$ on the main orthogonal axis (eq. 6.6), while in the general case we have

$$\begin{aligned}\theta_\perp(\epsilon,\theta_a) &= \arccos\left(\frac{B_\perp^2 - h^2(0)}{B_\perp^2 + h^2(0)}\right) \\ &= \arccos\left(\frac{\sin^2\theta_a - \left(\frac{1+\epsilon}{1-\epsilon}\right)^2(1-\cos\theta_a)^2}{\sin^2\theta_a + \left(\frac{1+\epsilon}{1-\epsilon}\right)^2(1-\cos\theta_a)^2}\right)\end{aligned} \tag{C.11}$$

Finally, to get the droplet volume one only need to integrate the area of the circular portion from $-B$ to B in case of $\theta_a < 90°$. In case of $\theta_a > 90°$ the integration is extended with disks of radius $(h(y) - Z(y))/2$ from $-R$ to $-B$ and from B to R.

$$A = \frac{R(y)}{2}\theta_\perp(y) + Z(y)x(y) \tag{C.12}$$

$$V = \int_{-B}^{B}\left[\frac{h^2(y)+x^2(y)}{h(y)}\arccos\left(\frac{h^2(y)-x^2(y)}{h^2(y)+x^2(y)}\right) - x(y)\left(\frac{h^2(y)-x^2(y)}{2h(y)}\right)\right]dy \tag{C.13}$$

We performed this calculation numerically.

C.2 Calculation of ratio $\frac{\Delta\theta}{\epsilon}\big|_{\epsilon\longrightarrow 0}$

For this model the relation is analytical, and can be simply obtained taking the first derivative of equation C.11. Takig it in the form

$$\Delta\theta = \arccos\left(\frac{A - \left(\frac{1+\epsilon}{1-\epsilon}\right)^2 B}{A + \left(\frac{1+\epsilon}{1-\epsilon}\right)^2 B}\right) - \theta_a \tag{C.14}$$

where

$$A = \sin^2\theta_a \qquad B = (1-\cos\theta_a)^2 \tag{C.15}$$

The derivative of the arccosin gives

$$\begin{aligned}\frac{\partial \arccos}{\partial\epsilon} &= -\frac{1}{\sqrt{1 - \left(\frac{A-\left(\frac{1+\epsilon}{1-\epsilon}\right)^2 B}{A+\left(\frac{1+\epsilon}{1-\epsilon}\right)^2 B}\right)^2}} \\ &= \frac{A + \left(\frac{1+\epsilon}{1-\epsilon}\right)^2 B}{2\sqrt{AB}\left(\frac{1+\epsilon}{1-\epsilon}\right)^2}\end{aligned}$$

while the derivative of its argument gives

$$-\frac{2AB}{\left(A+\left(\frac{1+\epsilon}{1-\epsilon}\right)^2 B\right)^2}\times\frac{\partial}{\partial\epsilon}\left(\frac{1+\epsilon}{1-\epsilon}\right)^2 \tag{C.16}$$

and

$$\frac{\partial}{\partial\epsilon}\left(\frac{1+\epsilon}{1-\epsilon}\right)^2 = 4\frac{(1+\epsilon)}{(1-\epsilon)^3} \tag{C.17}$$

Putting all together for $\epsilon \longrightarrow 0$ and substituting A and B with eq. C.15 we get the very simply equation

$$\begin{aligned}\frac{\partial\Delta\theta}{\partial\epsilon} &= 4\frac{\sqrt{AB}}{A+B}\\ &= 4\frac{\sqrt{\sin^2\theta_a(1-\cos\theta_a)^2}}{\sin^2\theta_a+(1-\cos\theta_a)^2}\\ &= 2\sin\theta_a\end{aligned} \tag{C.18}$$

C.3 Calculation of ratio $\left.\frac{\Delta\theta}{(V/w^3)}\right|_{\epsilon,\theta_a\longrightarrow 0}$

This ratio can be considered by the combination of derivatives

$$\left.\frac{\partial\Delta\theta}{\partial V/w^3}\right|_{\epsilon,\theta_a\longrightarrow 0} = \frac{\left.\frac{\partial\Delta\theta}{\partial\epsilon}\right|_{\epsilon,\theta_a\longrightarrow 0}}{\left.\frac{\partial\Delta(V/w^3)}{\partial\epsilon}\right|_{\epsilon,\theta_a\longrightarrow 0}} \tag{C.19}$$

where

$$\left.\frac{\partial\Delta\theta}{\partial\epsilon}\right|_{\epsilon,\theta_a\longrightarrow 0} = 2\sin\theta_a \tag{C.20}$$

To give a determination of $\left.\frac{\partial\Delta(V/w^3)}{\partial\epsilon}\right|_{\epsilon,\theta_a\longrightarrow 0}$, if the droplet shape were a part of an ellipsoid, we should have $\Delta V \sim V_s(1-e)$, where V_s is the spherical cup volume and e is given by eq. C.3. In our case the assumption that the parallel profile mantains always a circular shape produce a dependence of second order $\Delta V \sim V_s(1-e^2)$. In this way we have, using equation C.17

$$\begin{aligned}\left.\frac{\partial\Delta(V/w^3)}{\partial\epsilon}\right|_{\epsilon,\theta_a\longrightarrow 0} &= \frac{V_s}{W^3}\times\frac{\partial}{\partial\epsilon}\left(\frac{1+\epsilon}{1-\epsilon}\right)^2 = 4\frac{V_s}{W^3}\\ &= \frac{\pi}{6}\frac{(1-\cos\theta_a)^2(2+\cos\theta_a)}{\sin^3\theta_a}\end{aligned} \tag{C.21}$$

Finally we have

$$\begin{aligned}
\left.\frac{\partial\Delta\theta}{\partial(V/w^3)}\right|_{\epsilon,\theta_a \longrightarrow 0} &= \frac{12}{\pi}\frac{\sin^4\theta_a}{(1-\cos\theta_a)^2(2+\cos\theta_a)} \\
&\sim \frac{12\theta_a^4}{\pi\left(\frac{\theta_a^2}{2}\right)^2 3} \\
&\sim \frac{16}{\pi}
\end{aligned} \tag{C.22}$$

as shown in section 6.3.4.

Appendix D

Details of Surface Evolver calculations

Public domain software by Ken Brakke [131; 132] is used to numerically investigate the 3D drop shapes and the apparent contact angles on rough surfaces. Similar investigations of drop shapes on chemically heterogeneous surfaces has been reported earlier by Brandon et al. [133; 134] and by Patankar [99]. We neglect gravity, which is a reasonable assumption for small drops. The numerical procedure is based on minimizing the free energy of the system to obtain the equilibrium drop shape. The free energy G of the system is given by

$$\frac{G}{\sigma_{lf}} = S_{lf} - \int\int_{S_{sl}} \cos\theta_i(x,y)dxdy \tag{D.1}$$

where x and y are the dimensionless Cartesian spatial coordinates spanning the substratés surface, and S_{sl} and S_{lf} are the solid - liquid and liquid - fluid interfacial areas of contact along the solid - liquid and liquid - fluid interfaces, respectively. $\cos\theta_i(x,y)$ is the cosine of the surface local intrinsic contact angle which is defined using Young's equation:

$$\cos\theta_i(x,y) = \frac{\sigma_{sf}(x,y) - \sigma_{sl}(x,y)}{\sigma_{lf}} \tag{D.2}$$

where σ_{lf} is the liquid - fluid interfacial tension, assumed to be constant, $\sigma_{sf}(x,y)$ and $\sigma_{sl}(x,y)$ are the local solid - fluid and slolid - liquid interfacial tension respectively. Minimization of the free energy G (Eq. D.1) with respect to the liquid - fluid interface shape, while constraining the drop's volume to a fixed value, yields the equilibrium form of the drop. Also the contact line of the droplet can be constrained to a given shape.

In the solution procedure, G/σ_{lf} is minimized. Hence, for a given problem, the only material parameter we need to specify is θ_a. It can be shown [135] using variational principles that the constrained minimization procedure, above, is equivalent to solving the Laplace equation for the pressure drop at each point on the liquid - fluid interface,

$$\frac{2\sigma_{lf}}{R_m} = \Delta p \tag{D.3}$$

along with Youngś equation D.2 on the solid - liquid - fluid contact line as the boundary condition. R_m is the mean radius of curvature and Δp is the pressure drop, at a point on the drop surface. A stationary drop on a substrate, in constant ambient pressure, will have a constant pressure drop at each point on the liquid - fluid interface (gravity neglected). Hence, it follows directly from Eq. D.3 that a sessile drop should have a constant mean curvature surface. In two dimensions, the arc of a circle is the only constant mean curvature curve. In three dimensions, the spherical surface is one of the many possible constant mean curvature surfaces. Detailed information about the numerical methodology to solve the constrained minimization problem (Eq. (1)) is available in the Surface Evolver manual [131]. A brief descriptionis given here.

The equilibrium drop shape is obtained iteratively from the initial shape. At each iteration the vertices on the liquid - fluid interface are moved in order to reduce the energy of the system while adhering to the imposed constraints (e.g., constant volume). Iterations are repeated until the system's energy does not change significantly.

A typical set of simulations contain the instructions in four different files: a file named "'simulation.cm"' contains the counters of the loops and the loading of the other files:

```
  run ::= {
    for ( count1 ::=0 ; count1 < 20 ; count1 ::= count1 + 1) {
           permload "simulation.fe";
           read "simulationgogo.cm";
           read "simulation.gogo";
           };
}
```

T file named "'simulation.fe"' contains the initialization of useful parameters, of the starting shape of the droplet, and the rules to apply the constraints:

```
// Patankar like simulations

PARAMETER nnn = 0        // number of simulation
PARAMETER angle1 = 90    // contact angle
PARAMETER pa1 = 8        // slope of pattern edges
PARAMETER lx = 2         // X axis initial lenght
PARAMETER ly = 2         // Y axis initial lenght
```

```
PARAMETER lz = 1         // Z axis initial lenght

PARAMETER cth = cos(angle1*pi/180)
PARAMETER sth = sin(angle1*pi/180)
PARAMETER Vp = (1-cth)**2*(2+cth)/sth**3/2   // nondim vol
PARAMETER Dmean = (12*lx*ly*lz/pi/Vp)**(1/3) // mean diameter

PARAMETER lhm = 2e-002  // Pattern channels depth
PARAMETER lpm = 2e-002  // Pattern channels width

PARAMETER RMAX = 1.2  // boundary radius
PARAMETER SHAPE = 2   // exponent of the boundary shape
PARAMETER ccc1 = 50   // raggio boundary
PARAMETER AB = 1.2    // boundary elongation
PARAMETER ccc2 = 0.2  // raggio boundary
PARAMETER C1 = 0   // Constant 3 switch 1
PARAMETER C2 = 1   // Constant 3 switch 2

parameter div = 5          //facets in insiade a groove
parameter toll = 1e-8      //energy output condition
parameter maxint = 200     //maximum number of iterations
parameter go1refine = 0.02 //upper limit to refine edges

define pointv real[10][100000]
define pointe real[4][100000]
define pointf real[5][100000]

gravity_constant 0  // start with gravity off


//-------------------------------------------------

constraint 1   /* first simmetry plane */

formula: x=0
```

```
energy:  // no energy

e1: 0
e2: 0
e3: 0

//-------------------------------------------------

constraint 2   /* second simmetry plane */

formula: y=0

energy:  //no energy

e1: 0
e2: 0
e3: 0

//-------------------------------------------------

constraint 3   /* geometrical groove pattern */

formula: z=0 // ( quasi rettangolari)

energy:  // no energy

e1: y*cos(angle1*pi/180)*(c1/(exp(pa1*sin(pi*(x/lp+0.5)))+1)+c2)
e2: 0
e3: 0

//-------------------------------------------------


constraint 4   /* contact line boundary */

formula: RMAX*RMAX=((sqrt(x*x))**(SHAPE)
```

```
                    + sqrt(y*y/AB/AB))**(SHAPE))

//-----------------------------------------------------

vertices
1    -lx/2  -ly/2 0.0  constraint 3,4
2     lx/2  -ly/2 0.0  constraint 3,4
3     lx/2   ly/2 0.0  constraint 3,4
4    -lx/2   ly/2 0.0  constraint 3,4
5    -lx/2  -ly/2 lz
6     lx/2  -ly/2 lz
7     lx/2   ly/2 lz
8    -lx/2   ly/2 lz


edges  /* given by endpoints and attribute */
1   1 2    constraint 3,4
2   2 3    constraint 3,4
3   3 4    constraint 3,4
4   4 1    constraint 3,4
5   5 6
6   6 7
7   7 8
8   8 5
9   1 5
10  2 6
11  3 7
12  4 8

faces  /* given by oriented edge loop */
1   1 10 -5  -9
2   2 11 -6 -10
3   3 12 -7 -11
4   4  9 -8 -12
5   5  6  7   8
```

```
bodies  /* one body, defined by its oriented faces */
1   1 2 3 4 5   volume lx*ly*lz  density 1
```

The file "‘simulationgogo.cm"’ contains the typical evolution instruction.

```
// Typical instructions

// operations on elements

r1 := refine edges where on_constraint 1;
r2 := refine edges where on_constraint 2;
r3 := refine edges where on_constraint 3;
re3 := foreach edge ee where
       max(ee.vertex vvv, vvv on_constraint 3)
       do refine ee;
rel3 := foreach edge ee where ee.length > lhm/5
        and max(ee.vertex vvv, vvv on_constraint 3)
        do refine ee;
rez  := foreach edge ee where max(ee.vertex vvv, vvv.z <0 )
       do refine ee;
relz := foreach edge ee where
        (ee.length > lhm/(div-1) and ee.vertex[1].z <lhm
        and ee.vertex[2].z <lhm) do refine ee;
delz := delete edge ee where
        (ee.length < lhm/div and ee.vertex[1].z <lhm
        and ee.vertex[2].z <lhm);
delx := delete edge ee where
        (ee.vertex[1].x <0 or ee.vertex[2].x <0);
dely := delete edge ee where
        (ee.vertex[1].y <0 or ee.vertex[2].y <0);
refz := foreach edge ee where
        (max(ee.facet ff, ff.area > lhm*lhm/25)
        and ee.length > lhm/10 and max(ee.vertex vv, vv.z <0))
        do refine ee;
ref3 := foreach edge ee where
```

```
        (max(ee.facet ff, ff.area > lhm*lhm/25) or
        ee.length > lhm/5) and
        max(ee.vertex vvv,
        max(vvv.edge eee, eee on_constraint 3))
        do refine ee;
sz   := show facets ff where avg(ff.vertex vv, vv.z <0 );


color1 := foreach facet ff where
          avg(ff.edge ee, sin(pi*((ee.vertex[1].x+
          ee.vertex[2].x)/2/lp+0.5)) >= 0)  do
{set ff color red;}

color2 := foreach facet ff where
          avg(ff.edge ee, sin(pi*((ee.vertex[1].x+
          ee.vertex[2].x)/2/lp-0.5)) >= 0)  do
{set ff color yellow;}


\\evolution instructions

 gof := {
 nn:=0;
     delete facets where area < lhm*lhm/div/div;
 u; u; u; u;
         olde := total_energy; g;
         newe := total_energy; g;
         diffe := olde - newe;
  while ((diffe*diffe - toll*toll > 0) and (nn<maxint)) do
                { g5;
                  delete facets where area == 0;
           olde := total_energy;
           g;
                  newe := total_energy;
                  diffe := olde - newe;
                  nn:=nn+1    };
```

```
        printf " DIFFE: %4g\ \n  ", diffe;
        printf " NN   : %4g\ \n  ", nn;

 }

go0 := { r3; r; g5 ;
         r; g5; u; u;
         re3; u; u;
         g250; r; r;
         maxint:=3000;
         toll:=1e-6;
        gof;
        re3;
        gof;
    };
```

The file "simulation.gogo" recall these istructions and print a list of vertices on interest along the main axxis and the contact line:

```
RMAX :=Dmean*(1-count1/100)/2;
AB := (1+count1/100)/(1-count1/100);
SHAPE := 2;
nnn:= count1;

verfile4 := SPRINTF "p%04gs_xy.ver",nnn;
verfile5 := SPRINTF "p%04gs_z.ver",nnn;
verfile7 := SPRINTF "p%04gs_const.ver",nnn;
datfile := SPRINTF "p%04g.dat",nnn;
dmpfile1 := SPRINTF "p%04g equi.dmp",nnn;
dmpfile2 := SPRINTF "p%04g.dmp",nnn;

ps_colorflag on;
gridflag on;
```

```
go0;

printf " Number of simulation   : \n %4g \n ", nnn >>> datfile;
printf " Local wettability   : \n %f \n ", angle1 >> datfile;
printf " Local wettability (cos)  : \n %f \n ",
        cos(angle1*pi/180) >> datfile;
printf " Sharpness   : \n %4g \n ", pa1 >> datfile;
printf " X dimension   : \n %4g \n ", lx/2 >> datfile;
printf " Y dimension   : \n %4g \n ", ly/2 >> datfile;
printf " Z dimension   : \n %4g \n ", lz >> datfile;
printf " Grooves height   : \n %f \n ", lhm >> datfile;
printf " Grooves width   : \n %f \n ", lpm >> datfile;
printf " Dmean   : \n %f \n ", Dmean >> datfile;
printf " Initial radius   : \n %f \n ", RMAX >> datfile;
printf " Initial asimmetry   : \n  %f \n ", AB >> datfile;
printf " Vprimo   : \n  %f \n ", Vp >> datfile;
printf " Tolerance    : \n %4g \n ", toll >> datfile;
printf " Max iterations    : \n %4g \n ", maxint >> datfile;
printf " Large refinement  : \n %f \n ", go1refine >> datfile;
printf " Total Energy   : \n %f \n ", total_energy >> datfile;
printf " Shape   : \n %f \n \n", shape >> datfile;

v >> datfile;
c >> datfile;
e >> datfile;

list vertices vv where (abs (vv.x) < 0.01) >>> verfile4;
list vertices vv where (abs (vv.y) < 0.01) >> verfile4;
list vertices vv where (abs (vv.z) < 0.005) >>> verfile5;
```

Outputs are finally analyzed with a set of Labview apposite tools.

List of Figures

Bibliography

[1] Young, T. "An Essay on the Cohesion of Fluids", *Philos. Trans. R. Soc. London.* **1805**, 95, 65.

[2] Araujo, Y. C.; Toledo, P. G.; Leon, V.; Gonzalez, H. Y. "Wettability of silane-treated glass slides as determined from X-ray photoelectron spetroscopy", *J. Colloid Interface Sci.* **1995**, 176, 485.

[3] Colorado, R.; Lee, T. R. "Wettabilities of self-assembled monolayers on gold generated from progressively fluorinated alkanethiols", *Langmuir* **2003**, 19, 3288.

[4] Davies, J.; Nunnerley, C. S.; Brisley, A. C.; Sunderland, R. F.; Edwards, J. C.; Kruger, P.; Knes, R.; Paul, A. J.; Hibbert, S. " Argon plasma treatment of polystyrene microtiter wells. Chemical and physical characterisation by contact angle, ToF-SIMS, XPS and STM", *Colloids Surf. A* **2000**, 174, 287.

[5] Athanassiou, A.; Lygeraki, M. I.; Pisignano, D.; Lakiotaki, K.; Varda, M.; Mele, E.; Fotakis, C.; Cingolani, R.; Anastasiadis, S. H. "Photocontrolled variations in the wetting capability of photochromic polymers enhanced by surface nanostructuring", *Langmuir* **2006**, 22, 2329.

[6] Han, J. T.; Zheng, Y.; Cho, J. H.; Xu, X.; Cho, K. "Stable superhydrophobic organic-inorganic hybrid films by electrostatic self-assembly", *J. Phys. Chem. B* **2005**, 109, 20773.

[7] Autumn, K.; Liang, Y. A.; Tonia Hsieh, S.; Zesch, W.; Chan, W. P.; Kenny, T. W.; Fearing, R.; Full, R. J. "Adhesive force of a single gecko foot-hair", *Nature* **2000**, 405, 681.

[8] Parker, A. R.; Lawrence, C. R. "Water capture by a desert beetle", *Nature* **2001**, 414, 33.

[9] Gau, H.; Herminghaus, S.; Lenz, P.; Lipowsky, R. "Liquid morphologies on structured surfaces: From microchannels to microchips", *Science* **1999**, 283, 46.

[10] Morita, M.; Koga, T.; Otsuka, H.; Takahara, A. "Macroscopic-wetting anisotropy on the line-patterned surface of fluoroalkylsilane monolayers", *Langmuir* **2005**, 21, 911.

[11] Brandon, S.; Haimovich, N.; Yeger, E.; Marmur, A. "Partial wetting of chemically patterned surfaces: The effect of drop size", *Colloid Interface Sci.* **2003**, 263, 237.

[12] Gleiche, M.; Chi, L.; Gedig, E.; Fuchs, H. "Anisotropic contact-angle hysteresis of chemically nanostructured surfaces", *Chem. Phys. Chem.* **2000**, 85, 1930.

[13] Higgins, A. M.; Jones, R. A. L. "Anisotropic spinodal dewetting as a route to self-assembly of patterned surfaces", *Nature* **2000**, 404, 476.

[14] Ionov, L.; Houbenov, N.; Sidorenko, A.; Stamm, M.; Minko, S. "Smart microfluidic channels", *Adv. Funct. Mater.* **2006**, 16, 1153.

[15] Sommers, A. D.; Jacobi, A. M. J. "Creating micro-scale surface topology to achieve anisotropic wettability on an aluminum surface", *J. Micromech. Microeng.* **2006**, 16, 1571.

[16] Feng, L.; Shuhong, L.; Yingshun, L.; Huanjun, L.; Zhang, L.; Zhai, Y.; Song, Y.; Liu, B.; Jiang, L.; Zhu, D. "Super-hydrophobic surfaces: From natural to artificial", *Adv. Mater.* **2002**, 14, 1857.

[17] De Gennes, S. J.; Quèrè, D. "Capillarity and wetting phenomena : drops, bubbles, pearls, waves." *Academic Press; New York*,(1982)

[18] Quèrè D. "Rough Ideas on Wetting", *Physica A* **2005**, 313, 32.

[19] Laplace P. "Oeuvres compl'etes de Laplace", *Paris : Gauthier-Villars.*, **1878**.

[20] Ming W.; Wu D.; Van Benthem R.; and de With G. "Superhydrophobic Films from Raspberry-Like Particles", *Nano Lett.* **2005**, 5, 2298.

[21] Zhu L.; Xiu Y.; Xu J.; Tamirisa P.; Hess D.; and Wong C. "Superhydrophobicity on Two-Tier Rough Surfaces Fabricated by Controlled Growth of Aligned Carbon Nanotube Arrays Coated with Fluorocarbon", *Langmuir* **2005**, 21, 11208.

[22] Gao X.; Yao X.; and Jiang L. "Effects of Rugged Nanoprotrusions on the Surface Hydrophobicity and Water Adhesion of Anisotropic Micropatterns", *Langmuir* **2005**, 23, 4886.

[23] Barthlott W. and Neinhuis C. "Purity of the Sacred Lotus, or Escape from Contamination in Biological Surfaces", *Planta* **1997**, 202, 1.

[24] Neinhuis C. and Barthlott W. "Characterization and distribution of water-repellent, self-cleaning plant surfaces", *Ann. Bot* **1997**, 79, 1667.

[25] Bico J.; Marzolin C. and Quèrè D. "'Pearl Drops"', *Europhys. Lett.* **1999**, 47, 220.

[26] Pozzato A.; Dal Zilio S.; Fois G.; Vendramin D.; Mistura G.; Belotti M.; Chen Y. and Natali M. "Superhydrophobic surfaces fabricated by nanoimprint lithography", *Micr. Eng.* **2006**, 83, 884.

[27] Tuteja A.; Choi W.; Ma M.; Mabry J.; Mazzella S.; Rutledge G.; McKinley G. and Cohen R. "Designing Superoleophobic Surfaces", *Science* **2007**, 318, 1618.

[28] Cao L.; Price T.; Weiss M.; and Gao D.; "Super Water- and Oil-Repellent Surfaces on Intrinsically Hydrophilic and Oleophilic Porous Silicon Films", *Langmuir* **2008**, 24, 1640.

[29] Cassie A. and Baxter S. "Wettability of Porous Surfaces", *Trans. Faraday Soc.* **1944**, 40, 546.

[30] Wenzel R. "Resistance of Solid Surfaces to Wetting by Water", *Ind. Eng. Chem.* **1936**, 28, 988.

[31] Ostrovskaya L.; Podestà A.; Milani P.; Ralcenko V. and Kholmanov I. "Wettability Studies of Nanostructured Cluster-Assembled Thin Films", *Europhys. Lett.* **2003**, 63, 401.

[32] Ishino C.; Okumura K and Quèrè D. "Wetting transitions on rough surfaces" *Europhys. Lett.* **2004**, 68, 419.

[33] Patankar N. A. "Transition between superhydrophobic states on rough surfaces", *Langmuir* **2004**, 20, 7097.

[34] Kusumaatmaja H.; Blow M. L.; Dupuis A. and Yeomans J. M. "The collapse transition on superhydrophobic surface", *Europhys. Lett.* **2008**, 81, 36003.

[35] Boruvka L. and Neumann A. W. "Generalization of the classical theory of capillarity", *J. Chem. Phys.* **1977**, 66, 5464.

[36] Drelich J.; Wilbur J. L.; Miller J.D. and Whitesides G.M. "Contact angles for liquid drops at a model heterogeneous surface consisting of alternating and parallel hydrophobic hydrophilic strips", *Langmuir* **1996**, 12, 1913.

[37] Wolansky G. and Marmur A. "The Actual Contact Angle on a Heterogeneous Rough Surface in Three Dimensions", *Langmuir*, **1998**, 14, 5292.

[38] Shibuichi, S.; Onda, T.; Satoh, N. and Tsuji, K. "Super water-repellent surfaces resulting from fractal structure", *J. Phys. Chem.* **1996**, 100, 19512.

[39] Sun, M.; Luo, C.; Xu, L.; Ji, H.; Ouyang, Q.; Yu, D. and Chen, Y. "Artificial lotus leaf by nanocasting", *Langmuir* **2005**, 21, 8978.

[40] Roach, P.; Shirtcliffe, N. J.; Newton, M. I. "Porous materials show superhydrophobic to superhydrophilic switching", *Chem. Comm* **2008**, 4, 224.

[41] He B.; Patankar N.A. and Lee J. "Multiple equilibrium droplet shapes and design criterion for rough hydrophobic surfaces", *Langmuir* **2003**, 19, 1249.

[42] Patankar N.A. "Mimicking the lotus effect: Influence of double roughness structures and slender pillars", *Langmuir* **2004**, 20, 8209.

[43] Marmur, A. "Underwater superhydrophobicity: Theoretical feasibility", *Langmuir* **2006**, 22, 1400.

[44] Yang, C.; Tartaglino, U.; Persson, B. N. J. "Influence of surface roughness on superhydrophobicity", . *Phys. Rev. Lett.* **2006**, 97, 116103.

[45] Blossey, R. "Self-cleaning surfaces - virtual realities", *Nature Mater.* **2003**, 2, 301.

[46] Burton, Z. and Bhushan, B. "Surface characterization and adhesion and friction properties of hydrophobic leaf surfaces", *Ultramicroscopy* **2006**, 106, 709.

[47] Joseph, P.; Cottin-Bizonne, C.; Benoit, J. M.; Ybert, C.; Journet, C.; Tabeling, P.; Bocquet, L. "Slippage of water past superhydrophobic carbon nanotube forests in microchannels", . *Phys. Rev. Lett.* **2006**, 97, 156104.

[48] Seemann, R.; Brinkmann, M.; Kramer, E. J.; Lange, F. F. and Lipowsky, R. "Wetting morphologies at microstructured surfaces", *Proc. Nat. Acad. Sci.* **2005**, 102, 1848.

[49] K. Efimenko, W.E. Wallace, and J. Genzer., *Journal of Colloid and Interface Science,*, **2002**, 254, 306.

[50] BOE R° BUFFERED OXIDE ETCHANTS from *Journal of Colloid and Interface Science,*

[51] Ulman, A., An introduction to ULTRATHIN ORGANIC FILMS From Langmuir-Blodgett to Self-Assembly *J. ACADEMIC PRESS: San Diego*, **1991**

[52] M. J. Madou, Foundamentals of microfabbrication: the scince of miniaturization, *CRC Press*,(2002)

[53] Ben G. Streetman, Solid State Electronic Devices *Prentice-Hall International, INC Edition*,(1999)

[54] Hoyle, C.E.; Lee. T.Y.; Roper, T.J., *Polym. Sci. Part A: Polym Chem.*, **2004**, 42, 5301.

[55] Cabral, J.T.; Cabral, J.T.; Douglas, J.F., *Langmuir*, **2004**, 20, 10020-10029.

[56] Warren, J.A.; Cabral, J.T.; Douglas, J.F., *Phys Rev E*, **2005**, 72, 021801.

[57] Harrison, C.; Cabral, J.T.; Stafford, C.M.; Karim, A.; Amis, E.J., *J. Micromech. Microeng.*, **2004**, 14, 153-158.

[58] Cygan, Z.T.; Cabral, J.T.; Beers, K.L.; Amis, E.J., *Langmuir*, **2005**, 21, 629-3634.

[59] Cleup, *http://www.cleup.it/index.php?centro=5*

[60] Xia, Y.; Whitesides, G.M., *Annu. Rev. Mater. Sci.*, **1998**, 281, 153.

[61] C.D. Bain, E.B. Troughton, Y.-T. Tao, J. Evall, G.M. Whitesides, R.G. Nuzzo, *J. Am. Chem. Soc.*, **1989**, 111, 321.

[62] E.A. Vogler, Interfacial chemistry in biomaterials science, in: *J. Berg (Ed.), Wettability, Marcel Dekker, New York,*, **1993**, pp. 184 - 250.

[63] L.M. Lander, L.M. Siewierski, W.J. Brittain, E.A. Vogler, A systematic comparison of contact angle methods. *Langmuir*, **1993**, 9, 2237.

[64] Jacqmin, D. "Contact-Line Dynamics of a Diffuse Fluid Interface", *J. Fluid Mech.* **2000**, 57, 402.

[65] Seppecher, P. "Moving Contact Lines in the Cahn-Hilliard Theory", *Int. J. Eng. Sci.* **1996**, 34, 977.

[66] Briant, A.; Wagner, A. and Yeomans J.M. "Lattice Boltzmann Simulations of Contact Line Motion. I. Liquid-Gas Systems", *Phys. Rev.* **2004**, 69, 031602.

[67] A. Briant and J. Yeomans, "Lattice Boltzmann Simulations of Contact Line Motion. II. Binary Fluids", *Phys. Rev.* **2004**, 69, 031603.

[68] Anderson, D.M.; McFadden, G.B. and Wheeler, A.A. "Diffuse-interface methods in fluid mechanics", *Annu. Rev. Fluid Mech.* **1998**, 30, 139.

[69] Briant, A.; Papatzacos, P. and Yeomans, J.M. "Lattice Boltzmann simulations of contact line motion in a liquid-gas system" , *Philos. Trans. R. Soc. London. Ser. A* **2002**, 360, 485.

[70] Dupuis, A. and Yeomans, J.M "Modeling Droplets on Superhydrophobic Surfaces: Equilibrium States and Transitions", *Langmuir* **2005**, 21, 2624.

[71] Cox, R. "The Dynamics of the Spreading of Liquids on a Solid Surface. Part 1. Viscous Flow", *J. Fluid Mech.* **1986**, 168, 169.

[72] Huh, C. and Scriven, L. "Hydrodynamic Model of Steady Movement of a Solid / Liquid / Fluid Contact Line", *J. Colloid Interf. Sci.* **1971**, 35, 85.

[73] Qian, T.; Wang, X. and Sheng, P. "A Variational Approach to Moving Contact Line Hydrodynamics", *J. Fluid Mech.* **2006**, 564, 333.

[74] Yeomans, J.M. "Mesoscale simulations: Lattice Boltzmann and Particle Algorithms", *Physica A* **2006**, 369, 159.

[75] Denniston, C.; Marenduzzo, D.; Orlandini, E. and Yeomans, J.M. "Lattice Boltzmann Algorithm for Three-Dimensional Liquid-Crystal Hydrodynamics", *Philos. Trans. R. Soc. A* **2004**, 362, 1745.

[76] Furtado, K. and Yeomans, J.M. "Lattice Boltzmann Simulations of Phase Separation in Chemically Reactive Binary Fluids", *Phys. Rev. E* **2006**, 73, 066124.

[77] Good, K.; Kuksenok, O.; Buxton, G.; Ginzburg, V. and Balazs, A. "Effect of Hydrodynamic Interactions on the Evolution of Chemically Reactive Ternary Mixtures", *J. Chem. Phys.* **2004**, 121, 6052.

[78] Ladd A. and Verberg, R. "Lattice-Boltzmann Simulations of Particle-Fluid Suspensions", *J. Stat. Phys.* **2001**, 104, 1191.

[79] Succi, S. "The Lattice Boltzmann Equation for Fluid Dynamics and Beyond", *Oxford: Oxford University Press.* **2001**.

[80] Swift, M.; Orlandini, E.; Osborn, W. and Yeomans, J.M. "Lattice Boltzmann Simultions of Liquid-Gas and Binary Fluid Systems", *Phys. Rev. E*, **1996**, 54, 5041.

[81] Swift, M.; Osborn, W. and Yeomans, J.M. "Lattice Boltzmann Simultion of Nonideal Fluids", *JPhys. Rev. Lett.* **1995**, 75, 830.

[82] Shan, X. and Chen, H. "Lattice Boltzmann Model For Simulating Flows with Multiple Phases and Components", *Phys. Rev. E* **1993**, 47, 1815.

[83] Kendon, V.; Cates, M.; Pagonabarraga, I.; Desplat, J. and Bladon, P. "Inertial Effects in Three-Dimensional Spinodal Decomposition of a Symmetric Binary Fluid Mixture: a Lattice Boltzmann Study", *J. Fluid Mech.* **2001**, 440, 147.

[84] Kusumaatmaja, H. and Yeomans, J. M. "Controlling drop size and polydispersity using chemically patterned surfaces", *Langmuir* **2007**, 23, 956.

[85] Kusumaatmaja, H.; Vrancken, R. J.; Bastiaansen, C. W. M.; and Yeomans, J. M. "Anisotropic drop morphologies on corrugated surfaces", *Langmuir* **2008**, 24, 7299.

[86] Cahn, J. W. "Critical-Point Wetting", *J. Chem. Phys.* **1977**, 66, 3667.

[87] C. Pooley and K. Furtado, "'Eliminating Spurious Velocities in the Free-Energy Lattice Boltzmann Method"', *Phys. Rev. E* , **2008**, 77, 046702.

[88] R. Benzi, L. Biferale, M. Sbragaglia, S. Succi, and F. Toschi, "'Mesoscopic Modeling of a Two-Phase Flow in the Presence of Boundaries: The Contact Angle"', *Phys. Rev. E* , **2006**, 74, 021509.

[89] J. Zhang and D. Kwok, "'Contact Line and Contact Angle Dynamics in Superhydrophobic Channels"', *Langmuir* , **2006**, 22, 4998.

[90] J. Hyvaluoma, A. Koponen, P. Raiskinmaki, and J. Timonen, "'Droplets on Inclined Rough Surfaces"', *Eur. Phys. J. E* , **2007**, 23, 289.

[91] A. Wagner and C. Pooley, "'Interface Width and Bulk Stability: Requirements for the Simulation of Deeply Quenched Liquid-Gas Systems"', *Phys. Rev. E* , **2007**, 76, 045702.

[92] Z. Guo, C. Zheng, and B. Shi, "'Discrete Lattice Effects on the Forcing Term in the Lattice Boltzmann Method"', *Physica A* , **2006**, 362, 105.

[93] Dupuis, A.; Yeomans, J. M, "'Lattice Boltzmann modelling of droplets onchemically heterogeneous surfaces"' *Fut. Gen. Comp. Syst.* , **2004**, 20, 993.

[94] Dupuis, A.; Yeomans, J. M, "'Modeling Droplets on Superhydrophobic Surfaces: Equilibrium States and Transitions"' *Langmuir* , **2005**, 21, 2624.

[95] D. d' Humieres, I. Ginzburg, M. Krafczyk, P. Lallemand, and L. Luo, "'Multiple-Relaxation-Time Lattice Boltzmann Models in Three Dimensions"' *Philos. Trans. R. Soc. A* , **2002**, 360, 437.

[96] Pompe, T. and Herminghaus, S. "Three-phase contact line energetics from nanoscale liquid surface topographies", *Phys. Rev. Lett.* **2000**, 85, 1930.

[97] Buehrle, J.; Herminghaus, S.; Mugele, F. "Impact of line tension on the equilibrium shape of liquid droplets on patterned substrates", *Langmuir* **2002**, 18, 9771.

[98] Bauer, C.; Dietrich, S. and Parry, A. O. "Morphological phase transitions of thin fluid films on chemically structured substrates", *Europhys. Lett.* **1999**, 47, 474.

[99] Chen, Y.; He, B.; Lee, Y. and Patankar, N. A. "Anisotropy in the wetting of rough surfaces", *J. Colloid Interface Sci.* **2005**, 281, 458.

[100] Chung, J. Y.; Youngblood, J. P. and Stafford, C. M. "Anisotropic wetting on tunable micro-wrinkled surfaces", *Soft Matter* **2007**, 3, 1163.

[101] Natali, M.; Begolo, S.; Carofiglio, T. and Mistura, G. "Rapid prototyping of multilayer thiolene microfluidic chips by photopolymerization and transfer lamination", *Lab Chip* **2008**, 8, 492.

[102] Briant, A. J.; Wagner, A. J. and Yeomans, J. M. "Lattice Boltzmann Simulations of Contact Line Motion. I. Liquid-Gas Systems", *Phys. Rev. E* **2004**, 69, 031602.

[103] Zhang F. and Low H. Y. "Anisotropic Wettability on Imprinted Hierarchical Structures", *Langmuir* **2007**, 23, 7793.

[104] Semprebon C.; Mistura G.; Orlandini E.; Bissacco G.; Segato A. and Yeomans J. "Anisotropy of water droplets on single rectangular posts", *Langmuir* **2009**, to be published.

[105] Bongiorno, G.; Lenardi, C.; Ducati, C.; Agostino, R. G.; et al. "Nano-crystalline Metal/Carbon Composites Produced by Supersonic Cluster Beam Deposition ", *J. of Nanosc. and Nanotech.* **2005**, 5, 1072.

[106] Giorgetti, Bongiorno, G.; Podestà, A.; et al. "Adsorption and stability of streptavidin on cluster-assembled nanostructured TiOx films ", *Langmuir* **2008**, 24, 11637.

[107] Barborini, E.; Kholmanov, I.N.; Conti, A.M. et al. "Supersonic cluster beam deposition of nanostructured titania", *Eur. Phys. J. D* **2003**, 24, 277.

[108] Brunette, D.; Tengvall P. et al. "Titanium in medicine: material science, surface science, engineering, biological responses and medical applications", *Berlin: Springer* **2001**

[109] Carbone, R.; Marangi, I.; Zanardi, A.; Giorgetti, L.; Podestà, A.; Bongiorno, G.; Milani, P. at al. "Biocompatibility of cluster-assembled nanostructured TiO_2 with primary and cancer cells", *Biomaterials* **2006**, 27, 3221.

[110] Lutolf, M.P. and Hubbell J.A.; "Synthetic biomaterials as instructive extracellular microenvironments for morphogenesis in tissue engineering", *Nat. Biotech.* **2005**, 23, 47.

[111] Kleinman, H.K.; Philp, D. and Hoffman, M.P. "Role of the extracellular matrix in morphogenesis", *Curr. Opin. Biotechnol.* **2003**, 14, 526.

[112] Chen, C. and Jiang, X. "Microengineering the environment of mammalian cells in culture", *MRS Bull.* **2005**, 30, 194.

[113] Dalby, M.J.; Riehle, M.O.; Sutherland, D.S. et al. "Use of nanotopography to study mechanotransduction in fibroblasts-methods and perspectives", *Eur. J. Cell. Biol.* **2004**, 83, 159.

[114] Dalby, M.J.; McCloy, D. et al. "Osteoprogenitor response to defined topographies with nanoscale depths", *Eur. J. Cell. Biol.* **2006**, 27, 1306.

[115] Shin, H.; Jo, S. and Mikos, A. "Biomimetic materials for tissue engineering", *Biomaterials* **2003**, 24, 4353.

[116] Hubbell, J. "Materials as morphogenetic guides in tissue engineering", *Curr. Opin. Biotechnol* **2003**, 14, 551.

[117] Long, M. and Rack, H.J. "Titanium alloys in total joint replacement-a materials science perspective", *Biomaterials* **1998**, 19, 1621.

[118] Barborini, E.; Piseri, P. and Milani P. "A pulsed microplasma source of high intensity supersonic carbon cluster beams", *J. Phys. D: Appl. Phys.* **1999**, 32, L105.

[119] Piseri, P.; Vahedi-Tafreshi, H. and Milani, P. "Manipulation of nanoparticles in supersonic beams for the production of nanostructured materials", *Curr. Opin. Solid State Mater. Sci.* **2004**, 8, 195.

[120] Mazza, T.; Barborini, E.; Kholmanov, I.N.; Piseri, P.; Bongiorno, G.; Vinati, S. et al. " Libraries of cluster-assembled titania films for chemical sensing", *Appl. Phys. Lett.* **2005**, 87, 103.

[121] Kholmanov, I.N.; Barborini, E.; Vinati, S.; Piseri, P.; Podestà, A.; Ducati, C. et al. "The influence of the precursor clusters on the structural and morphological evolution of nanostructured TiO_2 under thermal annealing", *Nanotechnology* **2003**, 14, 1168.

[122] Barborini, E. Kholmanov, I.N.; Piseri, P.; Ducati, D.; Bottani, C.E. and Milani, P. "Engineering of nanocrystalline structure of TiO_2 by aerodynamically filtered cluster deposition", *App Phys Lett* **2002**, 81, 3052.

[123] Liu, P.; Ziemann, P.J.; Kittelson, D.B. and McMurry, P.H. "Generating particle beams of controlled dimensions and divergence .1. Theory of particle motion in aerodinamic lenses and nozzle expansions", *Aerosol. Sci. Technol.*, **1995**, 22, 293.

[124] Liu, P.; Ziemann, P.J.; Kittelson, D.B. and McMurry, P.H. "Generating particle beams of controlled dimensions and divergence .2. Experimental evaluation of particle motion in aerodynamic lenses and nozzle expansions", *Aerosol. Sci. Technol.* **1995**, 314, 293.

[125] Bao-Xiang, W. and Zhao, X. "The wettability, size effect and electrorheological activity of modified titanium oxide nanoparticle", *Coll. and Surf. A: Physicochem. Eng. Asp.* **2007**, 295, 27.

[126] Lawrence, J.; Hao, L.; and Chew, H.R "On the correlation between Nd:YAG laser-induced wettability characteristics modification and osteoblast cell bioactivity on a titanium alloy" , *Surf. & Coat. Tech.* **2006**, 200, 5581.

[127] Aronov, D. and Rosenman, G. "Surface energy modification by electron beam", *Surf. Sci.* **2007**, 601, 5042.

[128] Barabasi & Stanley, "Fractal concepts in surface growt", *Cambridge Univ., New York* **1995**.

[129] Palasantzas "Effect of the form of the height-height correlation function from a self affine surface", *Phys. Rev. B* **1993**, 48, 2873.

[130] Yang C.; Tartaglino, U. and Persson, B. N. J. "Influence of Surface Roughness on Superhydrophobicity", *Phys. Rev. Lett.* **2006**, 97, 116103.

[131] Brakke, K.A., http://www.susqu.edu/facstaff/b/brakke/evolver.

[132] Brakke, K.A. "The Surface Evolver", *Exp. Math.* **1992**, 1, 141.

[133] Brandon, S.; Wachs, A. and Marmur, A. "Simulated contact angle hysteresis of a three-dimensional drop on a chemically heterogeneous surface: A numerical example", *J. Colloid Interface Sci.* **1997**, 191, 110.

[134] Brandon, S.; Haimovich, N.; Yeger, E. and Marmur A. "Partial wetting of chemically patterned surfaces: The effect of drop size", *J. Colloid Interface Sci.* **2003**, 263, 237.

[135] Finn, R. "Equilibrium Capillary Surfaces", *Springer - Verlag* **1986**, pp. 4 - 10.

Acknowledgements

Eccomi dunque ai saluti finali: innanzitutto vorrei ringraziare il mio mentore, il Prof. **Giampaolo Mistura** che mi ha sostenuto e spronato in questi anni, lasciandomi ampia libertà, e mettendo i giusti paletti quando necessario. E' stata una guida franca e rude, ma anche leale e generosa, il cui insegnamento più prezioso è stato un approccio rigoroso e pragmatico, ricordandomi che comunque ciò che serve è avere i piedi ben saldi a terra. Il secondo pensiero va al Prof. **Enzo Orlandini**, che mi ha aiutato tantissimo in quest'ultimo anno, e ha saputo levarmi le castagne dal fuoco quando più scottavano. E' una persona sempre gentile, sorridente, e ironica, che mi ha sempre mostrato il lato positivo delle cose. Un altro grande grazie va a **Gianluca Rossi**, che ha mostrato una pazienza infinita, fin dai tempi della tesi, data la mia abilità di far cadere il server, sempre pronto a illuminarmi sugli ultimi prodigi informatici, e a farmi partecipe dei sui raduni colplay di Star Wars. Una menzione per **Cinzia Sada**, che ho visto veramente arrabbiata una volta per una certa questione di vetri romani. Un ricordo speciale anche per **Giorgio Delfitto**, che ha condiviso l'amore per la musica classica, la passione per il caffè di mezza mattinata e i primi rudimenti del Labview. Un ricordo anche al Prof. **Lorenzo Bruschi** e a **Marco Natali**. Un ricordo importante anche per **Matteo Pierno**, promotore del restyling del laboratorio, e sempre disposto a chiacchierare di sport, e sapeva come solleticarmi. Un ringraziamento particolare per **Alessandro Pozzato**, per i campioni in silicio che non sono riuscito ad usare, e a **Giuliano Bissacco**: è il suo intervento che ha fatto prendere una svolta definitiva alla mia tesi. Infine per quanto concerne strettamente questo lavoro, una menzione doverosa per **Alessandro Podestà** e **Gero Bongiorno**, grazie al cui contributo il lavoro sulla titania ha visto infine la luce.

Vengo ora alla mia meravigliosa compagna di ufficio, **Laura Brigo**, che ha condiviso con me gioie e apprensioni di questi ultimi tre anni: polso di ferro in guanto di velluto, ma è stata anche gentile, cara e tenera. Ha sempre trovato una parola dolce e incoraggiante, e mi ha sempre fatto sentire il suo sostegno. In questi giorni si profila una bella e positiva novità per il tuo futuro. In bocca al lupo: faccio il tifo per te! Una menzione speciale anche per **Alì Shahid**, con cui ho potuto confrontarmi discutendo di cose serie e di cose leggere allo stesso tempo.

Viene ora il folto gruppo del **LAFSI**, con i tanti volti che si sono affacciati per lungo o breve periodo al nostro laboratorio: in primo luogo **Giovanni Fois**, a cui ne ho combinate alcune di

memorabili, ma che è sempre stato cordiale e comprensivo. Una menzione va sicuramente a **Barbara Perrone**, i cui campioni mai arrivati, alla fine son giunti a me. Vanno citati poi **Diego Vendramin**, colui che ha fatto il mio primo campione, e **Stefano Begolo** da cui ho attinto preziose fonti sulla microfabbricazione, e che ogni tanto cala giù dalla Francia per salutarci. Un saluto caro va a **Letizia d'Apolito**, con cui ho diviso un'intera stagione di spuntini a mezzogiorno, e **Stefano Noventa**, che non è del LAFSI, ma è opportuno inserire a questo punto. Un ricordo anche a **Marta Bonura**, che ogni volta che incontro mi piace farmi raccontare della Nuova Zelanda, e ancora **Matteo Ruzante, Matteo Stefan, Enrico Rossi, Sebastiano Valenti, Giuseppe Rinaldin** e **Davide Ferraro**, che è tornato da poco e mi sta dando una bella mano. E ancora **David Frizzo, Giorgio Carraro, Alberto Franzoi, Andrea Pacetti** e infine **Luca Porcelluzzi**, compagno oramai di vecchia data. Giacchè siamo veronesi "' tel digo 'n dialeto: mòete!"'

Una caloroso ricordo al mio più grande amico padovano: **Filippo Galeazzi**. Ormai sei a Berlino da un pezzo, ma è come se fossi sempre qua. Quante ne abbiamo passate insieme. Un grande saluto anche alla tua dolce metà: **Francesca Vidotto**. Del gruppo storico anche **Chiara Poletto**: ultimamente ci si vede poco, ma abbiamo cominciato insieme. Un caro saluto anche a tutti i **Nanerottoli**: le identità restino segrete, ma se un giorno qualcuno di quella compagnia sfoglierà casualmente queste pagine, sappia che ancora ricordo quella mitica settimana. Una menzione ai miei compagni di appartamento: **Federico Bertolazzo**, con cui ho discusso di tutto lo scibile umano, fuorchè di astronomia, **Annachiara, Alice** ed **Elda** per citare i più recenti. Infine un saluto ai **Colli Eugaei**, che hanno reso più ondulata la mia permanenza a Padova: senza di loro non sarebbe stata la stessa cosa.

Vengo ora a qualche doveroso saluto veronese: in primo luogo **Federico Albiero**, anche se adesso è a Barcellona, dopo aver girato mezza Europa: il più grande compagno di sempre. Poi **Riccardo Bertolazzi**: l'amico d'infanzia, che ora si laurea in **Indiana Jones-ologia**, e la rossa **Rossana**, che se l'è preso. Infine vorrei salutare tutta la società dell'**Ambrosiana**: siete in troppi per citarvi tutti, ma in particolare vorrei ricordare **Melchio** ed **Enzo** con cui ho condiviso gran parte degli allenamenti, il **Ceschi** con cui ho affrontato l'epica Campagnolo lunga del 2008, e il **Tobi** che è diventato un punto di riferimento. Un saluto anche a tutti quelli del forum, in particolare **Aqua** e **Brizzo** tra i padovani, e **Gio89** con cui ho fatto una fantastica vacanza sulle alpi francesi.

Infine un saluto alla mia bici: ne abbiamo fatta di strada insieme!